ABSTRACT

Title of Document: AN INVESTIGATION OF SOLID OXIDE FUEL CELL CHEMISTRY: A SPECTROSCOPIC APPROACH

Michael Brendan Scott Pomfret
Doctor of Philosophy, 2007

Directed By: Professor Robert A. Walker
Department of Chemistry and Biochemistry

Solid oxide fuel cells (SOFCs) represent an alternative power source that utilizes hydrogen and/or hydrocarbon fuels at significantly higher efficiencies than combustion systems; however, molecularly specific fuel oxidation mechanisms in SOFCs are not well understood. This research uses *ex-situ* techniques to quantify the physicochemical properties of SOFC materials and novel optical methods to identify chemical intermediates present *in-situ*.

Ex-situ experiments include quantifying gas-phase exhaust composition using Fourier transform infrared spectroscopy and characterizing material properties of SOFC components with Raman and X-ray photoelectron (XPS) spectroscopies. The exhaust studies show that fuel oxidation efficiencies depend on anode materials and fuels used. Nickel is a more active fuel oxidation catalyst than ceria; however, poor exhaust carbon balance indicates that nickel also promotes carbon deposition. Studies of YSZ indicate that the surface is chemically altered by reducing environments. This

observation can complicate our understanding of SOFC chemistry if the reduced surface participates in fuel oxidation chemistry.

In-situ Raman spectroscopy is combined with traditional electrochemical methods to characterize SOFC anodes at 715 °C. Raman spectra of the anode indicate the presence of NiO, graphite, and Ni-COO as fuel oxidation intermediates depending on operating conditions. Graphite formed with carbon-containing fuels is tracked by Raman spectroscopy on a minute timescale, allowing the study of deposit formation and oxidation. CO, CH_4, C_2H_4, C_3H_6, and C_4H_{10} have been used to correlate fuel molecule structure to the deposit formed. Higher-weight fuels lead to carbon deposits with smaller domain sizes. Singular intermediate-weight fuels (C2 and C3) lead to permanent degradation in cell performance, while extended use of intermediate-weight fuel mixtures and C_4H_{10} result in performance recovery.

These studies present the first identification of intermediates on working SOFC anode surfaces, providing new insight to the fuel oxidation mechanism. Species identified in these studies will enable development of more accurate models of SOFC chemistry.

AN INVESTIGATION OF SOLID OXIDE FUEL CELL CHEMISTRY: A SPECTROSCOPIC APPROACH

By

Michael Brendan Scott Pomfret

Dissertation submitted to the Faculty of the Graduate School of the
University of Maryland, College Park, in partial fulfillment
of the requirements for the degree of
Doctor of Philosophy
2007

Advisory Committee:
Professor Robert A. Walker, Chair
Professor Bryan W. Eichhorn
Professor Sang Bok Lee
Professor Janice E. Reutt-Robey
Professor Gregory S. Jackson, Dean's Representative

Dedication

This thesis is dedicated to my parents Barbara and William and my sister Lindsey.

Acknowledgements

There are many people who deserve credit and thanks for their part in this thesis. Without their contributions and support, this work would not have been possible.

My advisor, Dr. Robert Walker, deserves an incredible amount of credit for the work presented here. His expertise, support, and help guided me through my time at the University of Maryland. His enthusiasm for the project and dedication to my work has truly inspired me. I thank him for making me a better scientist.

The SOFC project is guided by three professors (including Dr. Walker) whose insight, support and critical eye have been invaluable. I would like to thank Drs. Bryan Eichhorn and Gregory Jackson for their stimulating conversations and scientific contributions to this work.

I would also like to thank Professor Robert Kee of the Colorado School of Mines for his insight and some of the illustrations presented in this thesis and Dr. Jeffrey Owrutsky of the Naval Research Laboratory for helping me refine my spectroscopic technique and lending outside influence that really furthered the success of this project.

I would like to thank the members of my committee, including Drs. Sang Bok Lee and Janice Reutt-Robey, for their support.

Members of the fuel cell project deserve a lot of thanks for being my experimental and intellectual partners. They are Dr. Seyed Reihani, Dr. Chad Stoltz, Dr. Mary Sukeshini, Selim Alayoglu, Ben Becker, Oktay Demircan, Steven DeCaluwe, Bahman Habibzadeh, Paul Jawlik, and Young Kyong Jo.

I would like to thank all of my graduate student colleagues for their companionship and insight, whether in the lab or in the office. I have had the good fortune to work with every graduate student member in the history of the Walker Research group. Whether it was only for a semester or for a few years they have all supported me with insight and camaraderie, so I thank Dr. Xiaoyi Zhang, Dr. Bill Steel, Dr. Carmen Huffman, Wendy Heiserman, Suleyman Can, Mike Brindza, Renee Siler, and Debjani Roy. I would especially like to thank Dr. Okan Esenturk, Anthony Dylla, and Bryan Eigenbrodt, who have contributed directly to the spectroscopic fuel cell work.

I would like to thank Dr. Bindu Varughese for her guidance with the XPS experiments.

Finally, and most importantly, I would like to thank my family for their unending love and support through not only my time in graduate school, but throughout my life. Thank you to my parents Barbara and William and my sister Lindsey – I could not have done this without you.

Table of Contents

List of Tables

List of Figures

List of Abbreviations

A	IR absorbance in Chapters 1 and 4
A	anode length X depth of the reduced YSZ surface (Chapter 3)
AC	alternating current
AFM	atomic force microscopy
c	concentration of species in IR measurements
CW	continuous wave
C_λ	Raman coupling coefficient
D	refers to the diagnostic peak of disorder in graphite
DC	direct current
DECO	direct electrochemical oxidation
EIS	electrochemical impedance spectroscopy
EPA	Environmental Protection Agency
ϕ	phase difference between voltage and current in EIS measurements
FTIR	Fourier transform infrared spectroscopy
G	refers to the diagnostic peak of graphite
HOPG	highly ordered pyrolytic graphite
I	current
I_0	intensity of Raman excitation
I_R	intensity of the Raman signal
I_x	intensity of Raman peaks of species "x"
L	pathlength of sample in IR measurements
l	distance between the anode and counter electrode in Chapter 3
L_a	lattice parameter
LSM	lanthanum strontium manganese oxide
MEA	membrane electrode assembly
n	number of molecules in a sample (for Raman measurements)
NCG	nanocrystalline graphite
NdYAG	neodymium-yttrium-aluminum garnet
OCV	open circuit voltage
OD	outer diameter
OP	overpotential
PEMFC	proton exchange membrane fuel cell
P_x	partial pressure of species "x"

R	resistance
R_b	bulk resistance
RMS	root mean square
R_p	polarization resistance
sccm	standard cubic centimeters per minute
SEM	scanning electron microscope
SOFC	solid oxide fuel cell
t	time
TPB	triple phase boundary
ν	incident frequency
V	voltage
ν_0	signal frequency
XPS	X-ray photoelectron spectroscopy
XRD	X-ray diffraction
YSZ	yttria-stabilized zirconia
Z	impedance
Z'	the real part of the impedance
Z"	the imaginary part of the impedance
α_0	polarizability
β	Raman cross section
ε	molar extinction coefficient (IR)
ε_0	electric field (Raman)
μ_{ind}	induced dipole moment
ρ	resistivity
ω	frequency (EIS measurements)

Chapter 1: Introduction

1. Fuel Cells

Inexpensive, reliable electricity is largely responsible for the quality of life to which we have become accustomed. The majority of the electricity used by our society, however, comes power plants that consume non-renewable resources such as oil or coal to turn steam turbines, which that, in turn, generate the power that supplies the grid.[1] At current consumption rates, petroleum reserves will last less than 50 years[2] meaning that the world must look either to alternative sources of energy or to ways of using existing resources much more efficiently. One such source is the electrochemical fuel cell.

Fuel cells are not a new technology. The first cell was reported about 170 years ago.[3] Because fuel cells produce energy directly from electrochemical oxidation, they are both cleaner and more efficient than traditional means of energy production, such as the combustion engine. Furthermore, fuel cells can be used for both portable and stationary applications.[3-6] The solid oxide fuel cell (SOFC), in particular, stands out as a promising alternative energy conversion device thanks, in part, to the fact that it can convert fuel to electricity with a theoretical efficiency of approximately 70%.[2,7]

Ideally, fuel cells would run on hydrogen fuel and cell exhaust would consist solely of water. However, hydrogen is expensive to produce, difficult to store, and highly explosive.[8,9] A hydrogen economy is not viable until these cost and safety

concerns are addressed.[10] Consequently, a lot of solid oxide fuel cell research focuses on developing systems that can utilize a range of fuels.[4,11] Again, SOFCs stand out. SOFCs can operate with a variety of hydrocarbon fuels, including methane and octane.[12-20] Despite this versatility, carbon-containing fuel also pose serious problems to cell operation. Even the simplest carbon fuels, such as methane or carbon monoxide can lead to anode poisoning through carbon deposition onto anode catalysts.[4,7] These deposits can block active sites and greatly reduce or even completely inhibit electric current production. Developing a tested, mechanistic understanding of the chemistry responsible for fuel oxidation may help to prevent poisoning of anode materials.

A schematic representation of a SOFC is shown in Figure I.1. SOFCs employ a solid oxide electrolyte that can transport O^{2-} ions from the cathode to the anode at temperatures of at least 600 °C.[3] The standard electrolyte material is yttria-stabilized zirconia (YSZ), although other materials are being developed to improve cell performance and durability.[21-26] YSZ ($Zr_{0.92}Y_{0.08}O_{1.96}$) is typically a composition of 8-10 mole percent Y_2O_3 balanced with ZrO_2 wherein the yttria dopant creates oxygen vacancies and stabilizes a cubic zirconia structure. As oxide ions reach the anode, they are reduced as they oxidize the fuel to form products and two electrons, which then flow through a circuit thus balancing the ion flow. The cathode is typically made of either platinum or perovskite oxides, such as lanthanum strontium manganite (LSM).[3]

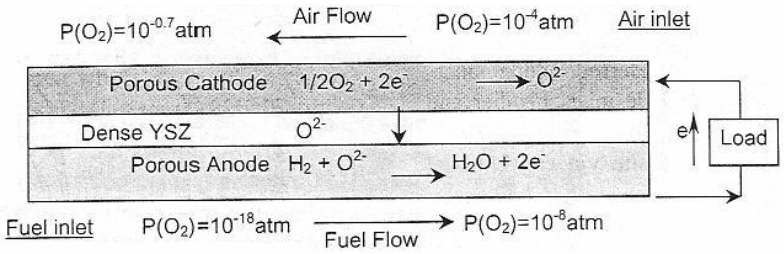

Figure I.1. Scheme of the operation of a solid oxide fuel cell.[7]

Numerous anode types consisting of various ionic and electronic conducting materials in different architectures have been tested for use in SOFCs. The standard anode material is a porous nickel/YSZ mixture known commonly as a cermet.[3] Other possible compositions incorporate ceria, copper, and other metal oxides.[4] Initially, Ni was used as an anode material due to its low cost and ability to catalyze carbon-hydrogen bond breakage.[7] While the cermet architecture remains the standard, many different designs have been tested including patterned anodes, whereby pure metal is deposited directly on the electrolyte.[27-29]

Fuel oxidation and electricity production is thought to occur at the three-phase boundary (TPB) where the metallic anode, the ceramic electrolyte and the gas phase fuel mixture meet. Most studies cite a microscopically narrow TPB as the source of electrochemical activity, although ambiguity exists regarding the TPB's exact dimensions.[30-32] Efforts to expand the TPB have include enhancing anode surface area and periphery, thus increasing in the rate of the reaction.[33] Cermet anodes perform better overall due to the large number of reaction sites achieved by mixing Ni and YSZ.[7,34,35] Patterned anodes, with a better defined TPB, allow for more rigorous, quantitative comparisons between the TPB length, anode surface area and cell performance.[27-29]

The exact mechanisms responsible for fuel oxidation remain mostly speculative because the TPB has never been identified explicitly. Traditional electrochemical methods, such as electrochemical impedance spectroscopy and voltammetry, can report on macroscopic electrochemical behavior but cannot identify the specific reaction pathways of fuel oxidation. One predicted pathway is a mechanism referred to as direct electrochemical oxidation (DECO).[36-42] If a fuel cell were to operate strictly by DECO the reactants would be the fuel and oxygen and they would produce water and CO_2. A balanced reaction with methane as a fuel would be:

$$CH_4 + 2O_2 \rightarrow CO_2 + 2H_2O$$

Lost in this overall reaction are details about how the molecular O_2 is reduced at the cathode and how the CH_4 breaks apart to provide electrons and form oxidized products. Possible reaction pathways include the complete breakdown of CH_4 to the component atoms, a partial breakdown of CH_4 that could result in the formation of partially oxidized fuel species such as carbon monoxide, methanol or formaldehyde. In fuel rich cases, there is also that possibility that some of the fuel, especially the carbon atoms, will not be oxidized. Excess carbon can form deposits on the anode that block reaction sites, reduce catalytic activity, and hinder cell performance.[2,7]

In addition to electrochemical reaction, side products may be created by non-electrochemical processes, such as reforming and pyrolysis. Reforming describes the process by which one fuel species is converted into another and can either help or hurt the efficiency of the cell. For example, hydrocarbons may reform in the presence of water vapor to produce molecular hydrogen and CO, which can then be

electrochemically oxidized to the final products.[12,43-47] In this case reforming is essential to clean fuel oxidation. However, should this reaction occur:

$$2\ CO \rightarrow C + CO_2$$

the elemental carbon can remain on the anode, hindering or completely blocking further anode activity.[48] Pyrolysis is the process by which fuels breakdown in the absence of an oxidizing agent at high temperatures. For example, butane pyrolyzes to a combination of smaller hydrocarbons, including methane, ethylene, and propylene.[49] The exact composition of the pyrolysis product mixture depends on the temperature of the fuel inlet as well as fuel residence time within the inlet. Clearly a limitation to improving fuel cell technology is the uncertainty about the fate of fuels once inside the SOFC apparatus. Pyrolysis poses distinct challenges to the development of kinetic models describing SOFC chemistry because this process changes the composition – and resulting reactivity – of the incident fuel mixture. Due to pyrolysis, a model that predicts the performance of a cell operating on butane fuel cannot focus on the electrochemical oxidation of butane molecules alone. An accurate model would have to take all of the hydrocarbons in the fuel flow that results from butane pyrolysis into account. Furthermore, the pyrolysis product yields change depending on the conditions of the fuel inlet (i.e., temperature, residence time, humidity, etc.).

Complicating the picture of SOFC chemistry even further is the fact that material properties change when subjected to conditions of high heat and strong oxidizing/reducing conditions. For example, previous research has considered the YSZ electrolyte only in terms of its ability to transport oxide ions from the cathode to

the anode.[3] Limited proton spillover chemistry has been suggested and YSZ has been shown to be active in "anodeless" cells, but the possible catalytic role of played by YSZ is still not completely clear.[50,51] Should YSZ catalyze side reactions that aid in hydrocarbon reforming, this electrolyte's impact on the electrochemical oxidation mechanism(s) could be much greater than simply providing oxide ions for the electrochemical reaction. Testing these and other ideas about chemical processes occurring in SOFCs requires noninvasive, molecularly specific techniques that are capable of identifying molecular species that form (and disappear) in functioning cells.

2. Aim of Thesis

The goal of this research is to use various analytical techniques – primarily Raman and Fourier-transform infra-red (FTIR) spectroscopies, voltammetry, and electrochemical impedance spectroscopy (EIS) – to develop an understanding of the fuel oxidation mechanism in SOFCs. Results from these studies can then be used by collaborators to produce more accurate models of SOFC processes and ultimately aid in the design of more efficient SOFCs as well as better protocols for operating existing devices. To accomplish this goal, experiments examine the composition and chemical activity of individual elements related to SOFC anode operation, namely electrolyte material, electrocatalysts, fuels, and cell exhaust. The work presented in this thesis fits into a larger goal of understanding the fundamental chemistry and physics of direct fuel utilization in SOFCs through experimentation and modeling being pursued by a team of researchers at the University of Maryland, Colorado School of Mines, and California Institute of Technology.

The cells examined in this work consist of three-layer membrane electrolyte assemblies (MEAs), supported by the electrolyte layer. All of the cells used in the following experiments have YSZ electrolytes (~ 1 mm thick) and ~20 μm thick LSM cathodes. All of the anodes are either 1:1 by weight Ni:YSZ cermet or 1:1:8 by mole Cu:CeO2:YSZ. MEA architectures specific to each experiment are discussed in the Experimental sections of each chapter. The research presented in this dissertation uses two different approaches to study the mechanism(s) of SOFC anode chemistry.

Ex-situ methods are first used to develop a firm understanding of the material and chemical properties of species involved in SOFC operation. The first set of *ex-situ* experiments employ Raman spectroscopy to investigate the effects of SOFC-like atmospheres on YSZ. The purpose of this study is to identify any chemical transformations that can occur on electrolyte surfaces exposed to conditions commonly encountered in functioning SOFCs, in particular on the anode side. In the second *ex-situ* study FTIR absorbance spectroscopy was used to identify the components of the exhaust of SOFCs operated with various fuels and anode materials.

During the *ex-situ* studies, a parallel effort was underway to design an SOFC that had optical access so that fuel oxidation processes could be studied *in-situ*. After several iterations, a working cell emerged that allowed Raman spectroscopy experiments to identify intermediates resulting from the oxidation reaction of various fuels. The primary intermediate was identified as nanocrystalline graphite. EIS and voltammetry were used to correlate the growth and oxidation of the graphite to cell

performance. The study as a whole has led to unprecedented insight into the chemistry occurring on SOFCs anodes.

3. Technical Overview

Most information about SOFC processes has come from studies using classical electrochemical methods such as impedance spectroscopy and linear sweep voltammetry.[28,52-54] While these techniques can characterize cell performance as a function of operating conditions, optical spectroscopic methods capable of identifying specific chemical species are needed to advance significantly the knowledge about fuel oxidation mechanisms The techniques used by this research to help clarify SOFC oxidation mechanisms include Raman and FTIR spectroscopy. Complementary data came from X-ray diffraction (XRD) and X-ray photoelectron spectroscopy (XPS) measurements.

Raman spectroscopy uses an incident optical beam to excite the sample to a different vibrational state through a scattering mechanism. The reflected beam will scatter at various wavelengths and produce a spectrum. The difference in frequencies between the incident light and the scattered light results in a vibrational spectrum of the sample being studied. The process of Raman scattering is described by the following equation:

$$\mu_{ind} = \alpha_0\varepsilon_0 \cos 2\pi\nu t + (1/2)\,\Delta\alpha\varepsilon_0\,[\cos 2\pi(\nu + \nu_0)t + \cos 2\pi(\nu - \nu_0)t]$$

where an excitation laser with a frequency of ν places a molecule in an electric field with a maximum value of ε_0 that induces a dipole moment (μ_{ind}) that can lead to vibrational excitation. If a vibration (with a frequency of ν_0) results in a change in polarizability ($\Delta\alpha$), it is considered to be Raman active.[55] A schematic of the Raman

processes is shown in Figure I.2. The signal measured in all of the following work is the Stokes radiation ($v - v_0$).

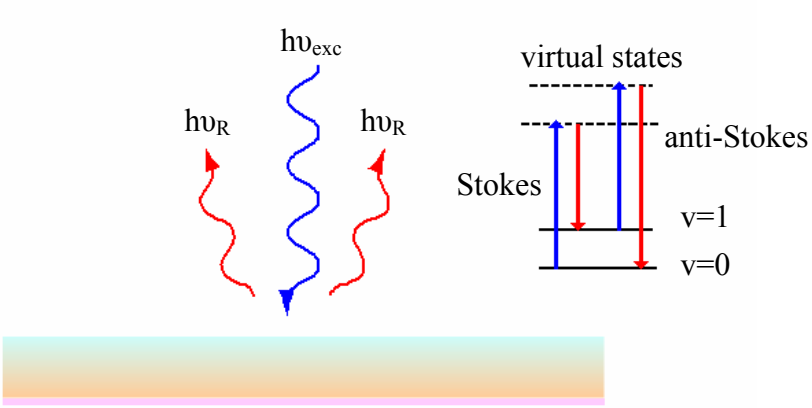

Figure I.2. Scheme showing the process of Raman excitation as well as Stokes and anti-Stokes Raman scattering.

The intensity of the Raman signal (I_R) depends on the Raman cross section (β), the intensity of the excitation (I_0) and the number of molecules present in the sample (n) such that:

$$I_R = n\beta I_0$$

Two examples of Raman spectra presented in this thesis are shown in Figure I.3.

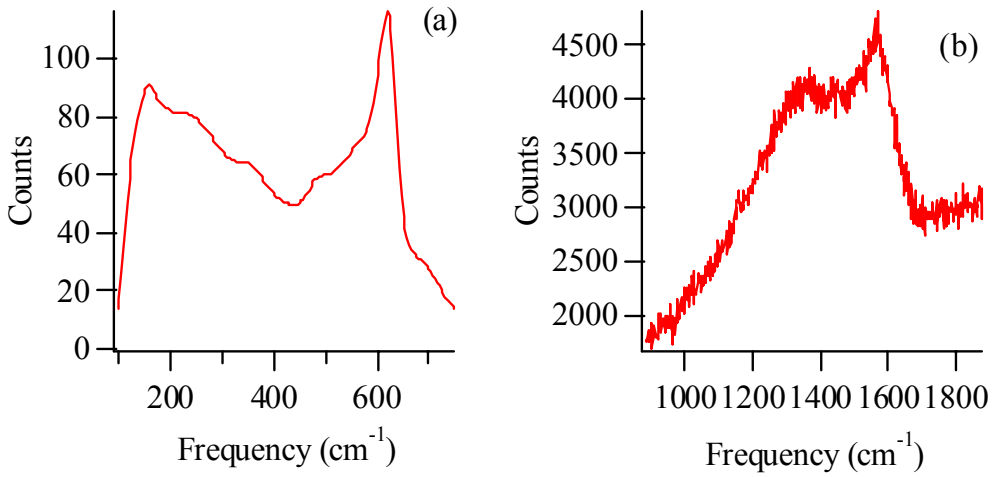

Figure I.3. An *ex-situ* FT-Raman spectrum of YSZ (a) and an *in-situ* (715˚C) dispersive Raman spectrum of nanocrystalline graphite.

The second optical technique used in this study is FTIR spectroscopy. Similar to Raman, an IR source excites molecules causing bonds to bend or stretch. If this vibrational excitation causes a change in dipole moment, the vibration will be IR active.[56] The intensity of the IR absorbance signal (A) is given by the equation:

$$A = \varepsilon cL$$

where ε is the molar extinction coefficient, c is the concentration of the species and L is the sample pathlength.[55] FTIR is used in the analysis of fuel cell exhaust to determine the products formed in the operating SOFCs as a function of fuel identity. Exhaust species have specific IR-active motions with strong, well resolved signals. FTIR is particularly useful for quantitative analysis of exhaust species with precision of three significant decimal figures, allowing for the evaluation of fuel utilization efficiencies.

IR is much more sensitive than Raman due to the direct measurement of absorbance of the incident beam (as opposed to the detection of scattered light in

Raman spectroscopy),[55] but *in-situ* IR studies of working SOFCs are not possible due to blackbody radiation. At SOFC operating temperatures blackbody radiation will produce light across much of the visible spectrum giving rise to undesirably large background, thus reducing experimental signal-to-noise ratios.

Optical spectra can report on the chemical processes that fuel and intermediate species participate in, but they cannot offer information about changes in cell performance that might occur as the chemistry happens. To fully understand how species detected in the optical spectra relate to SOFC anode chemistry, the spectra must be related to results from EIS and voltammetry. Typical electrochemical measurements use a three-point configuration, referring to the number of electrodes attached to the electrolyte.[28,57] The electrodes are designated as working, counter, and reference. For this study, the anode is the working electrode and the cathode functions as both the reference and counter electrodes. Electrochemical methods are used to correlate changes in the overall performance of the cells with changes in optical data.

Voltammetry applies an time-dependent electric potential across the cell and measures the corresponding current produced. The dependence of current on applied potential can give insight into the kinetics and rates of electrochemical processes.[58] Voltammetry plots can be analyzed to give the maximum current and power densities of different SOFC designs allowing for a very clear diagnostic of changes in cell performance. A typical voltammetry and power density plot is shown in Figure I.4.

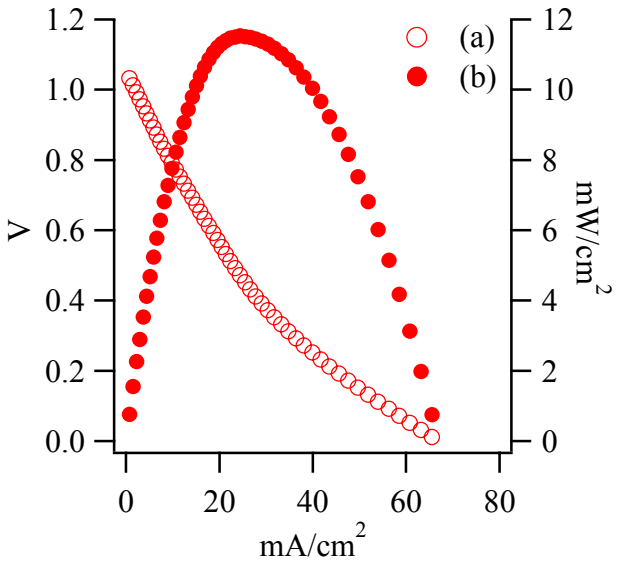

Figure I.4. Typical electrochemical data acquired from an SOFC in this study showing the voltammetry (○) and power density curves (●).

Voltammetry scans (Figure I.4) offer much information about a cell. The maximum cell voltage is referred to as the open circuit voltage (OCV) and is the maximum voltage drop across the cell. At a cell voltage of 0 V the circuit is completely closed and maximum current is being drawn from the cell. This current is reported as a current density (mA/cm^2 in this thesis). Typically, the V-I plot of an SOFC is dominated by charge transfer reactions, but various slopes in a V-I line can give information about different fuel processes. Significant activation barriers appear as a steep slope at high voltages. A flatter slope at low voltages is often due to mass transport issues at the anode. Finally, a power density (mW/cm^2) curve can be calculated by multiplying voltages by the respective current densities. The maximum power output of the cell is given by the peak on this plot.

EIS is used to characterize the resistance associated with the experimental system. These measurements apply an alternating potential difference between the reference and working electrodes. This potential (V) is applied across a range of

frequencies (ω), the resulting current (I) is measured, and the associated electrochemical impedance (Z) is calculated. The impedance at a certain frequency is given by the equation:

$$Z(\omega) = \Delta V(\omega,t) / \Delta I(\omega,t) = (V / I)e^{i\phi}$$

where ϕ is the phase difference between the voltage and the current.[59] The total impedance, as defined above, has two components – the imaginary (Z") and the real (Z') – that are defined below.[59]

$$Z'(\omega) = |Z| \cos \phi$$

$$Z''(\omega) = |Z| \sin \phi$$

The convention for plotting impedance data used in this dissertation is the Nyquist plot. The Nyquist convention plots the negative of the imaginary impedance against the real component of the impedance.[60] Two characteristic resistances can be easily measured in an impedance plot: the polarization resistance (the overall ohmic resistance of the cell, R_p) and the bulk (electrolyte) resistance (R_b). Nyquist plots show arcs that are attributed to different electrochemical occurrences. A typical EIS plot is shown in Figure I.5. Data are plotted as frequency decreases, generally from left to right on the graph. The high frequency x-intercept defines the bulk resistance. The polarization resistance is found by determining the difference between the high frequency and low frequency x-intercepts. In many cases more than one arc is found per plot indicating that multiple electrochemical processes are occurring at the same time. Discussions of EIS data relevant to the systems in this study refer only to the total polarization resistance of the cell.

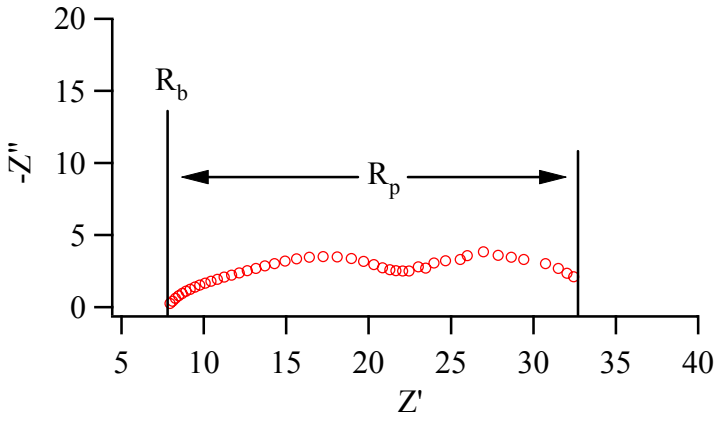

Figure I.5. Typical Nyquist plot of electrical impedance data of a SOFC in this study. The bulk resistance (R_b) and polarization resistance (R_p) are designated.

4. Organization

The remainder of this thesis is organized as follows: Chapter II examines the structural properties of polycrystalline YSZ using FT-Raman spectroscopy, XRD, and XPS. A range of yttria content (by mole fraction) is studied to determine compositional effects on YSZ phonon structure, lattice parameter, and oxidation state. Exposing YSZ to a reducing environment (H_2) at elevated temperatures (1000 ˚C) results in reduced forms of Y and Zr within the first few molecular layers of the sample. The impact that surface-reduced YSZ may have on the chemistry occurring within solid oxide fuel cells is discussed briefly. Chapter III expands on the reduced YSZ discussion by investigating the electrochemical properties of various YSZ surfaces with impedance spectroscopy. Data suggest that YSZ may actively contribute to the electrochemical fuel oxidation process and therefore to electrical current production.

Chapter IV presents FTIR experiments that quantify the exhaust of solid oxide fuel cells (SOFC) operating with fuel flows of methane over Ni/YSZ cermet anodes,

and butane over Ni/YSZ and $Cu/CeO_2/YSZ$ cermet anodes. Data show that hydrocarbon fuels can participate in a variety of different reactions beyond direct electrochemical oxidation. A measure of fuel oxidation efficiency is found by comparing the partial pressure of CO_2 (P_{CO_2}) in the SOFC exhaust to the partial pressure of CO (P_{CO}).

In Chapter V Raman spectroscopy is shown to be capable of identifying *in-situ* and noninvasively changes in SOFC material properties as well as the formation and disappearance of molecular species on surfaces at temperatures of 715 ˚C. Experiments demonstrate the ability of Raman spectroscopy to follow reversible oxidation/reduction kinetics of Ni/NiO as well as the rate of carbon disappearance when graphite, formed *in-situ*, is exposed to a weakly oxidizing atmosphere. In addition the Raman active phonon mode of YSZ shows a temperature dependent shift that correlates closely with the expansion of the lattice parameter, thus providing a convenient internal diagnostic for identifying thermal gradients in high temperature systems. These preliminary high-temperature experiments lead to the study of the anode surface of operating cells. This study presents the first direct, *in-situ* measurements of relevant chemical species formed on SOFC cermet anodes operating with carbon containing fuels, specifically butane and carbon monoxide.

Chapters VI and VII describe experiments that investigate cells operating on smaller hydrocarbons – methane, ethylene, and propylene – both as singular fuels and as fuel mixtures. All of the fuel flows form graphitic intermediates. In the presence of an oxide flux, these intermediates are transient. Concurrent voltammetry studies

show that the formation of graphite at OCV leads to changes in cell performance that depend on the type of graphite formed with specific fuel species or fuel combinations.

Chapters II through VII are all modified versions of manuscripts that have either appeared in press, have been submitted for review (Chapters VI and VII), or are in preparation for submission (Chapter III). As a result, there is some redundancy throughout this thesis, especially in the introductory comments at the start of each chapter. Overall conclusions and speculation for future directions are discussed in Chapter VII. The design of the *in-situ* optical fuel cell assembly, data representative of a typical experiment in which *in-situ* Raman spectroscopy was used and contributions of collaborating authors are discussed in the appendices.

5. References

(1) Schnapp, R. Electric Power Annual; Energy Information Administration, 2006. http://www.eia.doe.gov/cneaf/electricity/epa/epa_sum.html.

(2) Song, C. S. *Catal. Today* **2002**, *77*, 17.

(3) Ormerod, R. M. *Chem. Soc. Rev.* **2003**, *32*, 17.

(4) Atkinson, A.; Barnett, S.; Gorte, R. J.; Irvine, J. T. S.; McEvoy, A. J.; Mogensen, M.; Singhal, S. C.; Vohs, J. *Nature Materials* **2004**, *3*, 17.

(5) Jacobson, M. Z.; Colella, W. G.; Golden, D. M. *Science* **2005**, *308*, 1901.

(6) Minh, N. Q. *Solid State Ionics* **2004**, *174*, 271.

(7) Zhu, W. Z.; Deevi, S. C. *Mater. Sci. Eng.* **2003**, *A362*, 228.

(8) Carpenter, A. R.; Hinze, P. C. *Process Safety Progress* **2004**, *23*, 292.

(9) Shayegan, S.; Hart, D.; Pearson, P.; Joffe, D. *J. Power Sources* **2006**, *157*, 862.

(10) McDowall, W.; Eames, M. *Energy Policy* **2006**, *34*, 1236.

(11) Farrauto, R.; Hwang, S.; Shore, L.; Ruettinger, W.; Lampert, J.; Giroux, T.; Liu, Y.; Ilinich, O. *Annu. Rev. Mater. Res.* **2003**, *33*, 1.

(12) Iida, T.; Kawano, M.; Matsui, T.; Kikuchi, R.; Eguchi, K. *J. Electrochem. Soc.* **2007**, *154*, B234.

(13) Kee, R. J.; Zhu, H. Y.; Goodwin, D. G. *Proc. Combust. Inst.* **2005**, *30*, 2379.

(14) Liu, J. *Prog. Chem.* **2006**, *18*, 1026.

(15) McIntosh, S.; Vohs, J. M.; Gorte, R. J. *J. Electrochem. Soc.* **2003**, *150*, A470.

(16) Tanaka, Y.; Nguyen, T. L.; Kato, T.; Shimada, T.; Sugano, K.; Negishi, A.; Kato, K.; Nozaki, K. *Solid State Ionics* **2006**, *177*, 3323.

(17) Ye, X. F.; Huang, B.; Wang, S. R.; Wang, Z. R.; Xiong, L.; Wen, T. L. *J. Power Sources* **2007**, *164*, 203.

(18) Zhan, Z.; Barnett, S. A. *Solid State Ionics* **2005**, *176*, 871.

(19) Zhan, Z. L.; Barnett, S. A. *Science* **2005**, *308*, 844.

(20) Zhu, W.; Xia, C. R.; Fan, J.; Peng, R. R.; Meng, G. Y. *J. Power Sources* **2006**, *160*, 897.

(21) Ishihara, T.; Yan, J. W.; Shinagawa, M.; Matsumoto, H. *Electrochim. Acta* **2006**, *52*, 1645.

(22) Nesaraj, A. S.; Kumar, M.; Raj, I. A.; Radhakrishna, I.; Pattabiraman, R. *J. Iranian Chem. Soc.* **2007**, *4*, 89.

(23) Rupp, J. L. M.; Drobek, T.; Rossi, A.; Gauckler, L. J. *Chem. Mater.* **2007**, *19*, 1134.

(24) Shao, Z. P.; Haile, S. M.; Ahn, J.; Ronney, P. D.; Zhan, Z. L.; Barnett, S. A. *Nature* **2005**, *435*, 795.

(25) Wang, C.; Xui, L. H.; Tang, W. H. *Rare Metal Mater. Eng.* **2006**, *35*, 501.

(26) Zhang, X.; Robertson, M.; Deces-Petit, C.; Qu, W.; Kesler, O.; Maric, R.; Ghosh, D. *J. Power Sources* **2007**, *164*, 668.

(27) Bieberle, A.; Gauckler, L. J. *Solid State Ionics* **2000**, *135*, 337.

(28) Bieberle, A.; Meier, L. P.; Gauckler, L. J. *J. Electrochem. Soc.* **2001**, *148*, A646.

(29) Sukeshini, A. M.; Habibzadeh, B.; Becker, B. P.; Stoltz, C. A.; Eichhorn, B. W.; Jackson, G. S. *J. Electrochem. Soc.* **2006**, *153*, A705.

(30) Bove, R.; Ubertini, S. *J. Power Sources* **2006**, *159*, 543.

(31) Fukunaga, H.; Ihara, M.; Sakaki, K.; Yamada, K. *Solid State Ionics* **1996**, *86-8*, 1179.

(32) Nam, J. H.; Jeon, D. H. *Electrochim. Acta* **2006**, *51*, 3446.

(33) Brown, M.; Primdahl, S.; Mogensen, M. *J. Electrochem. Soc.* **2000**, *147*, 475.

(34) Haslam, J. J.; Pham, A. Q.; Chung, B. W.; DiCarlo, J. F.; Glass, R. S. *J. Am. Ceram. Soc.* **2005**, *88*, 513.

(35) Mogensen, M.; Skaarup, S. *Solid State Ionics* **1996**, *86-8*, 1151.

(36) Feng, B.; Wang, C. Y.; Zhu, B. *Electrochem. Solid State Lett.* **2006**, *9*, A80.

(37) Hirabayashi, D.; Hashimoto, A.; Hibino, T.; Harada, U.; Sano, M. *Electrochem. Solid State Lett.* **2004**, *7*, A108.

(38) Ihara, M.; Hasegawa, S. *J. Electrochem. Soc.* **2006**, *153*, A1544.

(39) Lin, Y. B.; Zhan, Z. L.; Liu, J.; Barnett, S. A. *Solid State Ionics* **2005**, *176*, 1827.

(40) Nabae, Y.; Yamanaka, I.; Hatano, M.; Otsuka, K. *J. Electrochem. Soc.* **2006**, *153*, A140.

(41) Sin, A.; Kopnin, E.; Dubitsky, Y.; Zaopo, A.; Arico, A. S.; La Rosa, D.; Gullo, L. R.; Antonucci, V. *J. Power Sources* **2007**, *164*, 300.

(42) Walters, K. M.; Dean, A. M.; Zhu, H. Y.; Kee, R. J. *J. Power Sources* **2003**, *123*, 182.

(43) Faungnawakij, K.; Kikuchi, R.; Eguchi, K. *J. Power Sources* **2007**, *164*, 73.

(44) Goula, G.; Kiousis, V.; Nalbandian, L.; Yentekakis, I. V. *Solid State Ionics* **2006**, *177*, 2119.

(45) Laosiripojana, N.; Assabumrungrat, S. *J. Power Sources* **2007**, *163*, 943.

(46) Liu, D. J.; Krumpelt, M.; Chien, H. T.; Sheen, S. H. *J. Mater. Eng. Perform.* **2006**, *15*, 442.

(47) Zhu, H. Y.; Kee, R. J. *J. Electrochem. Soc.* **2006**, *153*, A1765.

(48) Holtappels, P.; De Haart, L. G. J.; Stimming, U.; Vinke, I. C.; Mogensen, M. *J. Appl. Electrochem.* **1999**, *29*, 561.

(49) Sheng, C. Y.; Dean, A. M. *J. Phys. Chem. A* **2004**, *108*, 3772.

(50) Jiang, S. P.; Badwal, S. P. S. *J. Electrochem. Soc.* **1997**, *144*, 3777.

(51) Hirabayashi, D.; Tomita, A.; Brito, M. E.; Hibino, T.; Harada, U.; Nagao, M.; Sano, M. *Solid State Ionics* **2004**, *168*, 23.

(52) Bebelis, S.; Neophytides, S. *Solid State Ionics* **2002**, *152-153*, 447.

(53) Bieberle, A.; Gauckler, L. J. *Solid State Ionics* **2002**, *146*, 23.

(54) Sunde, S. *Electrochim. Acta* **1997**, *42*, 2637.

(55) Harris, D. C.; Bertolucci, M. D. *Symmetry and Spectroscopy: An Introduction to Vibrational and Electronic Spectroscopy*; Dover Publications, Inc.: New York, 1978.

(56) Skoog, D. A.; Holler, F. J.; Nieman, T. A. *Principles of Instrumental Analysis*, 5th Ed. ed.; Brooks/Cole Thompson Learning: Crawfordsville, MD, 1998.

(57) Zheng, R.; Zhou, X. M.; Wang, S. R.; Wen, T. L.; Ding, C. X. *J. Power Sources* **2005**, *140*, 217.

(58) Wang, J. *Analytical Electrochemistry*, 2nd Ed. ed.; John Wiley & Sons, Inc.: New York, 2000.

(59) Bieberle, A. The Electrochemistry of Solid Oxide Fuel Cell Anodes: Experiments, Modeling, and Simulations. PhD thesis, Swiss Federal Institute of Technology, 2000.

(60) Bard, A. J.; Faulkner, L. R. *Electrochemical Methods: Fundamentals and Applications*, 2nd Ed. ed.; John Wiley & Sons, Inc.: New York, 2001.

Chapter 2: Structural and Compositional Characterization of Yttria Stabilized Zirconia (YSZ): Evidence of Surface Stabilized, Low Valence Metal Species

1. Introduction

Due to its ability to conduct oxygen anions at temperatures above 600 °C, yttria stabilized zirzonia (YSZ) has seen extensive use as a solid state electrolyte in a wide variety of solid oxide fuel cells (SOFCs).[1-3] At temperatures up to 1150 ˚C, zirconia exists in a monoclinic structure. Only at temperatures above 2400 ˚C does zirconia adopt a cubic, fluorite stucture (at atmospheric pressure), as shown in Figure II.1.[4] However, doping ZrO_2 with yttria (Y_2O_3) stabilizes the cubic phase for dopant concentrations ≥ 8% (by mole fraction).[4,5] Doping zirconia with yttria replaces two equivalents of ZrO_2 with a single equivalent of Y_2O_3 and creates oxygen vacancies in the crystal lattice. These oxygen vacancies are responsible for O^{2-} conductivity and, consequently, this ceramic's popularity in electrochemical applications. Oxide anion conductivity in YSZ is quite low at room temperature and only becomes adequate for anode supported fuel cell applications at temperatures above ~600˚ C. Given these high operating temperatures, probing the structure and composition of YSZ during SOFC operation poses considerable experimental challenges. Numerous studies have sought to characterize the properties of cubic YSZ.[4-14] X-ray diffraction measurements have shown how the cubic lattice parameter expands both with increasing Y_2O_3 concentration and with increasing temperature.[14] Raman studies of cubic YSZ have assigned up to ten features associated with the material's low

frequency phonon spectrum.[10] The dominant band in the Raman spectrum appears near 618 cm^{-1} and is assigned to a triply degenerate F_{2g} mode associated with pairs of oxygen atoms in the crystal lattice moving out of phase with one another.[10] The vibrational spectrum of YSZ depends on temperature only very weakly.

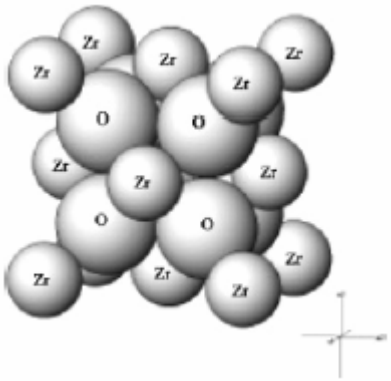

Figure II.1. The fluorite-type cubic zirconia crystal structure. Cubic ZrO_2 is thermodynamically favored only at temperatures above 2400 °C but becomes stable at room temperature when doped with Y_2O_3. Figure taken from http://unit.aist.go.jp/greenlife/ii/english/itscgallary-e.htm and used with permission, see reference.[15]

Experiments described below correlate the structural and compositional properties of YSZ with its optical signatures as measured by FT-Raman spectroscopy. Motivating this work is the need to develop diagnostic methods for examining the high temperature surface chemistry that occurs in SOFCs where YSZ plays a prominent role both as a solid state electrolyte and as a component of cermet anodes. The most direct way to measure structure and surface composition in these high temperature systems is to use X-ray based techniques, either X-ray diffraction or X-ray photoelectron spectroscopy. However, the elaborate experimental geometries required to carry out these experiments are often incompatible with functional SOFC assemblies.[1] As a means of probing the properties of YSZ *in-situ* during fuel cell operation, Raman spectroscopy stands out as an attractive technique because it is less

sensitive to background, blackbody radiation and low frequency vibrational bands can be measured with high accuracy. In addition, Raman signals can be enhanced by selectively doping materials with chemically inert particulates.[16,17]

Data show that the lattice parameter of cubic YSZ corresponds quite closely to the frequency of the F_{2g} band meaning that Raman spectroscopy can be used to monitor directly and noninvasively the structure of this common SOFC material. Furthermore, the Raman intensity of YSZ depends quite sensitively on the material's history. Raman spectra of YSZ that has been exposed to a high temperature reducing environment shows a dramatic and reproducible reduction in its scattering intensity. Furthermore, this change is reversible and scattering intensities return to their previous levels following high temperature oxidation. These changes are not reflected in the lattice parameter, which stays constant, but X-ray photoelectron spectroscopy measurements show clearly that new, reduced species of yttrium and zirconium are created on the YSZ surface. These low oxidation metals likely change the reflectivity and polarizability of the YSZ sample leading to the observed changes in the low frequency Raman spectra. Furthermore, reduced forms of zirconium (Zr^{3+} and Zr^{2+}) have been shown to be very efficient catalysts in organic and polymer synthesis.[13,18] Should the reduced YSZ created in this work have catalytic properties with comparable activities to electrocatalyst materials, then many existing models of fuel cell oxidation mechanisms will have to be re-examined to consider alternative reactions (other than charge transfer reactions) that are accessible on the electrolyte surface.

2. Experimental

2A. Sample Preparation

Yttria-stabilized zirconia (YSZ) was synthesized with varying yttria content using materials obtained from Aldrich Chemical Company, Inc. Yttrium nitrate tetrahydrate and zirconyl nitrate hydrate, both 99.99% pure, were dissolved in minimal amounts of water to produce mixtures containing 1, 2, 5, 8, 10, and 15% yttria by mass doped zirconia. Once the materials were completely dissolved the water was evaporated off with gentle heating. This approach led to more uniform mixing of precursors than could be obtained from grinding in a mortar and pestle. The resulting mixtures were heated at 1000 °C for six days and then cooled to room temperature. At yttria concentrations below 8% the YSZ did not quantitatively form a single phase material. Rather, the samples showed evidence of tetragonal and monoclinic phases as well as a cubic phase.

Polycrystalline YSZ (8% yttria) – obtained from ITN Energy Systems, Inc. – had the same lattice parameter and exhibited a Raman response equivalent to the 8% YSZ samples synthesized according to the above procedure. The ITN YSZ wafers (1.2 cm dia., 2mm thick) are being used in our ongoing studies of direct electrochemical oxidation in SOFCs.[19] These commercial samples were subjected to two heating cycles, one in an oxidizing environment of air, the other in 5% H_2 and 95% Ar – a reducing atmosphere. Each cycle lasted for six hours before samples were cooled to room temperature.

2B. Sample Analysis

All Raman spectra were obtained with a ThermoNicolet Nexus 670 FTIR spectrometer with a Raman accessory using Omnic v6.1 software. Samples were irradiated with 0.5 Watt from a CW NdYAG laser (1064 nm). Resolved band positions are accurate to within 4 cm^{-1} while absolute signal intensities reproduced to within 10% for a given YSZ sample. As we note below, signal intensity did depend sensitively on sample roughness with signals from polycrystalline samples exceeding single crystal intensities by a factor of 10.

XRD data were acquired using a Bruker C2 Discover X-ray Powder Diffractometer with a HiStar area detector and CuK_α radiation. Six frames were collected with the area detector and merged to give 2θ scan ranges from 4° to 90°. Unit cell indexing and refinements were carried out using the MDI Jade software package.

AFM images and RMS roughness values were obtained with Molecular Imaging Pico Plus microscope using MAClevers SN, type II tips in tapping mode in air. Reported images and data are representative of numerous scans taken at randomly chosen locations on the YSZ wafers from ITN.

The X-ray photoelectron spectroscopy measurements were carried out using a Kratos Axis 165 spectrometer at a vacuum of $4x10^{-10}$ Torr with monochromatic Al Kα radiation. The X-ray power used for the measurements was 144 W. A wide scan survey as well as various element specific regions (Y 3d, Zr 3d, O 1s and C 1s) were measured. All measurements were carried out in hybrid lens mode using both electrostatic and magnetic lenses with a step size of 0.1 eV and sweep time of 60 s.

Survey spectra were only 2 scans with a pass energy of 160 eV. All individual region spectra were recorded in the FAT analyzer mode with pass energy of 80 eV, and an average of 10 scans. The charge neutralizer was on during the measurements to compensate for surface charging and binding energies were calibrated with respect to C 1s at 284.6 eV. Angle-resolved spectra were obtained by adjusting the sample tilt to 35º and 70º from the plane of the standard surface. Argon ion milling of non-angle-resolved samples was carried out at a pressure of 3.2×10^{-7} Torr for 5 minutes etch time and the parameters used for etching are 15 mA and 4KV. Data processing is done using Vision processing software. After subtraction of a linear background, all spectra are fitted using 60% Gaussian / 40% Lorentzian peaks, taking the minimum number of peaks consistent with the best fit.

3. Results and Discussion

Cubic zirconia has a fluorite-type crystal structure, as in Figure II.1. At room temperature and atmospheric pressure, the thermodynamically stable phase of ZrO_2 is monoclinic. However, when doped with $\geq$ 8% yttria the ZrO_2 crystal structure adopts the fluorite structure. A room temperature Raman spectrum of 8% YSZ appears in Figure II.2. Only the Stokes shifted signal was collected. The sharp features between 2400 and 3500 cm^{-1} arise from ytrria fluorescence and do not appear when YSZ is probed using other wavelengths. The low frequency structure (100-700 cm^{-1}) is attributed to the phonon structure of cubic YSZ (Figure II.3). The most prominent peak at 618 cm^{-1} is attributed to the F_{2g} mode of the YSZ lattice.[10] This band corresponds to the out-of-phase stretching of the oxygen bound to zirconium. Other low frequency features can be discerned in the spectrum and these all correlate

closely to previously reported results.[10] The XRD pattern of 8% YSZ is shown in Figure II.4 and the measured lattice was found to be 5.143 $\pm$ 0.001 Å, in agreement with previously reported results.[10] Raman spectra of single crystal YSZ were identical to the polycrystalline spectra except for a 100x reduction in scattering intensity.

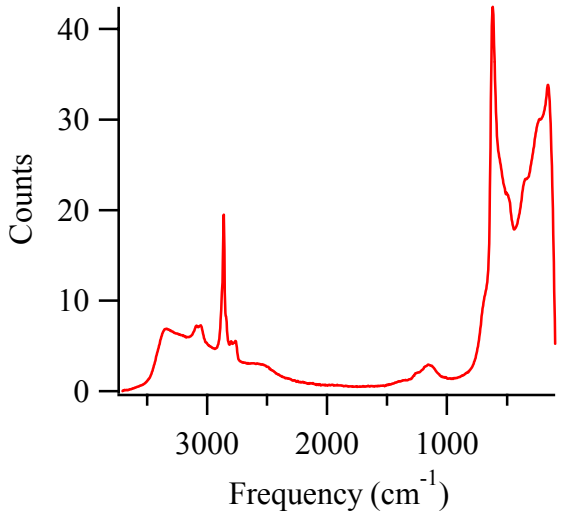

Figure II.2. The full stokes Raman spectrum of YSZ. The band structure from 100 to 800 cm^{-1} is characteristic of the cubic YSZ phonon modes. The bands at higher frequencies are attributed to sample fluorescence caused by the 1064 nm laser.

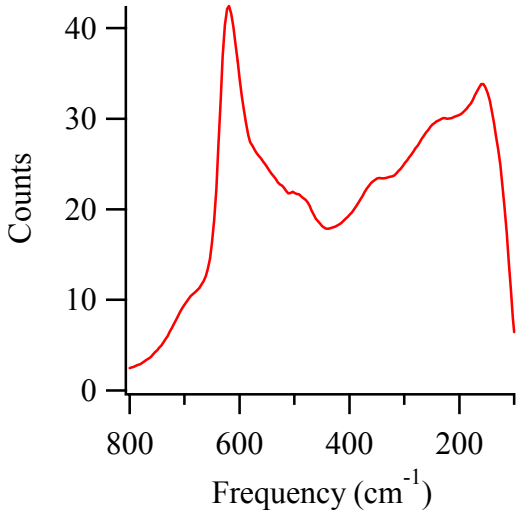

Figure II.3. The low energy spectrum of YSZ. The dominant peak at 617 cm^{-1} is characteristic of the F_{2g} phase of the cubic YSZ structure.

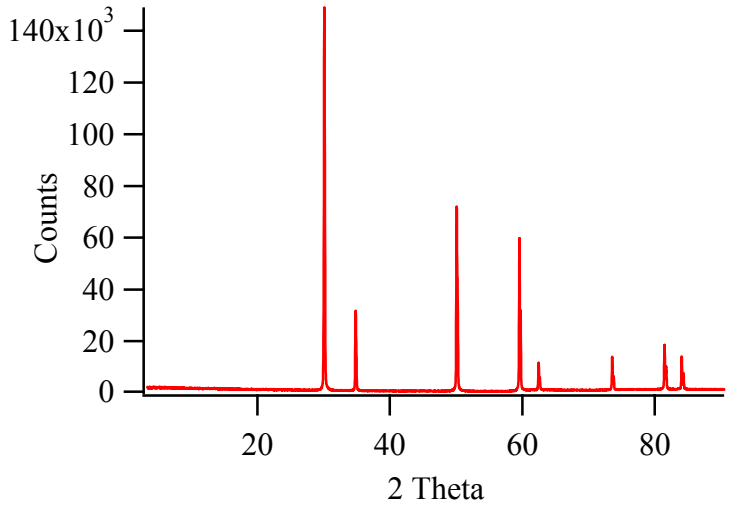

Figure II.4. A typical X-ray diffraction pattern of polycrystalline YSZ with 8% yttria content by weight. The cubic lattice parameter of this sample is 5.143 Å.

3A. YSZ Synthesis

All six zirconia samples were characterized with Raman spectroscopy and XRD as a function of percent yttria composition. The analysis of the 1% and 2% samples found predominantly monoclinic zirconia characteristics. The 5% yttria

sample produced a Raman spectrum that compared more closely to that of tetragonal zirconia. The XRD pattern, however, is strongly associated with the cubic YSZ pattern. The 8%, 10% and 15% samples all exhibited behavior characteristic of the cubic phase and for this reason, only these samples are discussed below.

The XRD and Raman data for cubic YSZ show two clear progressions (Figure II.5). As the percentage of Y_2O_3 increases, the Raman signal shifts to lower frequencies and the lattice parameter increases. The characteristic Raman peak associated with the cubic phase phonon structure shifts from 617 cm^{-1} to 598 cm^{-1}. For the same samples the lattice parameter grew from 5.143 Å to 5.152 Å. In the harmonic approximation these observations are internally consistent. A larger lattice parameter should lead to a softening of the forces within the crystal lattice and a corresponding shift in phonon bands to lower energy. Given the excellent correlation between peak position and lattice parameter, the data suggest that Raman spectroscopy can serve as an important tool in characterizing YSZ composition in applications that are not amenable to XRD measurements.

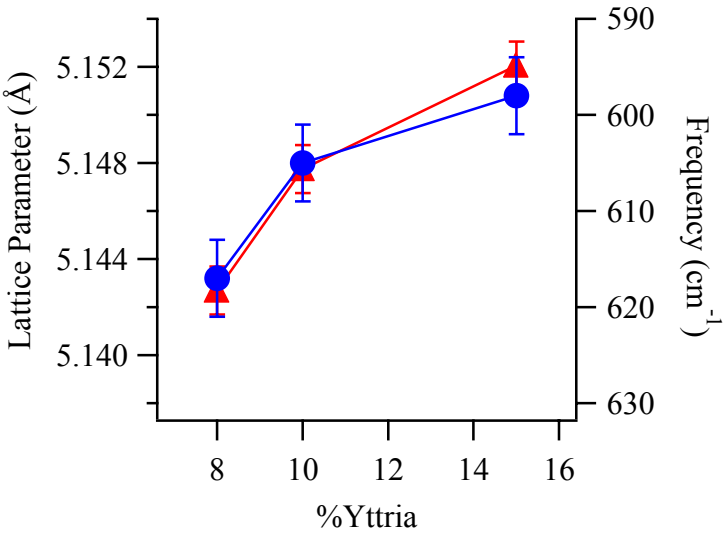

Figure II.5. The relationship between weight percent yttria, lattice parameter (▲), and peak position (●). The lattice parameter increases with increased yttria content, while the peak position shifts to lower wavenumbers. Details of data acquisition appear in the text.

3B. Environmental Conditioning of YSZ

Polycrystalline YSZ samples exposed to reducing environments – 5% H_2 in Ar for six hours at 1000 °C – show a 50% decrease in Raman scattering intensity compared to the oxidized samples (Figure II.6). This change is both reversible and stable. Raman spectra of YSZ samples taken one month after reduction agreed quantitatively with spectra acquired from the same reduced sample immediately after it was removed from the oven. Furthermore, exposing the sample to air at 1000 °C for six hours led to a reoxidized sample whose Raman spectrum was indistinguishable from that of the original sample. One should note that the peak position remained constant at 617 cm^{-1} throughout these cycles, indicating that to within experimental resolution there was no change in lattice parameter or percent yttria. XRD patterns of both reduced and oxidized samples revealed identical lattice parameters, within

instrument resolution, supporting the Raman result. Also, the change in the Raman intensity is reversible by heating the reduced samples in air. Figure II.7 clearly shows that the effects of the two heating environments are both reversible and repeatable.

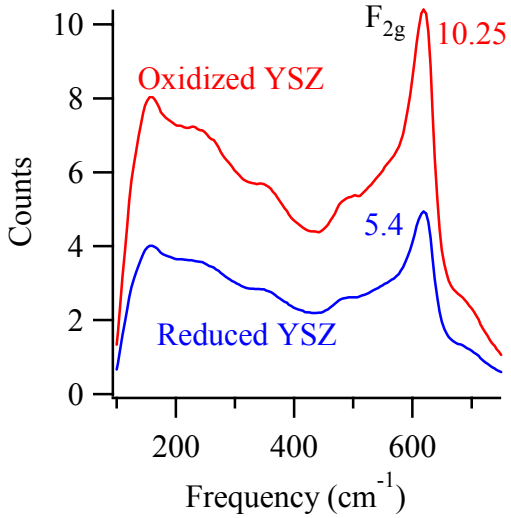

Figure II.6. The effect of a reducing atmosphere on YSZ Raman signal intensity. Exposure to a reducing environment at high temperature precipitates a drop in Raman signal intensity of 25-50% compared to oxidized sample. Peak structure and position is unchanged indicating no change in the chemical composition of the bulk crystal structure.

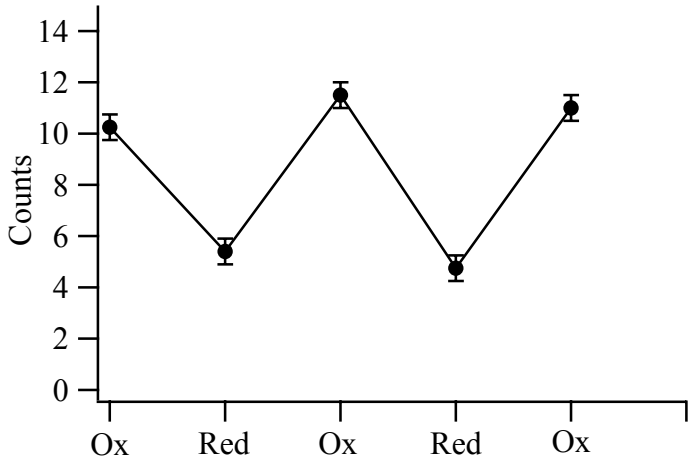

Figure II.7. The effect of atmospheric cycling. The change in Raman signal intensity due to the reducing atmosphere is shown to be both reversible and repeatable with the same sample, indicating that adverse effects of the a reduced surface, if any, can be cured through oxidation.

A loss in Raman signal intensity from the sample could arise from two sources. The first explanation would be a change in the surface roughness. Rougher samples tend to promote Raman scattering efficiency while Raman signals from molecularly flat samples are typically quite small. Thus, if the exposure to hydrogen led to a significant reduction in topographical roughness, one might expect a decrease in Raman intensity. This atmospherically induced reorganization would have to be reversible given the quantitative return of scattering intensity following reoxidation. However, AFM measurements indicate that the surface roughness of both oxidized and reduced samples were equivalent within instrument uncertainties. The root mean square roughness values for the oxidized and reduced polycrystalline samples were 145.8 ± 6.6 nm and 149.8 ± 22.0 nm, respectively. These values reflect the roughness over multiple 7 μm x 7 μm patches selected at random on the YSZ surface. If anything, the reduced samples are rougher given the larger uncertainty in the rms roughness value.

A second source of diminished Raman signal could be a change in polarizability and/or reflectivity as a result of chemically transforming the material. In the literature a reduction in signal intensity has been attributed to the increased number of oxygen vacancies in YSZ crystals.[20] Such a phenomenon would increase the concentration of cationic metal ions relative to oxide ions, a result that would reduce sample polarizability and increase the surface reflectivity. Both effects would serve to diminish the Raman signal.

For a given sample, XRD data show no change in lattice parameter following reduction and/or oxidation. The Raman spectra, however, show pronounced differences that may be attributable to a chemical change within the YSZ. One solution to these apparently contradictory results requires considering the origin of signal observed in the Raman spectra and XRD patterns. Given the sampling depths of the two techniques, Raman spectroscopy samples just a few hundred nanometers at most, while XRD has a penetration depth of several microns, we might anticipate that a change in surface polarization would not be detected in XRD. Furthermore, this change in composition must be small enough on the length scale sampled by the incident Raman excitation field that the observed peak position (at 618 cm^{-1}) does not change. One can imagine that if the YSZ surface becomes more reflective, less light penetrates leading to a decrease in signal intensity.

To better understand the surface composition of polycrystalline YSZ, we carried out XPS measurements on both oxidized and reduced samples. The oxidized samples gave rise to a doublet peak for both metals, 181.8 eV and 184.2 eV for Zr (3d) 5/2 and 3/2, respectively; and 157.1 eV and 159.2 eV for Y (3d) 5/2 and 3/2,

respectively. Reduced samples again showed these peaks as well as a second set of features at slightly lower values. The lower energy features of the reduced YSZ clearly suggest that the chemical composition of the YSZ surface has changed leaving a reduced form of zirconia that is both air and humidity stable. Figure II.8 shows the Y and Zr 3d peaks for both the reduced and oxidized samples and peak positions are reported in Table 1. We note that experiments carried out with single crystal YSZ were qualitatively consistent with those of polycrystalline samples, but the quantitative extent of reduction was much less reproducible.

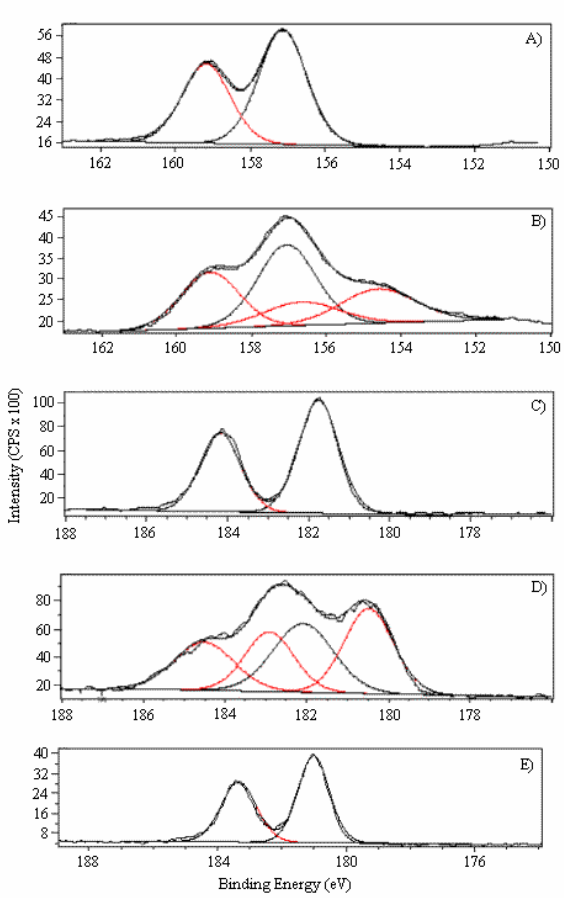

Figure II.8. X-ray photoelectron spectra of Y (A) and Zr (C) 3d electrons in YSZ, showing the effects of reduction on surface composition. Bands appearing at lower binding energies in reduced samples indicate a reduced oxidation state of both the Y (B) and Zr (D) atoms. An angle resolved spectrum at 70º from the surface normal (E) shows the extent to which the surface of the wafer is reduced. All traces of the higher energy, oxidized Zr bands are absent.

The sampling depth of XPS is much less than that of Raman spectroscopy, thus XPS experiments are much more sensitive to surface species. Ion milling even more clearly illustrate that the reduce species was only a surface feature as the lower energy feature was easily removed with one ion-milling pass. Ion milling removes less than a nanometer of material from the sample surface. Furthermore, ion milling is carried out in the absence of oxygen meaning that if the milling endured additional change we would expect to observe additional reduced zirconia, not less. Thus, the

observed change in YSZ composition likely does not result from changes in its bulk crystal structure and should not have much effect on the ion conducting ability of the YSZ.

Angle-resolved XPS measurements were carried out to isolate the reduced surface. The sample was rotated to 35º and 70º from its original surface plane to achieve a grazing angle. At 70º the species present in the reduced YSZ spectrum is clearly zirconium in a low (<4+) oxidation state (Figure II.8, Table II.1). As stated earlier this phase is both air and humidity stable, attributes not associated with metallic zirconium. We speculate that the YSZ surface consists of a valence form of yttria stabilized zirconia that is stabilized by either the relative roughness of the polycrystalline surface or the corresponding high concentration of grain boundaries that are necessarily present at the surface layer. Preliminary studies of a single crystal YSZ surfaces have not returned conclusive results.

Table II.1: YSZ XPS Peak Positions

Feature	Oxidized	Reduced	Reduced (70º)
Zr (5/2)	181.8	182.1,180.5	181.3
Zr (3/2)	184.2	184.5, 182.9	183.7
Y (5/2)	157.1	157.0, 154.6	
Y (3/2)	159.2	159.1, 156.7	

Table II.1. Binding energies of Y and Zr features in 3d XPS spectra. Reported values are accurate to with in ±0.2 eV.

Where reduced YSZ may play a prominent role is in promoting chemical reactions on the MEA surface that have not been considered previously. This concern is particularly relevant if hydrocarbon powered SOFCs should operate under oxygen poor conditions. Low oxidation Zr compounds are commonly used in organic synthesis and as catalysts,[18] making CH and CC bond activation a real concern when

considering DECO in SOFCs. Non-electrochemical side reactions could take away from fuel conversion efficiency and contribute to residues known to impede anode operation. On the other hand, the catalysis of reforming side reactions may lead to better cell performance by breaking down more complex fuels into smaller components that are more easily oxidized at the anode.

4. Conclusion

The present work examines the structural and compositional properties of YSZ with the goal of establishing benchmark measurements that can be used to monitor SOFC chemistry *in-situ*. Data show that the low frequency phonon structure correlates quite closely with the YSZ lattice parameter over the range of Y_2O_3 dopant levels commonly used in SOFC applications. Exposing polycrystalline YSZ samples to a reducing environment at high temperatures leads to a chemical reduction of both the yttrium and zirconium to a lower valence. This effect appears to be restricted to the surface, extending no more than a few nanometers into the sample based on angle resolved and ion milling XPS measurements. These findings have implications in fuel cell research where structure and composition of electrolytes affect electrochemical operation.

5. References

(1) Ormerod, R. M. *Chem. Soc. Rev.* **2003**, *32*, 17.

(2) Song, C. S. *Catal. Today* **2002**, *77*, 17.

(3) Zhu, W. Z.; Deevi, S. C. *Mater. Sci. Eng.* **2003**, *A362*, 228.

(4) Feinberg, A.; Perry, C. H. *J. Phys. Chem. Solids* **1981**, *42*, 513.

(5) Hattori, M.; Takeda, Y.; Sakaki, Y.; Nakanishi, A.; Ohara, S.; Mukai, K.; Lee, J.-H.; Fukui, T. *J. Power Sources* **2004**, *126*, 23.

(6) Lee, T. A.; Navrotsky, A.; Molodetsky, I. *J. Mater. Res.* **2003**, *18*, 908.

(7) Kilo, M.; Argirusis, C.; Borchardt, G.; Jackson, R. A. *Phys. Chem. Chem. Phys.* **2003**, *5*, 2219.

(8) Fujiwara, Y.; Sakai, T.; Kaimai, A.; Yashiro, K.; Nigara, Y.; Kawada, T.; Mizusaki, J. *J. Electrochem. Soc.* **2003**, *150*, E543.

(9) Hughes, A. E.; Sexton, B. A. *J. Mater. Sci.* **1989**, *24*, 1057.

(10) Mori, M.; Hiei, Y.; Itoh, H.; Tompsett, G. A.; Sammes, N. M. *Solid State Ionics* **2003**, *160*, 1.

(11) Garcia, G.; Figueras, A.; Merino, R. I.; Orera, V. M.; Llibre, J. *Thin Solid Films* **2000**, *370*, 173.

(12) Faber, J.; Mueller, M. H.; Cooper, B. R. *Phys. Rev. B* **1978**, *17*, 4884.

(13) Busca, G. *Catal. Today* **1996**, *27*, 323.

(14) Botha, P. J.; Chiang, J. C. H.; Comins, J. D.; Mjwara, P. M.; Ngoepe, P. E. *J. Appl. Phys.* **1993**, *73*, 7268.

(15) Nomura, K. AIST-Kansai, open to public, 2002. http://unit.aist.go.jp/greenlife/ii/english/itscgallary-e.htm

(16) Fleischmann, M.; Hendra, P. J.; McQuillan, A. J.; Paul, R. L.; Reid, E. S. *J. Raman Spectrosc.* **1976**, *4*, 269.

(17) Jeanmaire, D. L.; Van Duyne, R. P. *J. Electroanal. Chem.* **1977**, *84*, 1.

(18) *Titanium and Zirconium in Organic Synthesis*; Marek, I., Ed.; Wiley-VCH, Inc.: Weinheim, Germany, 2002.

(19) Sukeshini, A. M.; Habibzadeh, B.; Becker, B. P.; Stoltz, C. A.; Eichhorn, B. W.; Jackson, G. S. *J. Electrochem. Soc.* **2006**, *153*, A705.

(20) Torres, D. I.; Paje, S. E.; Llopis, J.; Morell, G.; Katiyar, R. S. *J. Lumin.* **1997**, *72-74*, 724.

Chapter 3: Interfacial Resistivity of Yttria Stabilized Zirconia in Operating Solid Oxide Fuel Cells

1. Introduction

In the ongoing search for alternative sources of electricity production, fuel cells have attracted considerable attention due to their high fuel conversion efficiencies, their absence of moving parts and their relatively simple operational designs.[1-6] In particular, solid oxide fuel cells (SOFCs) represent attractive, stand-alone sources of power generation with operating efficiencies of up to 70% and relatively benign by-products.[5,6] In applications where heat is readily availble (in order to maintain operating temperatures in excess of 600 ˚C), SOFCs have proven to be economic solutions to situations requiring durable, efficient sources of direct current electricity.[7-9]

In the most general sense, SOFCs consist of a cathode, an anode and a solid oxide electrolyte. (Figure III.1) At the cathode molecular oxygen is catalytically reduced to form O^{2-}. These oxide anions diffuse through a solid oxide electrolyte to the SOFC anode where they react with incident fuel. The most common electrolyte found in SOFCs is yttria stabilized zirconia (YSZ), an electrically insulating metal oxide having a cubic lattice structure and oxygen vacancies (due to the substitution of Y_2O_3 for 2 x ZrO_2 at compositions of ~8-10 mole %).[4] The most common material used as an SOFC anode is a porous Ni/YSZ ceramic-metallic (or cermet) composite although alternative anodes have been prepared using metal oxides such as ceria

(CeO_2), samaria doped ceria ($Sm_{0.15}/Ce_{0.85}O_2$), perovskites, and even simple porous YSZ without an added metal.[10-16]

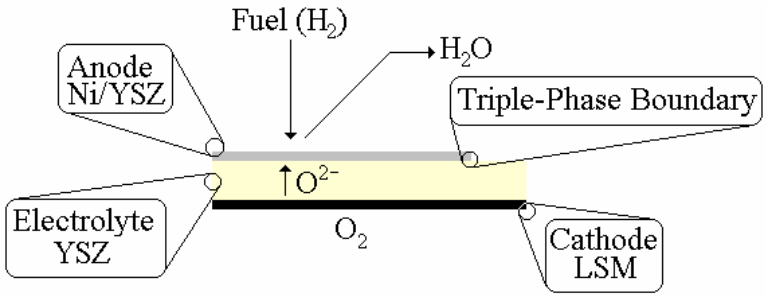

Figure III.1. General SOFC architecture.

Traditionally, research into SOFC operation has investigated questions about architecture, materials and transport in efforts to improve overall device efficiency.[4,5] More recently, researchers have begun to focus on the detailed chemical mechanisms by which SOFCs oxidize fuel to produce electricity.[17-19] Numerous challenges stand in the way of identifying directly the pathways responsible for converting hydrogen and carbon-based fuels to electricity and products such as CO_2 and H_2O. Quantifying specific reaction pathways leading to electrochemical fuel oxidation should lead to more efficient SOFC assemblies by allowing for rational choice of materials and design. One source of electrochemical activity that has not been considered explicitly in most models of fuel oxidation has been the YSZ electrolyte itself. This oversight is not surprising given the known chemical stability of YSZ as well as the material's electrically insulating properties. However, recent reports of a reduced surface phase of YSZ as well as SOFCs operating with a simple porous YSZ assembly for an anode raise questions about the role YSZ can play in SOFC electrochemistry.[20,21] Experiments described below use a variation of electrical impedance spectroscopy

(EIS) to characterize the electrical resistance across the surface of YSZ in different forms.

Underlying all models of electrochemical operation in SOFCs is the notion of a three-phase boundary (TPB), a term used to describe the junction of the solid state electrolyte, the conducting anode and the gas phase fuel mixture. This boundary represents the eletrochemically active region in the SOFC where the fuel and oxide ions meet and electrons resulting from fuel oxidation are carried into an external circuit.[22-24] Despite being an attractive tool used to rationalize the chemistry occuring in SOFCs, the TPB remains very poorly characterized. In principle, the TPB represents a one dimensional perimeter. In practice, the TPB should represent the regions of the Ni anode and YSZ electrolyte that participate in charge transfer and contribute electrons to the external circuit. In recent years, studies have shown that YSZ may indeed be more active in fuel cell processes than simply a medium for transporting oxide anions. One mechanism of fuel oxidation proposes that after molecular hydrogen dissociates on a Ni anode, atomic hydrogen may "spill-over" onto the electrolyte surface to react with O^{2-} some distance away from the formal anode/electrolyte boundary.[25] The lengthscale over which the spill-over mechanism operates has not been quantified, but the net effect of this phenomenon is to increase the effective triple-phase boundary from a one dimensional line to a two dimensional area. Further evidence that YSZ can participate in electrochemical oxidation and current collection comes from the aforementioned studies of SOFCs using only porous YSZ as the anode assembly and H_2 as the fuel.[20] Coupled with the discovery that reducing conditions can lead to reduced forms of Y and Zr that extend 5-10 Å

into bulk polycrystalline YSZ,[21] these results raise important questions about the electronically conducting and catalytic properties of the YSZ electrolyte in operating SOFCs.

The experiments described herein examine quantitatively the surface electrical conductivity of YSZ electrolytes in operating SOFCs having Ni/YSZ cermet anodes. Instead of using traditional 4-probe experiments to determine electrial conductivity, experiments employ a variation of EIS. All cells are operated with H_2 as the sole fuel source and EIS measurements are taken both after cell operation and after the cells have stood at open-circuit voltage (OCV) conditions. The conductivity of YSZ during SOFC operation is expressed as a resistivity. Under the conditions used in these studies, operating a cell at 0.6 V leads to a polycrystalline YSZ surface that is not DC conductive but has a surface resistivity of 4.70×10^{-4} Ω·cm, while the electrolyte surface of a cell that has been at OCV for more than 30 minutes exhibits DC conductivity and the surface resistivity has dropped to 3.31×10^{-4} Ω·cm. These results vary from sample to sample but the behavior is quite general and for a given sample, data reproduce quantitatively to within 10%. When extrapolated to the micron scale, the surface resistivity of the polished, polycrystalline electrolyte appears to be comparable to an external load. Surface resistivity depends sensitively on surface topography. Single crystal YSZ never exhibits DC conductivity under any conditions and porous, polycrystalline YSZ appears to be DC conductive, even in SOFCs operating at a cell potential of 0.6 V. Despite differences due to structure, both porous polycrystalline and single crystal YSZ show similar resistivities – on the same order of magnitude – to polished polycrystalline YSZ. The calculated

resistivities suggest that YSZ electrolytes can exhibit anode-like behavior for a distance of few microns away from the formal metal/electrolyte TPB.

2. Experimental

2A. Fuel Cell Construction

SOFCs used in this study had one of three different types of YSZ electrolyte surfaces. One electrolyte surface is simply a polished 1.5 mm thick, dense, polycrystalline, 8 mole % YSZ disk (ITN Energy Systems, Inc). The second electrolyte surface is a polished, 1.0 mm thick, single-crystal 8 mole % YSZ disk (MTI Corporation). The final electrolyte surface is a layer of porous YSZ deposited on the anode side of a polycrystalline disk. The deposited YSZ was prepared by tape casting a 60% YSZ powder – 40% glycerin mixture over a 12 mm diameter on the electrolyte and sintering at 1300 °C to create a porous YSZ layer approximately 0.1 mm thick.

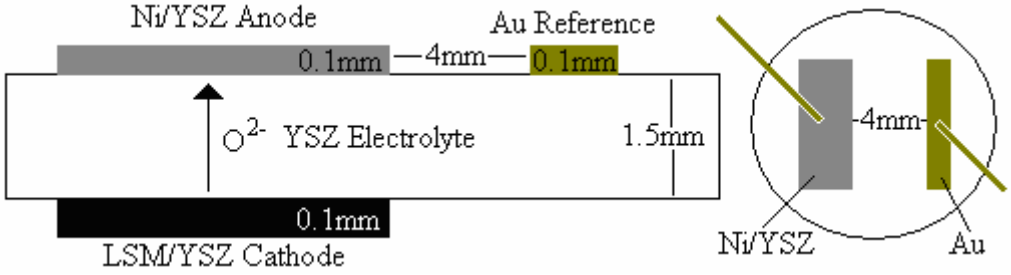

Figure III.2. Scheme showing a cross section (left) and top view (center) of the arrangement of electrodes in the SOFCs of this study. The scheme on the right is the cell architecture used in the supplemental experiments – the electrolyte surface is polished polycrystalline and is covered in porous YSZ in the shaded region.

All electrolytes were sandwiched between a porous LSM ($La_{0.85}Sr_{0.15}MnO_3$) cathode and a nickel/YSZ cermet anode. These membrane electrode assemblies (MEAs) consisted of a Ni/YSZ cermet anode placed on the electrolyte opposite the

cathode. A gold reference was placed on the anode side 4.0 mm or approximately three electrolyte thicknesses from the Ni/YSZ anode (Figure III.2). All electrodes were prepared by a tape casting method. The 10 mm x 2 mm rectangular cathodes were sintered in air by heating to 400 °C at a rate 0.3 °C/min. The temperature was held at 400 °C for one hour before the cathodes were heated to 1300 °C at 3 °C/min. After one hour at 1300 °C, the sample temperature was lowered to 25 °C at 3°C/min. Ni/YSZ cermet anodes were prepared by tape casting a commercially available, 50% post-reduction Ni content NiO/YSZ cermet (NexTech Materials Lot # 112-45) over a 10 mm x 2 mm area of the YSZ electrolyte. These anodes were then sintered at 1300 °C – the careful temperature cycle used for cathode sintering is not necessary for anode preparation. The gold electrode was placed 4.0 mm from the anode. The NiO/YSZ was reduced by an atmosphere of 5% H_2 – 95% Ar to Ni/YSZ while heating the fully assembled fuel cell to an operational temperature (800 °C) at 3 °C/min.

The MEAs were attached cathode-side-out to an alumina tube (22.2 mm OD, 15.9 mm ID) with a high temperature, zirconia-based ceramic paste. An alumina fuel-feed tube (4.8 mm OD, 3.2 mm ID) was centered in the larger tube and the entire assembly was placed in a temperature-controlled furnace. A second feeder tube was centered near the cathode to deliver air. Electronic mass flow controllers (Brooks 5850E) regulated the flow rates of the fuel stream. Data from the mass flow controllers were collected by a National Instruments SCXI data acquisition system. The cathode flow was regulated by a rotameter.

2B. Cell Operation and Electrochemical Measurements

EIS uses minimal AC currents to measure the ohmic resistance between a working and a counter electrode. Typically, when measuring the impedance of a SOFC the working electrode is the anode and the counter electrode is the cathode. Data contain information about total cell impedance, including electrolyte impedance to oxide flux, electrode contact resistance, electrode overpotential and other barriers to passing current (Figure III.3a).[18,26] In the experiments described below the Au reference on the anode side of the MEA was used as the counter electrode. This arrangement allows for the measurement of ohmic resistances between the Au and Ni/YSZ electrodes across the YSZ surface. The resulting impedance data contain information about the extent to which the electrolyte surface is electrically conducting. Contributing to the shape and magnitude of the impedance arcs are resistances due to general SOFC electrochemical processes such as fuel adsorption to the surface, repopulation of reduced sites by the oxide flux from the cathode, electrode contacts and local capacitances caused by grain boundaries and surface irregularities on the electrolyte. These resistances are all displayed on an EIS graph where the x-axis is the real part of the impedance (Z') and the y-axis is the imaginary part (-Z"). The data is tracked with a change in AC frequency and typically moves from left to right as the frequency decreases. The high frequency x-intercept is referred to as the bulk resistance (R_b) and is characteristic of the electrolyte impedance in typical measurements and of the electrode contact resistances in the surface measurements. The difference between the high and low frequency x-intercepts is the polarization resistance (R_p), which is a total cell resistance in typical

measurements and the surface resistance in the surface measurements. The very small AC currents used by EIS minimize the current-induced reduction of YSZ that can be observed in traditional four-probe measurements of material resistivity.[27-29]

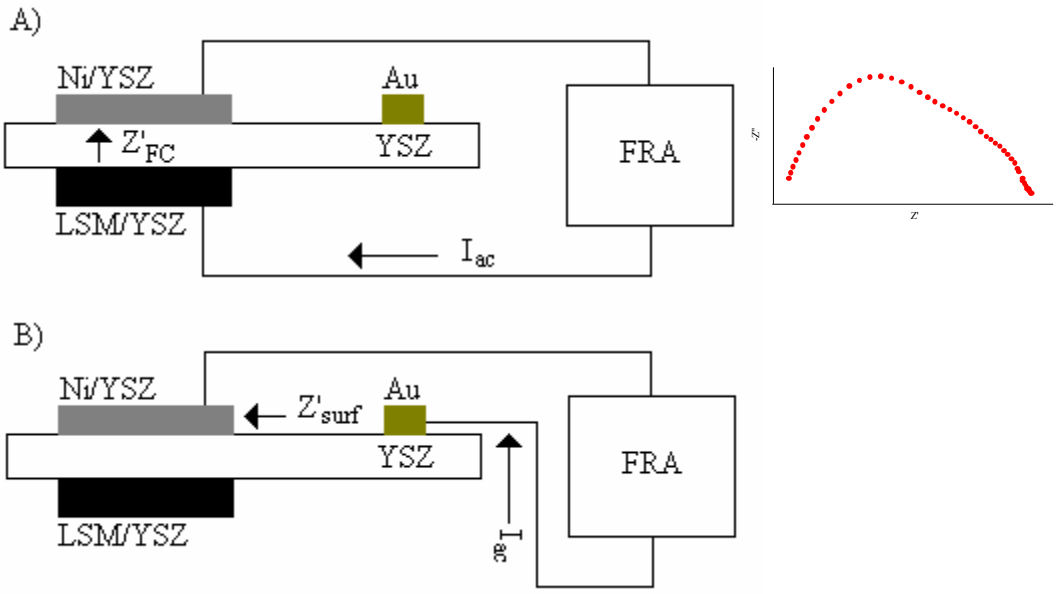

Figure III.3. SOFC wiring configurations used for A) total cell impedance and B) YSZ surface impedance.

H_2 was used as the fuel for these experiments and all cells operate at a temperature of 800 °C. A 70 sccm flow of H_2 on the anode side was balanced by a 35 sccm flow of air on the cathode side. All experiments used a fuel flow of 33% fuel, with a balance of Ar.

An Autolab PGSTAT30 (Eco Chemie) was used to monitor fuel cell performance. Power density measurements were taken to ensure that cells were operating properly. AC impedance spectra were taken using a two electrode configuration depicted schematically in Figure III.3. Two configurations were used to allow for both the cathode and Au reference to act as the counter electrode as described above. Impedance spectra were aquired under open circuit conditions over a frequency range from 100 kHz to 10 mHz.

Total cell EIS measurements were made at OCV (Figure III.3a). Cells were then operated at a cell potential of either 0.6 or 0.8 V for one hour prior to a surface EIS measurement (Figure III.3b). Additional surface EIS measurements were made 15 and 30 minutes after the cell was returned to OCV conditions in order to track the effects of atmospheric surface reduction. Previous experiments had determined that with the fuel flow rates used in these experiments, 30 minutes at OCV was sufficient to reduce the YSZ surface.

3. Results and Discussion

3A. Regular Cell Operation

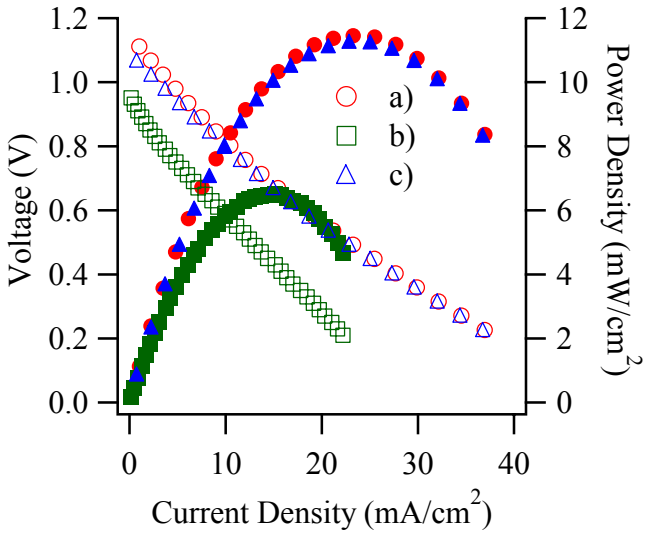

Figure III.4. Power density (closed marks) and V-I (open marks) plots typical of a) single crystal, b) polished, polycrystalline, and c) porous polycrystalline YSZ electrolyte SOFCs operated with hydrogen.

Once the SOFC assembly is at 800 °C the performance was monitored with V-I curves to ascertain system stability and reproducibility. Care was taken never to extend voltammetry experiments into regions of negative overpotential where anode degradation is known to occur. Representative electrochemical data from the SOFCs

used in these studies appear in Figure III.4. Due to the relatively thick electrolytes, these SOFCs generated only modest currents. Cell performance tended to stabilize in approximately 1 hour. After a period of stable operation, impedance measurements began. Figure III.5 shows representative, through-cell impedance data from the three fuel cells operated at OCV. The data corresponding to the cell with a polished, polycrystalline electrolyte surface display a polarization resistance (R_P) of 73.7 Ω that is largely electrolytic, but also contains contributions from cathode and anode related processes such as double layer capacitance and charge transfer resistance. These contributions have been isolated and identified in other reports.[18,26,30,31] After confirming the stable and well defined properties of a cell, surface impedance measurements were carried out to address specifically the question of whether or not YSZ can serve as a current collector in SOFCs thereby extending the three phase boundary and, if so, over what lengthscales.

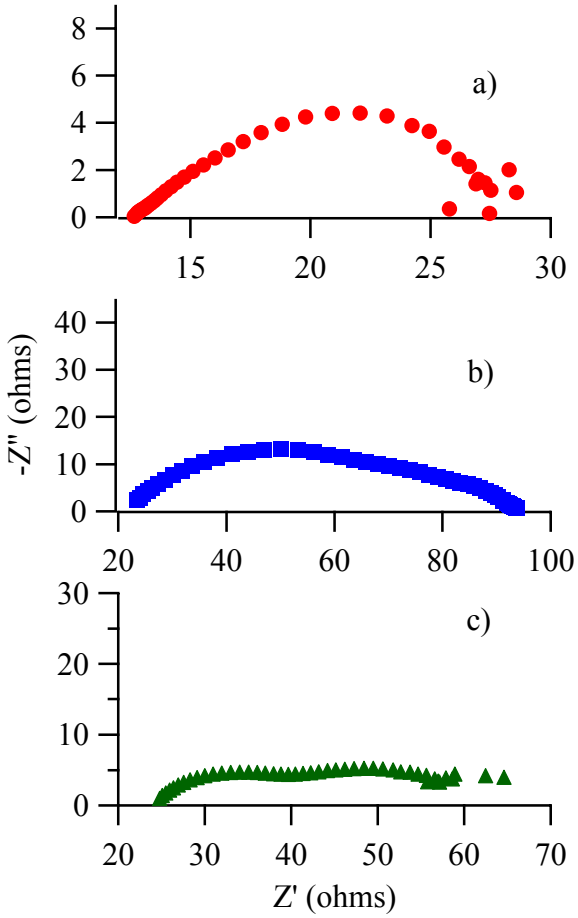

Figure III.5. Representative EIS plots typical of SOFCs with a) single crystal, b) polished polycrystalline, and c) porous polycrystalline YSZ electrolyte surfaces operated with hydrogen fuel. Note the different scales on the x and y axes.

3B. Surface Impedance Measurements

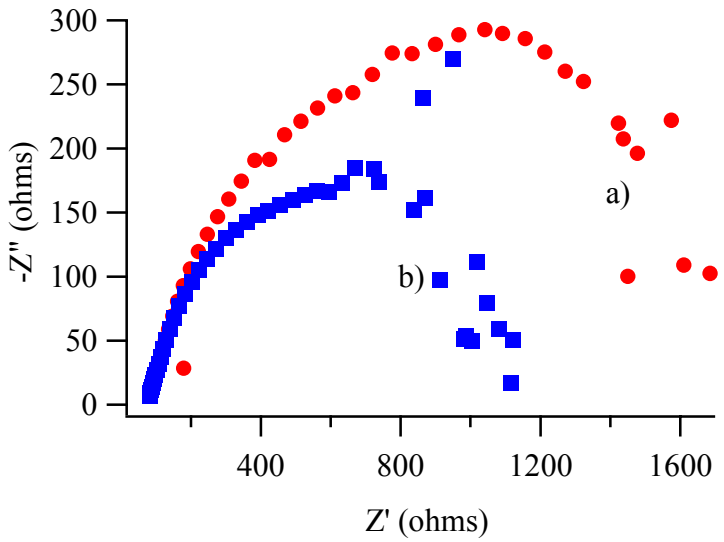

Figure III.6. Surface impedance plots of a cell with a polished, polycrystalline electrolyte operated at cell potentials of a) 0.6 V and b) 0.8 V.

Figure III.6 shows surface electrical impedance spectra for SOFCs containing polished polycrystalline electrolytes operated at cell potentials of 0.6 and 0.8 V across the cell. The impedance data from the SOFCs operated at 0.6 V result in a R_p value that is approximately twenty times higher than that of the through-cell polarization resistance. In addition to the increase in resistance, the data begin to oscillate and scatter as the measurements are carried out at lower and lower frequencies. Similar behavior is observed in the impedance data of cells operated at 0.8 V, although the data oscillate less and the arc appears more complete than when cells are operated at 0.6 V. Specific impedances of different cells vary quantitatively by as much as 850 Ω, but the data reproduce qualitatively for all cells. The quantitative differences likely result from differences inherent to the cells themselves including YSZ surface grain boundaries and electrode resistances that vary from cell to cell. Scattered data at low frequencies indicate a lack of DC conductivity between the counter and

working electrodes. Thus, the polycrystalline YSZ electrolyte of an operating SOFC does not appear to be DC conducting on macroscopic length scales.

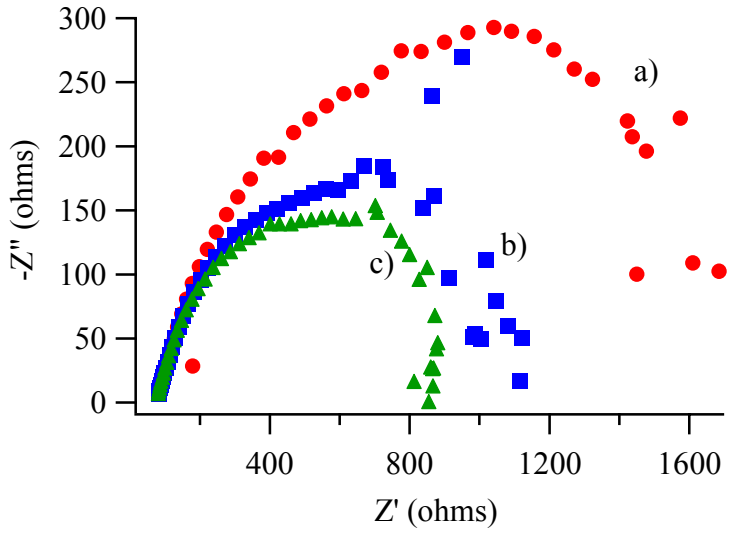

Figure III.7. Surface impedance plots of a cell with a polished, polycrystalline electrolyte operated at a cell potential of 0.6 V. EIS measurements were take at a) 0 min, b) 15 min, and c) 30 min after returning the cell to OCV operating conditions.

If a cell sits at OCV, the H_2 gas phase above the MEA will reduce the YSZ surface. Figure III.7 shows surface impedance plots of a cell that is operated at 0.6 V, followed by a return to OCV conditions. Changes in the impedance spectra are striking. After 15 minutes without an oxide flux the surface polarization resistance has dropped approximately 33% from ~1500 to ~1000 Ω. The low frequency data approach the x-axis with less scatter suggesting that the surface is acquiring a degree of DC conductivity that allows for 20 mA of current to pass between the electrodes across the surface when the arc is completed. The fact that the EIS data after 15 minutes at OCV still exhibit incomplete arcs indicate that the surface has not quite reached the point of DC conductivity. The data compare quite well to those of the same cell operated at 0.8 V without any time at OCV (Figure III.6b), suggesting a direct correlation between the amount of oxide flux during operation and the time

needed at OCV to re-reduce the YSZ surface with the incident fuel. According to the impedance data, the YSZ surface reduction is complete approximately 30 minutes after operation at 0.6 V has ceased. The impedance data for the reduced YSZ surface show considerably diminished scatter at low frequencies and, in fact, the impedance arc has a well-defined second intercept with the x-axis, completing the arc. The R_p value (~775 Ω) has dropped nearly 50% from the initial value of the surface operated at 0.6 V and the absence of scatter in the behavior of the data suggest that the polished polycrystalline electrolyte surface between the two electrodes has reduced sufficiently to become DC conductive.

Different YSZ surfaces exhibit quite different electrochemical behavior (Figure III.8) implying that a material's structure plays a critical role in controlling electrochemical properties. EIS data from SOFCs using a single crystal YSZ electrolyte never show DC conducting behavior, even after sitting at OCV and exposed to a reducing atmosphere for extended periods (8 hours). A porous polycrystalline surface shows the opposite behavior appearing to be DC conductive under all operating conditions.

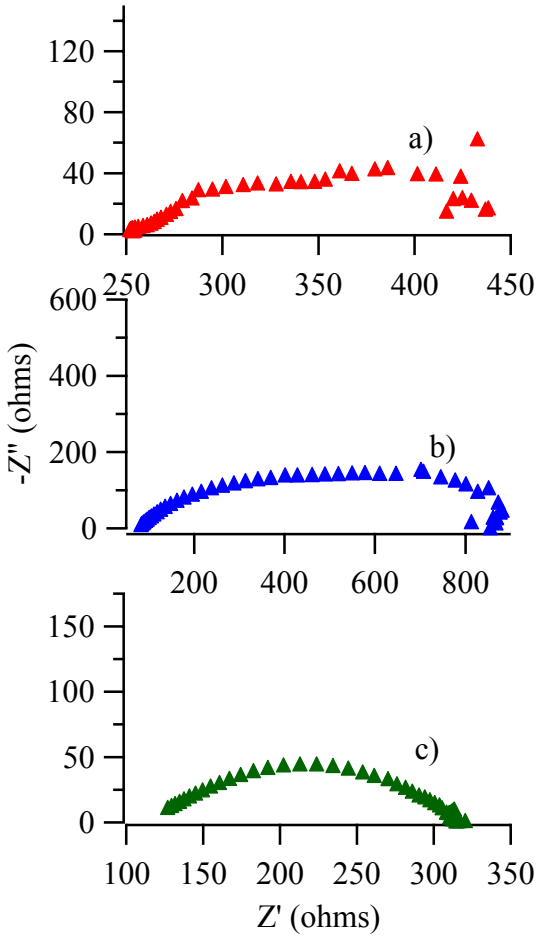

Figure III.8. Surface impedance plots for cells under OCV conditions for 30 minutes with a) single crystal, b) polished polycrystalline, and c) porous polycrystalline YSZ electrolyte surfaces. Note the different scales on the x and y axes.

Collectively these results imply the following for polycrystalline YSZ electrolytes used in SOFCs: under normal operating conditions the anode surface is sufficiently oxidized so that it remains electrically insulating. The insulating properties appear to be directly related to the potential at which the cell is operated as reflected differences in the data between SOFCs operated at 0.6 and 0.8 V. More specifically, the extent of chemical reduction on the YSZ surface appears to vary inversely with the amount of oxide diffusion through the YSZ membrane. When ion diffusion ceases (OCV conditions) the polycrystalline surface reduces and shows

strong evidence of electrical conductivity. The single crystal YSZ surface does not reduce under OCV conditions and thus is less likely to participate in charge transfer and deliver electrons to the anode as it. This retention of insulating properties may be due to the smooth surface that is devoid of structural features such as grain boundaries and pits that may promote and stabilize surface reduction. Regardless of the origin, the single crystal YSZ surface never shows any evidence of DC conductivity. The porous YSZ surface never oxidizes at 0.6 V suggesting that the reduced porous layer can conduct electrons but does not have the structural continuity to conduct oxide ions efficiently.

3C. Interpretation of Surface Conductivity in Terms of Resistances and Resistivities

The average resistances for SOFC electrolyte surfaces under the operating conditions described above are given in Table III.1. The values are derived from impedance plots such as those in Figures III.4 and III.5. In cases where the arcs are not complete a polynomial line fit is used to best complete the arc and determine a second, low frequency x-intercept. The large uncertainties associated with the data result from averaging data from multiple cells. Multiple measurements from a single cell carry uncertainties that are less than 10% of the average for that cell. The large range of resistances from one cell to another are attributed to inherent differences in the cell architecture including natural variances in YSZ surface grain boundaries, gold contacts, and contact resistances associated with the electrodes.

Table III.1: Surface resistances ($R_{p,surf}$) of YSZ in SOFCs (Ω, as measured)				
YSZ Surface	0.6 V	0.8 V	OCV(15min)*	OCV(30min)
Single crystal	190 ± 15	203 ± 10	231 ± 6	212 ± 26
Polycrystalline,polished	940 ± 402	698 ± 99	801 ± 217	662 ± 75
Polycrystalline,porous	194 ± 25	219 ± 6	200 ± 26	212 ± 22
* - *after 0.6 V operation only.*				

The conductivity of a material is commonly given in terms of a resistivity with units Ω·cm. The YSZ surface resistances of the cells are within the same order of magnitude as the electrode-reaction resistances of YSZ anodes on cells in previous work.[20] The surface resistances reported in Table III.1 can be converted to effective surface resistivities through the relationship $R = \rho(l/A)$ where R is the resistance equivalent to the R_p value of the impedance plots, ρ is surface resistivity, l is the distance separating the Ni/YSZ anode and the Au counter electrode, and A is the product of the anode length (1 cm) and the depth of the reduced surface (estimated to be ~2 nm based on previous previous studies of reduced YSZ). The resulting resistivities are listed in Table III.2. All three YSZ surfaces in a SOFC operating at 1.0 – 0.6 V overpotentials have resistivities on the order of 10^{-4} Ω·cm or approximately an order of magnitude lower than the resistivity of graphitic carbon – a material that has great impact on SOFC operation.[32] The average YSZ surface resistivity is comparable to that of nichrome.[33]

Table III.2: Surface resistivities of YSZ in SOFCs (Ω·cm)**				
YSZ Surface	0.6 V	0.8 V	OCV(15min)*	OCV(30min)
Single crystal	0.95 ± 0.08	1.02 ± 0.05	1.16 ± 0.03	1.06 ± 0.13
Polycrystalline,polished	4.70 ± 2.01	3.49 ± 0.49	4.00 ± 1.08	3.31 ± 0.38
Polycrystalline,porous	0.97 ± 0.12	1.09 ± 0.03	1.00 ± 0.13	1.06 ± 0.11
Gold				0.02
Nichrome				1.50
Carbon				35.0
Glass				$\sim 10^{14}$
* - *after 0.6 V operation only.*				
** - *values are* $x \cdot 10^{-4}$				

The data contained in Figures III.6 and III.7 show that the polished polycrystalline YSZ surface in a working SOFC becomes increasingly conductive when the device operates at lower overpotentials. Single crystal YSZ is not DC conductive and porous YSZ is DC conductive under all operating conditions. Nevertheless, the question remains of whether or not the surface is ever conductive enough to contribute to electrochemical fuel oxidation. In order for reduced YSZ to participate in SOFC operation, the YSZ would have to be able to deliver electrons to the circuit via a gold lead that is attached to the Ni/YSZ anode. Sustainable operation also requires oxide conduction to prevent deposition or irreversible chemical changes that accompany fuel reduction. The average resistivity value for the surface of the cell operating at 0.4 V overpotential is the highest of the surface values at $\sim 5 \times 10^{-4}$ Ω·cm, or ~5 Ω·μm. If 1 Ω is considered to be competitively resistive with the outside circuit then one can consider the electrolyte to be a contributor to electrochemical fuel oxidation processes at distances of approximately 1-10 μm from the anode even as oxide flux replaces the O^{2-} ions that are extracted to form products.

The presence of reduced, conducting YSZ on the anode-side surface of a fuel cell with a polycrystalline YSZ electrolyte implies that electrochemical oxidation in SOFCs will be more complicated than predicted by models based on a well defined, abrupt TPB. In addition to spill-over mechanisms previously proposed[25] the conductivity of reduced Zr and Y introduces new pathways for fuel oxidation and current production.

The calculated resistivities and inferred TPB distances are consistent with *ex-situ* examinations of the cells after operation. Figure III.9 shows the SEM image of the TPB area of a nickel anode deposited on a single crystal YSZ electrolyte in a SOFC that was operated with carbon-containing fuel.[18] The region of the electrolyte surface between the anode edge outlined with the dashed black line is spotted with carbon deposits not found on the rest of the electrolyte surface. This spotted region varies in width from 2 to 6 μm, consistent with the electrochemically active region of the electrolyte surface predicted by the impedance measurements. This image implies that even the surface of single crystal YSZ can participate in electrochemical fuel oxidation.

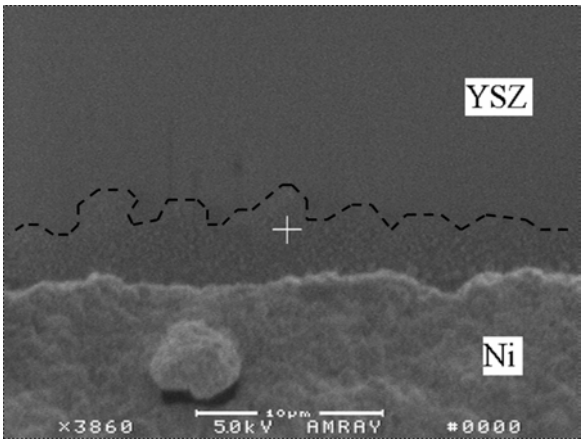

Figure III.9. SEM image of the TPB area of a SOFC with a Ni anode and single crystal YSZ electrolyte operated with CH_4 fuel.

An important point to note is that the mechanism of electrochemical fuel oxidation may well be different depending on where the oxidation takes place. Chemical properties of metal (Ni) and oxide surfaces are likely to be quite different and reactions occurring on the reduced YSZ surface will not necessarily contribute to the observed electrochemical behavior. For example, Fourier-transform infra-red spectra of fuel cell exhaust have revealed the presence of non-electrochemical reaction products.[34]

4. Conclusion

The electrochemical properties of YSZ surfaces have been investigated by EIS under various SOFC operating conditions. Data show that the surface of the polycrystalline electrolytes – previously not considered as a fuel oxidation site – can be reduced to the point where they become DC conductive with resistivities on the order of 10^{-4} Ω·cm. The extent of surface reduction depends sensitively on surface morphology and the operating overpotential of the SOFC. Rougher surfaces maintain better electrical conductivity up to the limit where porous YSZ remains DC conducting under all operating conditions. Polycrystalline surfaces exhibit reversible behavior; these surfaces are electrically insulating so long as the SOFC is operating at high enough overpotential so that the oxide ion flux keeps the surface oxidized. At lower overpotentials or under OCV conditions, however, the polycrystalline YSZ surface acquires a degree of DC electrical conductivity. In contrast, the single crystal

YSZ surface always shows electrical insulating characteristics even when subjected to strongly reducing conditions.

The surface is found to be competitively resistive with a fuel cell circuit within 1-10 microns of the Ni/YSZ anode. Results suggest that reactions that occur in this region likely contribute to the electrochemical fuel oxidation process and therefore to electrical production. Even the surfaces of single crystal YSZ also appear to contribute to electrochemical reactions even despite the electrically insulating properties measured in EIS experiments.

5. References

(1) Atkinson, A.; Barnett, S.; Gorte, R. J.; Irvine, J. T. S.; McEvoy, A. J.; Mogensen, M.; Singhal, S. C.; Vohs, J. *Nature Materials* **2004**, *3*, 17.

(2) Jacobson, M. Z.; Colella, W. G.; Golden, D. M. *Science* **2005**, *308*, 1901.

(3) Minh, N. Q. *Solid State Ionics* **2004**, *174*, 271.

(4) Ormerod, R. M. *Chem. Soc. Rev.* **2003**, *32*, 17.

(5) Song, C. S. *Catal. Today* **2002**, *77*, 17.

(6) Zhu, W. Z.; Deevi, S. C. *Mater. Sci. Eng.* **2003**, *A362*, 228.

(7) Alanne, K.; Saari, A.; Ugursal, V. I.; Good, J. *J. Power Sources* **2006**, *158*, 403.

(8) Calise, F.; Palombo, A.; Vanoli, L. *J. Power Sources* **2006**, *158*, 225.

(9) Fontell, E.; Phan, T.; Kivisaari, T.; Keranen, K. *J. Fuel Cell Sci. Technol.* **2006**, *3*, 242.

(10) Ishihara, T.; Yan, J. W.; Shinagawa, M.; Matsumoto, H. *Electrochim. Acta* **2006**, *52*, 1645.

(11) McIntosh, S.; Vohs, J. M.; Gorte, R. J. *J. Electrochem. Soc.* **2003**, *150*, A470.

(12) Nesaraj, A. S.; Kumar, M.; Raj, I. A.; Radhakrishna, I.; Pattabiraman, R. *J. Iranian Chem. Soc.* **2007**, *4*, 89.

(13) Rupp, J. L. M.; Drobek, T.; Rossi, A.; Gauckler, L. J. *Chem. Mater.* **2007**, *19*, 1134.

(14) Shao, Z. P.; Haile, S. M.; Ahn, J.; Ronney, P. D.; Zhan, Z. L.; Barnett, S. A. *Nature* **2005**, *435*, 795.

(15) Wang, C.; Xui, L. H.; Tang, W. H. *Rare Metal Mater. Eng.* **2006**, *35*, 501.

(16) Zhang, X.; Robertson, M.; Deces-Petit, C.; Qu, W.; Kesler, O.; Maric, R.; Ghosh, D. *J. Power Sources* **2007**, *164*, 668.

(17) McIntosh, S.; He, H.; Lee, S.-I.; Costa-Nunes, O.; Krishnan, V.; Vohs, J. M.; Gorte, R. J. *J. Electrochem. Soc.* **2004**, *151*, A604.

(18) Sukeshini, A. M.; Habibzadeh, B.; Becker, B. P.; Stoltz, C. A.; Eichhorn, B. W.; Jackson, G. S. *J. Electrochem. Soc.* **2006**, *153*, A705.

(19) Zhu, H.; Kee, R. J.; Janardhanan, V. M.; Deutschman, O.; Adams, J.; Eldridge, D.; Goodwin, D. G. "The Influence of Elementary Heterogeneous Reforming Chemistry within Solid-Oxide Fuel Cell Anodes"; Western States Section of the Combustion Institute, 2003, Los Angeles, CA.

(20) Hirabayashi, D.; Tomita, A.; Brito, M. E.; Hibino, T.; Harada, U.; Nagao, M.; Sano, M. *Solid State Ionics* **2004**, *168*, 23.

(21) Pomfret, M. B.; Stoltz, C.; Varughese, B.; Walker, R. A. *Anal. Chem.* **2005**, *77*, 1791.

(22) Bove, R.; Ubertini, S. *J. Power Sources* **2006**, *159*, 543.

(23) Fukunaga, H.; Ihara, M.; Sakaki, K.; Yamada, K. *Solid State Ionics* **1996**, *86-8*, 1179.

(24) Nam, J. H.; Jeon, D. H. *Electrochim. Acta* **2006**, *51*, 3446.

(25) Bieberle, A.; Gauckler, L. J. *Solid State Ionics* **2000**, *135*, 337.

(26) Bieberle, A.; Meier, L. P.; Gauckler, L. J. *J. Electrochem. Soc.* **2001**, *148*, A646.

(27) Levy, M.; Fouletier, J.; Kleitz, M. *J. Electrochem. Soc.* **1988**, *135*, 1584.

(28) Nagle, D.; PaiVerneker, V. R.; Petelin, A. N.; Groff, G. *Mater. Res. Bull.* **1989**, *24*, 619.

(29) Wright, D. A.; Thorp, J. S.; Aypar, A.; Buckley, H. P. *J. Mater. Sci.* **1973**, *8*, 876.

(30) Jiang, S. P.; Wang, W. *Electrochem. Solid State Lett.* **2005**, *8*, A115.

(31) Svensson, A. M.; Sunde, S.; Nisancioglu, K. *J. Electrochem. Soc.* **1997**, *144*, 2719.

(32) Pomfret, M. B.; Owrutsky, J. C.; Walker, R. A. *Anal. Chem.* **2007**, *79*, 2367.

(33) Physics Data; Institute of Science Technology, 2006. http://www.istonline.org.uk/Handbook/40.pdf

(34) Pomfret, M. B.; Demircan, O. S., A.M.; Walker, R. A. *Environ. Sci. Technol.* **2006**, *40*, 5574.

Chapter 4: Fuel Oxidation Efficiencies and Exhaust Composition in Solid Oxide Fuel Cells

1. Introduction

Fuel cells have attracted considerable attention in recent years as clean, efficient, durable means of alternative energy production. Solid oxide fuel cells (SOFCs) in particular stand out as attractive sources of electricity production given operating efficiencies of up to 70%, noise levels that are ~20 dB below those of conventional turbine engines and the absence of moving parts.[1] Ideally, SOFCs convert H_2 and/or carbon containing fuels into two products, H_2O and CO_2, that are relatively benign for the environment. However, the exhaust from fuel cells can contain complex mixtures of species resulting from reforming reactions, incomplete oxidation or simple unreacted fuel components passing through the electrochemical assembly.[2,3] One component of SOFC exhaust that merits particular attention is carbon monoxide (CO), a product of partial alkane oxidation on the way to formation of CO_2. CO has been identified by the EPA as a "criteria pollutant" and a potential public health hazard.[4] Thus, any potential source of CO must be factored into models that attempt to predict seasonal air quality in different regions around the country.

In the work presented below, Fourier Transform Infrared (FTIR) spectrometry is used to quantify the exhaust composition of SOFCs being operated with different fuel feeds and with different anode compositions. Results from this work can serve to guide users of SOFC technology who must choose operating conditions carefully to optimize fuel utilization and minimize the environmental consequences of incomplete

fuel oxidation and corresponding atmospheric pollution. Specifically, experiments examine the ability of nickel (Ni) and copper/ceria (Cu/CeO_2), two materials commonly used as SOFC anodes, to oxidize two dry hydrocarbon fuels, methane (CH_4) and butane (C_4H_{10}). By controlling the amount of fuel present in the fuel feed and by measuring quantitatively the amount of CO_2, CO and residual hydrocarbon species in the exhaust, we evaluate the ability of each anode material to oxidize fuel and the extent to which fuel is oxidized to its thermodynamic endpoint.

Data show CH_4 to be a less active but much cleaner fuel than C_4H_{10}. Efficiency here refers to the amount of fuel that is consumed relative to the amount of fuel present in the initial fuel feed. Fuel "cleanliness" refers to the amount of CO_2 (a product of complete oxidation) present in the exhaust relative to the amount of CO (a product of incomplete oxidation). Similarly, for a given fuel, a Ni anode produces more power but also more CO and graphite, whereas a Cu/CeO_2 anode is much less efficient in terms of overall power production, but the exhaust from SOFCs having Cu/CeO_2 anodes has a much higher CO_2/CO exhaust ratio. Taken together these findings have important consequences for determining the conditions under which SOFCs should be operated as well as important predictions pertaining to the environmental impact of improperly operated SOFCs that produce large amounts of atmospheric pollutants.

In the most general sense, SOFCs consist of a cathode, an anode and a solid oxide electrolyte.[5-12] At the cathode molecular oxygen is catalytically reduced to form O^{2-}. These oxide anions diffuse through a solid oxide electrolyte to the SOFC anode where they react with incident fuel. The most common electrolyte found in

SOFCs is yttria stabilized zirconia (YSZ), an electrically insulating metal oxide having a cubic lattice structure and oxygen vacancies (due to the substitution of Y_2O_3 for 2 x ZrO_2 at compositions of ~8-10 mole %). The most common material used as an SOFC anode is a porous Ni/YSZ cermet although alternative anodes have been prepared using metal oxides such as ceria (CeO_2), samaria doped ceria ($Sm_{0.15}Ce_{0.85}O_{1.925}$), and perovskites. [1,12-14]

Ni stands out as an attractive anode material given its ability to catalyze the decompositions of hydrocarbons. Under certain conditions, however, Ni can be too active and promote excessive carbon deposition, especially when higher molecular weight hydrocarbons are used as fuels.[3,15] These carbon deposits tend to be graphitic in character and their effects on SOFC performance can vary. In some instances, carbon deposits can compromise anode activity and signifcantly diminish the amount of current an SOFC can produce. However, under some circumstances, carbon deposition can "wire together" different pieces of a porous anode architecture leading to greater current collecting efficiencies and improved SOFC performance.[3,15,16]

Descriptions of how anode composition controls SOFC electrochemistry and influences exhaust product distributions remain largely speculative. Furthermore, most models of SOFC operation fail to account for the possibility that the material properties of the SOFC itself can change over time. That these changes affect electrochemical performance is unquestioned. A consequence of these changes is that the distribution of exhaust species will also change over time. Based on the fuel used and the products that appear in the exhaust, one can infer possible reaction mechanisms.[17-20] CO_2 and H_2O represent products of complete oxidation. Other

products, such as CO, CH_4 and C_2H_4, provide clues to overall cell efficiency and hint at bottlenecks in fuel oxidation processes. All of these species can be quantified in the SOFC exhaust with calibrated FTIR measurements. A simple elemental balance between the fuel flow and exhaust composition provides clues about the ability of various fuels to undergo complete oxidation, the SOFC materials that best catalyze fuel oxidation, and possible by-products not present in the exhaust. This work examines the exhaust of methane and butane fuel feeds in SOFCs operating at 800 °C with Ni/YSZ and Cu/CeO_2/YSZ anodes. Experiments examine the time evolution of products in the exhaust effluent as well as the overall SOFC fuel oxidation efficiency, defined here as the ratio of the partial pressures of a fully oxidized product, CO_2, and a partially oxidized product, CO.

2. Experimental

2A. Fuel Cell Fabrication

The SOFCs used in this study consist of electrolyte supported, three-layer architectures with a 1.5 mm thick, 8 mole % YSZ electrolyte (ITN Energy Systems, Inc.) sandwiched between a porous LSM ($La_{0.85}Sr_{0.15}MnO_3$) cathode and either a Cu/CeO_2/YSZ or Ni/YSZ porous anode. The 12 mm diameter cathodes were sintered in air by heating to 400 °C at a rate 0.3 °C/min, holding for one hour before ramping to 1300 °C at 3 °C/min and cooling after one hour to room temperature. Ni/YSZ cermet anodes were prepared by tape casting a commercially available, 50% post-reduction Ni content NiO/YSZ cermet (NexTech Materials Lot # 112-45) over a 12 mm diameter area on the YSZ electrolyte. These anodes were then sintered at

1300 °C – the careful temperature cycle used for cathode sintering is not necessary for anode preparation. The NiO/YSZ was reduced by an atmosphere of 5% H_2 – 95% Ar to Ni/YSZ while heating the fully-assembled fuel cell assembly to operational temperature (800 °C) at 3°C/min. Cu/CeO_2/YSZ anodes were prepared by first tape casting a 60% YSZ powder – 40% glycerin mixture over a 12 mm diameter on the electrolyte and sintering at 1300 °C to create a porous YSZ layer. The porous YSZ layer was impregnated with cerium (10 mole%) and copper (5 mole%) by a solution of nitrate precursors.[21] The resulting anode assembly was then sintered at 800 °C under a 5% H_2 – 95% Ar reducing atmosphere.

The membrane electrode assemblies (MEAs) were attached cathode-side-out to an alumina tube (22.2 mm OD, 15.9 mm ID) with a high temperature, zirconia-based ceramic paste. An alumina fuel-feed tube (4.8 mm OD, 3.2 mm ID) was centered in the larger tube and the entire assembly was placed in a temperature-controlled furnace. A second feeder tube was centered near the cathode to deliver air. The assembly is shown in Figure IV.1. Assembled SOFCs were heated to 800 °C at a rate of 1.5° per minute with a fuel flow of 5% H_2 (balance Ar). Once at 800 °C the experimental fuel flows were used. All cells were operated with H_2 fuel to calibrate performance cell-to-cell and to ensure proper function. Once cell performance stabilized the fuel flow was changed to the hydrocarbon fuel and exhaust measurements were made with the cells functioning at 0.6 V.

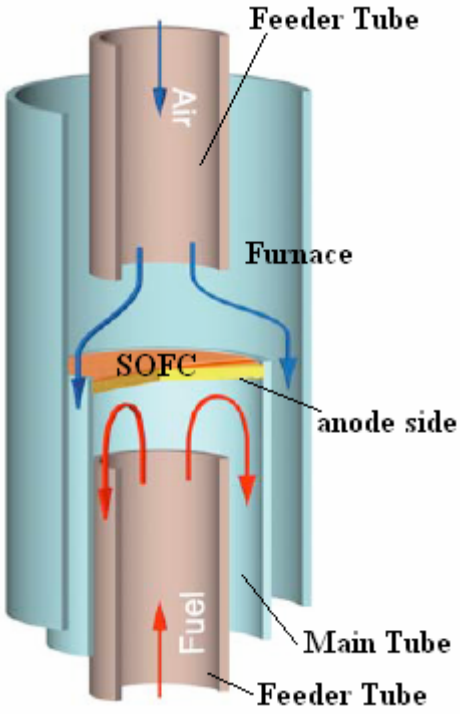

Figure IV.1. The SOFC operational assembly.

An Autolab PGSTAT30 (Eco Chemie) was used to monitor fuel cell performance. Periodic DC polarization measurements were taken to insure proper operation. Representative V-I traces and power curves for fuel cells operated with different fuel feeds appear in Figure IV.2.

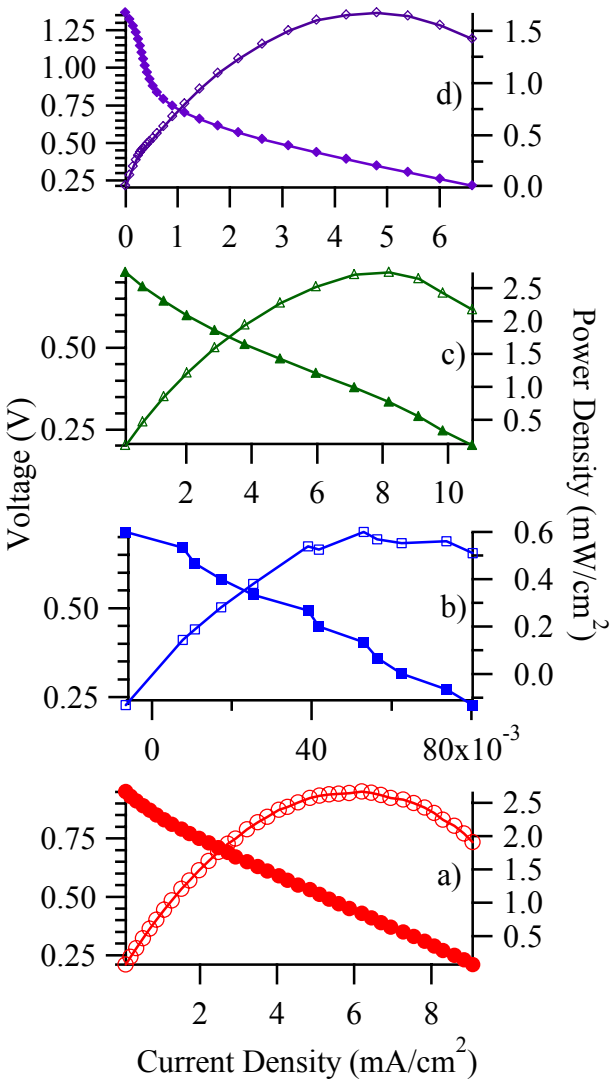

Figure IV.2. Typical voltage (solid marks) and power density (open marks) curves of a) H_2 (○), b) CH_4 (□), and c) C_4H_{10} (Δ) fuels in a SOFC with Ni/YSZ cermet anodes, and d) C_4H_{10} (◊) fuel in a SOFC with $Cu/CeO_2/YSZ$ a cermet anode. Note the different scales on the vertical and horizontal axes. The sharp rise in (d) at low current is due to a partial reduction of the CeO_2 to Ce_2O_3. All exhaust measurements were taken as cells were operated at a voltage of 0.6 V.

2B. Fuel Flows

Electronic mass flow controllers (Brooks 5850E) regulated the flow rates of the fuel stream. Data from the mass flow controllers were collected by a National Instruments SCXI data acquisition system. Three fuels – H_2, CH_4, and C_4H_{10} – were

used in experiments at an operating temperature of 800 °C. Experiments used stoichiometric fuel flow meaning that if all fuels were oxidized quantiatively the fuel cell would generate the same current regardless of fuel identity. For example, a fuel feed delivering 25% as much CH_4 (by mole fraction) as H_2 would lead to equivalent currents and power densities were both completely oxidized electrochemically. Experimental fuel flows are given in Table IV.1. A constant 50 sccm of air was flowed over the cathode and was regulated by a rotameter.

Table IV.1: Experimental SOFC fuel flow rates (sccm).

Fuel	Ar Flow	Fuel Flow	Fuel/Air
H_2	122.6	61.27	0.50
CH_4	30.64	15.32	2.00
C_4H_{10}	9.42	4.71	6.50

Experimentally, the fuels used in this study do not produce the same electrical output as evidenced in Figure IV.2. The first three traces show the VI data and power densities (scaled to anode area) of the three fuels used with a porous Ni/YSZ anode assembly. The SOFC operated with butane produces the highest currents followed closely by the H_2 operated SOFC. In contrast, currents from the SOFC operated with methane are ~1% of those values. These electrochemical results imply that the exhaust resulting from different fuel feeds will contain a mixture of species including CO_2 and H_2O as well as products of incomplete oxidation and unreacted fuel. The second series of experiments used the same fuel conditions over a $Cu/CeO_2/YSZ$ anode assembly to test the relative efficiency of different anode materials. (Figure IV.2d) This anode is less efficient but cleaner than Ni/YSZ – less fuel is

consumed but of the fuel that is oxidized, a higher fraction is converted to CO_2 and H_2O.

2C. Exhaust Collection and Infra-Red Spectroscopy Measurements

A custom-built, exhaust collection manifold was attached to the anode exhaust outlet. An IR gas cell with a volume of 35.0 cm^3 and NaCl crystal windows was evacuated before a background spectrum was acquired. The cell was then attached to the collection manifold. The valves on the IR cell were then opened and the exhaust of the fuel cell was passed through the collection system for 5 mins. After this time the IR cell valves were closed and a sample spectrum was acquired. All spectra were taken at room temperature (~25 °C) using a Thermo Nicolet Nexus 670 FTIR spectrometer. The gas collection manifold is illustrated schematically in Figure IV.3.

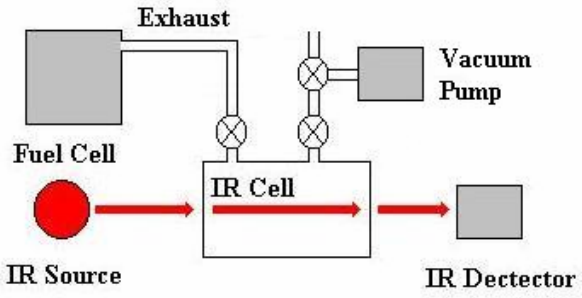

Figure IV.3. Scheme of infra-red sampling system used in this experiment.

2D. System Calibration

After identifying the main components of the anode-side exhaust with FTIR spectrometry, calibration data were collected for the fuels (butane and methane), their oxidation products (CO and CO_2), and likely gas-phase reforming products (C_2H_4), over a range of partial pressures from 0.01 to 0.33 atm (total pressure of 1 atm) using the same electronic mass flow controllers and software as in the actual exhaust

measurements. For each species, individual vibrational band intensities were integrated at different partial pressures and the resulting intensities were plotted versus partial pressure to give a calibration curve. In most cases the peak were separate from each other and if not one species dominated the region. This condition allowed for integration of the peak from the baseline on the low energy side of the peak to the baseline at the high energy side. Integrations included the rotational bands as well, in other words the P, Q and R branches were all included. A representative calibration curve for CO is shown in Figure IV.4.

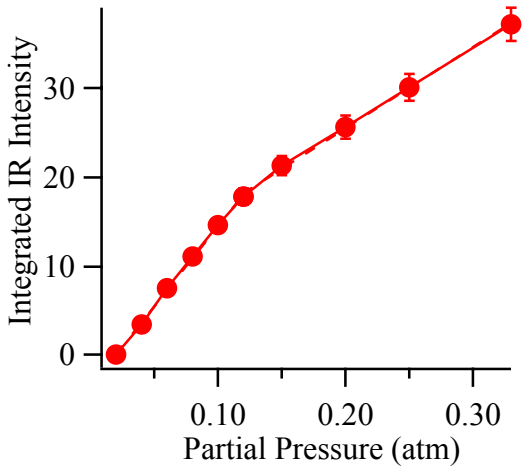

Figure IV.4. Calibration curve of carbon monoxide IR intensity.

At pressures above 0.12 atm the integrated intensities of vibrational features assigned to all identified exhaust species begin to deviate from expected Beer's law behavior. The calibration data, however, could be fit accurately to the sum of two different linear functions. With these calibrations, experimentally observed IR intensities of species in the SOFC exhaust were converted to partial pressures using the spectroscopic calibration data. While one may question the use of two linear fits

for data that should follow simple Beer's Law behavior, if a solitary function were used to fit the calibration data, low but measurable experimental intensities would give rise to negative partial pressures. We attribute the observed deviation in the calibration data to the mass flow controllers that cause small, systematic inaccuracies at flows that are less than 5% of the maximum flow for a particular controller. Multiple calibrations with the same fuel through the same controller reproduced to 5% for each data point. Fit parameters are listed in Table IV.2.

Table IV.2: Typical Conversions of Exhaust Component IR Intensities to Partial Pressures Through Calibration Line Fits (±5%)

Component Peak Position (cm^{-1})	Absorbance @ 0.12 atm PP	low b	low m	high b	high m
CH_4 3015	27.985	3.692	211.62	20.276	65.48
CH_4 1303	22.631	1.229	187.12	15.295	60.18
CO 2178	17.846	-3.364	178.88	7.385	90.54
CO_2 2359	n/a	-17.058	1591.4	n/a	n/a
C_4H_{10} 2965	n/a	-17.917	3625.5	n/a	n/a
C_4H_{10} 1466	17.596	-0.068	145.5	-2.218	172.37
C_4H_{10} 1391	4.697	-0.195	41.82	-0.056	41.24
C_2H_4 949	n/a	-0.346	209.43	n/a	n/a

3. Results and Discussion

3A. Diagnostic Spectral Intensities

Figure IV.5 shows exhaust spectra from stoichiometric quantities of all three fuels used with a Ni/YSZ anode, as well as the exhaust from a butane fuel feed to a $Cu/CeO_2/YSZ$ anode. All spectra exhibit well-resolved bands that can be readily assigned to stable, low molecular weight species. As expected, the H_2 exhaust spectrum shows only water stretching and bending bands. The CH_4 exhaust shows a

band centered at 2350 cm^{-1} assigned to the antisymmetric stretch of carbon dioxide. Additional features indicate the presence of unreacted fuel (CH_4 at 3015 and 1303 cm^{-1}) and a product of partial oxidation, carbon monoxide (2145 cm^{-1}). The same features appear in a more dramatic fashion in the spectra of exhaust from C_4H_{10} used in both Ni-based and Cu/CeO_2 fuel cells.

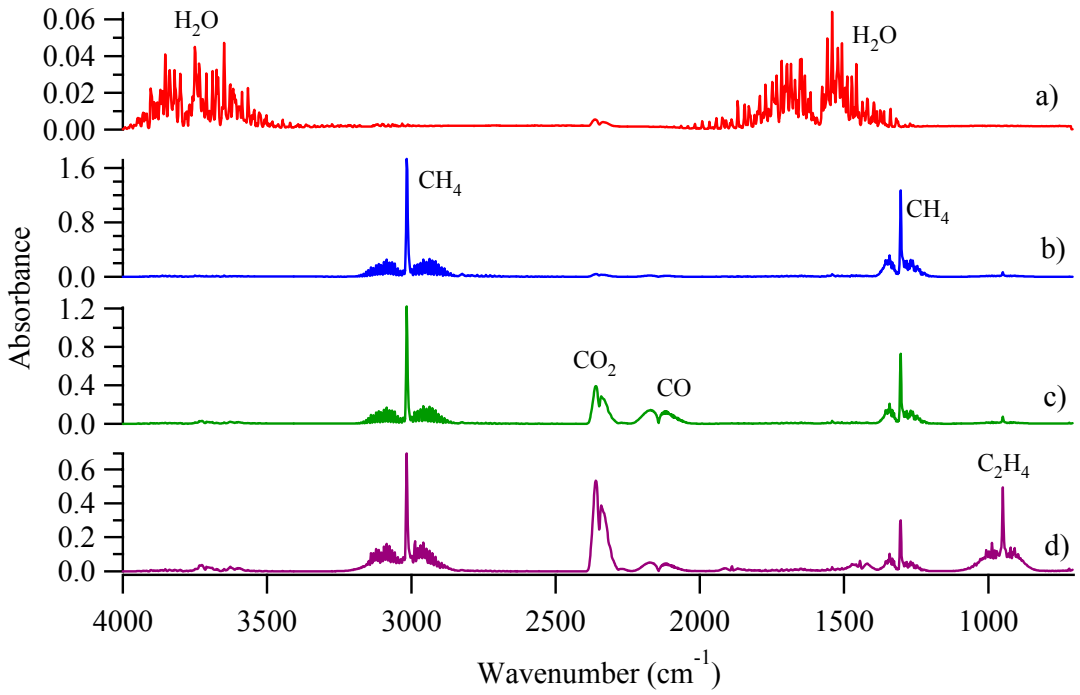

Figure IV.5. Typical SOFC emissions of a) H_2 fuel over Ni/YSZ anodes, b) CH_4 over Ni/YSZ, c) C_4H_{10} over Ni/YSZ, d) C_4H_{10} over Cu/CeO_2/YSZ. Note the different scale on the vertical axes.

As with methane, complete oxidation of butane would lead only to water and carbon dioxide peaks in IR exhaust spectra. However, many other species are present, most notably CH_4. There also appear to be other small hydrocarbons (≤ 4 carbons) based on the asymmetry of the methane band. One product is ethylene, based on the large intensity near 950 cm^{-1} in the exhaust spectrum of the Cu/CeO_2

based SOFC operated with butane. Butane itself is not distinguishable in the exhaust, a result that is consistent with previous studies of butane pyrolysis measured in flow tubes at similar temperatures (>700˚ C), but with shorter residence times.[2] This same study reported that butane pyrolysis in the inlet results in a fuel flow having C_2H_4 (39.8%) and CH_4 (36.3%) as prinicipal components.[2] If this high-temperature fuel pyrolysis occurs in the fuel feed tube prior to exposure to the anode, little or no butane can participate in electrochemical oxidation reactions, and the exhaust is likely to contain a complex mixture of saturated and unsaturated hydrocarbons. From the CH_4 data presented in Figure IV.6, we know that a large fraction of the CH_4 produced by pyrolysis will pass through the SOFC unreacted. Other hydrocarbons are likely to be more reactive and either oxidize or form carbon deposits.

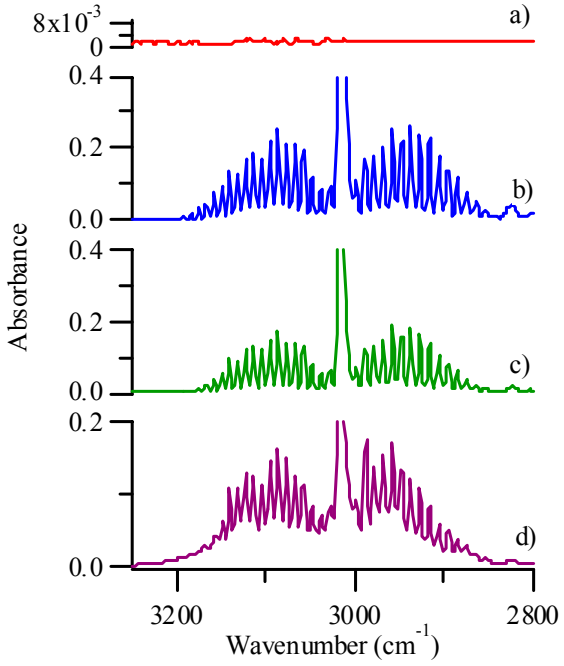

Figure IV.6. Methane absorbance peaks of a) H_2 fuel over a Ni/YSZ anode, b) CH_4 over Ni/YSZ, c) C_4H_{10} over Ni/YSZ, and d) C_4H_{10} over $Cu/CeO_2/YSZ$. Note the absence of asymmetry and unresolved lines in (c), implying the hydrocarbon exhaust from a Ni/YSZ SOFC operated with butane is predominantly CH_4. The large unresolved intensity in (d) reflects a more complicated distribution of products.

Figure IV.7 displays the 2000-2500 cm^{-1} region in the IR spectra of the exhaust of $C_4H_{10(g)}/Cu/CeO_2$ and on $C_4H_{10(g)}/Ni/YSZ$, and $CH_{4(g)}/Ni/YSZ$. Several observations stand out. First, Ni/YSZ anodes lead to lesser amounts CO and CO_2 from methane compared to butane. This observation is consistent with the relatively poor electrochemical performance of SOFCs operated with a CH_4 fuel feed. If complete oxidation occured, the same amount of carbon containing products would appear in the exhaust of both fuels given the stoichiometric conditions of the initial fuel flows. However, with butane as a fuel, CO_2 and CO features are much stronger than those resulting from a methane feed meaning that the products of butane pyrolysis oxidize much more easily than CH_4 itself.

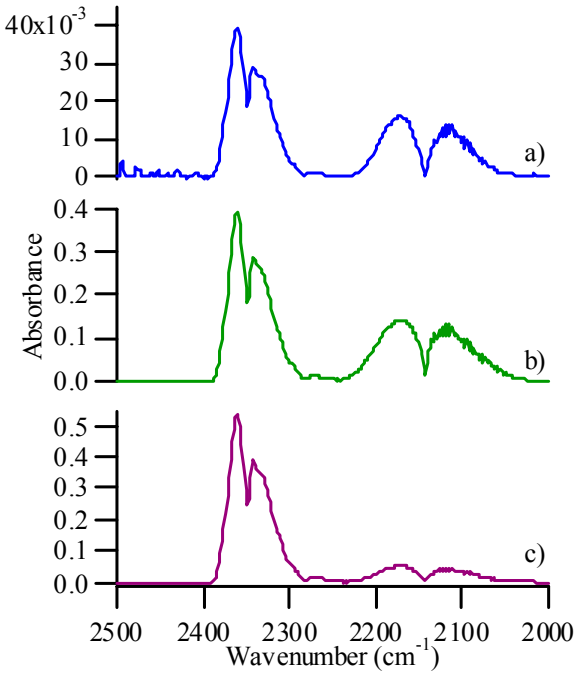

Figure IV.7. CO and CO_2 absorbance intensities in SOFC exhaust of a) CH_4 fuel over Ni/YSZ anodes, b) C_4H_{10} over Ni/YSZ, and c) C_4H_{10} over Cu/CeO_2/YSZ. Note the different scales on the vertical axes.

3B. Quantitative Partial Pressures

For all of the experiments presented in this work, the distinguishable, carbon-containing species in the exhaust are CH_4, C_2H_4, CO and CO_2 – an "unreacted" hydrocarbon, an unsaturated hydrocarbon, a partially oxidized product and a fully oxidized product, respectively. The relative amounts of these species in SOFC exhaust can serve as a diagnostic of device performance and can provide clues about possible oxidation mechanisms. Converting observed spectral intensities to partial pressures can accomplish these goals quantitatively. Partial pressures of species present in the exhaust have been determined from integrated IR absorbance data. Partial pressure data was used to monitor fuel oxidation efficiency over time.

(Figure IV.8) With CH_4 as the fuel for a Ni/YSZ anode, both electrochemical behavior and exhaust composition stabilizes within 10 minutes of operation, although SOFC performance is quite poor. (Figure IV.4b) The exhaust composition from this SOFC/fuel combination leads to the production of only 0.011 atm CO_2 and a partial pressure of 0.023 atm CO. More than 50% of the fuel sent into the SOFC – 0.174 atm – passes through the assembly unchanged. An important point to note is that approximately 33% of the methane can not be accounted for by mass balance. Raman spectroscopy measurements provide conclusive evidence that some carbon from a CH_4 fuel feed remains in the SOFC chamber adsorbed to the Ni surface. This mechanism as well as loss of carbon to the walls of the rig and the electrolyte surface are likely sinks for missing carbon in the exhaust measurements.

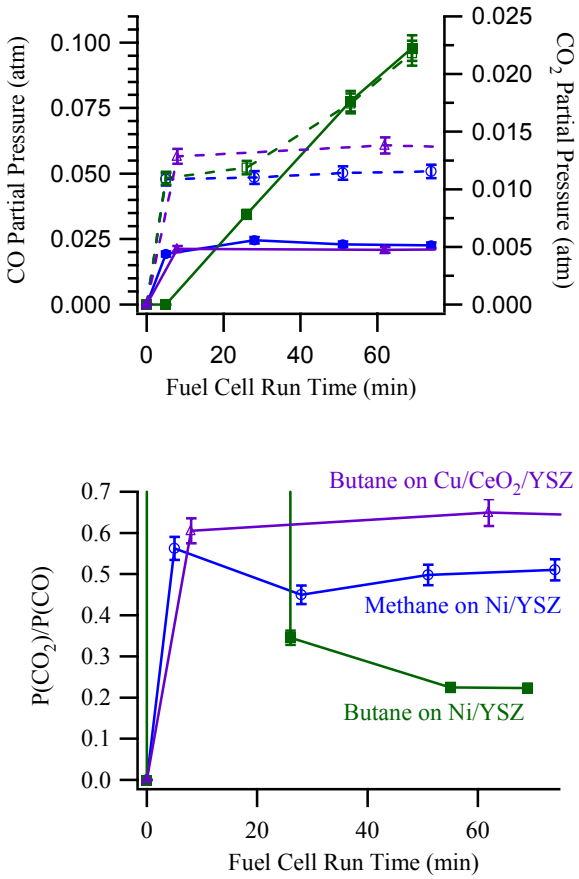

Figure IV.8. SOFC exhaust output stabilization over time in terms of CO partial pressure (solid marks and lines) and CO_2 partial pressure (open marks, dashed lines) for CH_4 fuel over Ni/YSZ anodes (○), C_4H_{10} over Ni/YSZ (□), and C_4H_{10} over $Cu/CeO_2/YSZ$ (Δ), and in terms of $P(CO_2)/P(CO)$ ratio for CH_4 fuel over Ni/YSZ anodes (○), C_4H_{10} over Ni/YSZ (■), and C_4H_{10} over $Cu/CeO_2/YSZ$ (Δ).

Cells using butane as a fuel over a Ni/YSZ anode do not demonstrate the same exhaust stabilization as the methane cells. Almost one hour is required for partial pressures in the exhaust to become stable. After the exhaust composition has stabilized, a butane feed (P_{init} = 0.333) produces twice as much carbon dioxide (0.022 atm) and four times more carbon monoxide (0.098 atm) as does the CH_4 feed. In terms of overall fuel oxidation efficiency, butane leads to more products being formed both from partial and complete oxidation. In addition, the exhaust from butane contains a large amount (0.083 atm) of CH_4 and measurable amounts

(0.005 atm) of ethylene (C_2H_4). The time-dependent data in Figure IV.8 show that butane oxidation becomes more favorable over time although the electrochemical data remain stable after the first 10 minutes of operation implying that changes in exhaust composition reflect changes in non-electrochemical processes occurring in the SOFC. An important observation from the $C_4H_{10(g)}$/Ni/YSZ exhaust data is that at very early times, little CO is produced. This product begins to appear in significant quantities ~10-20 after electrochemical performance has stabilized, suggesting non-electrochemical side reactions bear a large responsibility for the observed increase in measured "product" concentrations. The origin of this additional channel for hydrocarbon reaction is unclear, but the only source of oxygen is from the cathode/electrolyte meaning that any side reactions have to occur on the electrolyte surface away from the conducting anode.

Replacing the Ni anode with Cu/CeO_2 significantly impacts the exhaust from SOFCs operating with a butane feed. Exhaust composition stabilizes on a time scale similar to what is seen in the methane-Ni/YSZ cells. Less CO and CO_2 are produced compared to the amount of products produced by the Ni/YSZ anode operating with an equivalent fuel feed, but Cu/CeO_2 SOFCs operate with much higher relative efficiencies given the higher P_{CO_2}/P_{CO} ratio. A second important observation is that the exhaust spectrum from the Cu/CeO_2 anode/C_4H_{10} fuel combination shows more intensity in the IR spectrum near 950 cm^{-1}. This band is assigned to the out-of-plane bending motion of C_2H_4[23] and its appearance implies that whatever mechanism consumes ethylene in the Ni/YSZ SOFC is not present in the Cu/CeO_2 SOFC. The integrated intensity of the C_2H_4 band centered at 950 cm^{-1} corresponds to a partial

pressure of 0.094 atm, almost twenty times the partial pressure of C_2H_4 in the exhaust of the butane operated Ni/YSZ SOFC. Figure IV.9 shows the ethylene peak observed in each fuel/anode case.

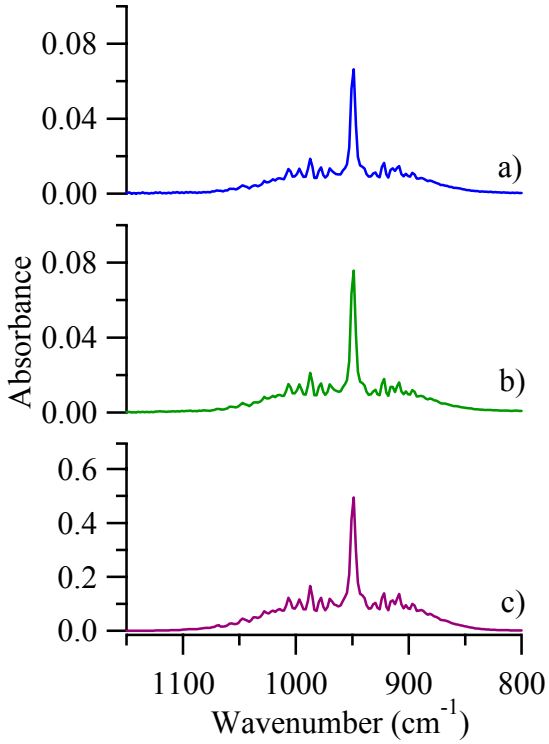

Figure IV.9. Ethylene absorbance peaks of a) CH_4 over Ni/YSZ, b) C_4H_{10} over Ni/YSZ, and c) C_4H_{10} over Cu/CeO_2/YSZ. (Note the difference in the scale of the y-axis between the Ni/YSZ cells and the Cu/CeO2/YSZ cell.) The relative intensities of this peak in the different cells imply that whatever mechanism consumes ethylene in the Ni/YSZ SOFC is not present in the Cu/CeO_2 SOFC.

To summarize the performance characteristics of the different fuel/anode combinations, all cells produce more CO than CO_2. The fuel/anode combination with the highest fuel conversion efficiency (as evidenced by the largest P_{CO_2}/P_{CO} ratio) is the butane/Cu/CeO_2 combination, yielding a value of 0.628 ± 0.016. The methane/Ni/YSZ cell has the second highest ratio at 0.486 ± 0.023. Despite producing the greatest amounts of CO and CO_2, exhaust from the butane/Ni

combination gives a ratio of 0.224 ± 0.001, a value that is almost three times less than that of the Cu/CeO_2 anode assembly. Figure IV.8 tracks the P_{CO_2}/P_{CO} ratio over time. The butane/Ni system shows no measurable amount of CO during early stages of operation (0-15 min) leading to a divergent P_{CO_2}/P_{CO} ratio. The P_{CO_2}/P_{CO} ratio requires almost one hour to stabilize, suggesting that the anode/electrolyte composition is changing, presumably due to carbon deposition and anode degradation as evidenced by a drop in cell performance to an OCV of ~0.80 V.

3C. Proposed Oxidation Mechanisms

In all cell types, the three main exhaust components were CH_4, CO, and CO_2 with considerable amounts of C_2H_4 also present in the Cu/CeO_2 SOFC exhaust. The quantitative amount of these carbon containing species in the exhaust effluent are reported in Table IV.3. After summing the partial pressures, one can see immediately that the total amount of the identified exhaust gases does not account for all of the fuel flowing into the cell.

Table IV.3: Partial Pressures of Exhaust Components (atm) ±5%

Fuel-Anode	Fuel In	Methane	CO	CO_2	C_2H_4	%C in exhaust
CH_4-Ni/YSZ	0.333	0.179	0.023	0.011	0.003	65.8
C_4H_{10}-Ni/YSZ	0.333	0.083	0.098	0.022	0.005	16.0
C_4H_{10}-Cu/CeO_2/YSZ	0.333	0.11	0.021	0.013	0.094	24.9

The Ni/YSZ SOFC operated with CH_4 produced exhaust that accounted for 66% of the total carbon content in the fuel feed. This "balance" represents the best agreement between fuel in and exhaust out for the three systems studied. Post-operation inspection showed no visual carbon deposition on either the MEA or on the

walls of the inlet and exhaust feeds, although Raman measurements do show the presence of carbon. Based on the components in the CH_4 exhaust, the simplest description of chemistry occuring in the CH_4 operated SOFC is that very little chemistry happens at all. More than 50% of the fuel passes through the SOFC unchanged. Of the CH_4 that is consumed, CO – the product of a single oxidation event – is present in a 2:1 ratio over the product of complete oxidation (CO_2).

The Ni/YSZ SOFC operated with C_4H_{10} also yields an exhaust spectrum with a clean methane product signature, a rather unexpected result given that one expects significant amounts of other hydrocarbon species that result from gas phase pyrolysis.[22] Surprisingly small is the amount of C_2H_4, which suggests that ethylene reacts efficiently on the Ni anode to produce graphitic deposits. The larger partial pressures of CO and CO_2 as well as the absence of hydrocarbons – other than methane – are consistent with improved electrochemical performance and suggest that higher molecular weight hydrocarbons are more easily oxidized by the Ni/YSZ anode. Despite the enhanced presence of oxidized products, larger amounts of carbon are unaccounted for with butane as a fuel compared to methane. In fact, 84% of the total incident carbon fails to emerge in the SOFC exhaust. The most obvious source of carbon loss is the significant build up of carbon deposits on the anode surface and the walls of the SOFC itself. Carbon build up is severe and readily visible to the naked eye, demonstrating the largest problem of using Ni/YSZ anodes with higher molecular weight hydrocarbon fuels.

The Cu/CeO_2 SOFCs operating with C_4H_{10} also show considerable carbon loss, with 75% of the incident carbon content missing from the measured exhaust.

Again carbon deposition is the likely culprit. After hours of operation, the Cu/CeO_2 anode shows only slight discoloration suggesting that this system is not plagued by the same electrocatalytic deposition of graphitic carbon endemic to the Ni/YSZ anode. However, the walls of the SOFC become coated with a brown-gray, hydrophobic film after only 1-2 hours of operation. Mass spectrometry, NMR, and chromatography show these deposits to contain a variety of high molecular weight hydrocarbons including naphthalene, anthracene, pyrene and fluorene.[3,15] Consequently, we attribute much of the carbon loss observed with the Cu/CeO_2 SOFC to gas phase chemistry and condensation of products resulting from butane pyrolysis. These factors combined with large amounts of C_2H_4 present in the exhaust show the Cu/CeO_2 anode to be relatively inert in terms of its ability to promote chemistry (electrochemical or otherwise). However, the chemistry that does occur on the Cu/CeO_2 surface is more likely to proceed all the way to its thermodynamic endpoint than on Ni/YSZ or graphitic surfaces as evidenced by the relatively large P_{CO_2}/P_{CO} ratio of 0.619.

4. Conclusion

IR absorbance data from SOFCs operating with CH_4 and C_4H_{10} show that CH_4 is, in fact, a very poor fuel that leads to minimal electrochemical oxidation (as determined from electrochemical measurements and the presence of oxidation products in the exhaust). More than half of the carbon content in the exhaust of Ni/YSZ SOFCs operated with CH_4 is nothing more than unreacted fuel. Previous work has shown that at standard SOFC operating temperatures (>700˚C) butane undergoes extensive pyrolysis with CH_4 and C_2H_4 appearing as the majority

products.[2] Our results support these findings as they identify both CH_4 and C_2H_4 as gas phase products in SOFC exhaust following transit through the anode chamber. As an anode material, Ni catalyzes "coke" formation. Interestingly, we see appreciable amounts of CH_4 in the exhaust from a $C_4H_{10(g)}$/Ni/YSZ system but virtually no C_2H_4, implying that ethylene is necessary to grow the observed graphitic deposits. Carbon deposition does not appear to inhibit fuel oxidation, however, as these systems produce ~4-5 times more CO and twice as much CO_2 than similar SOFCs operated with CH_4. SOFCs operating with Cu/CeO_2 anodes and a butane fuel feed show both CH_4 and C_2H_4 in their exhaust and the SOFC assembly following operation is correspondingly free from the extensive carbon deposition observed with the Ni/YSZ anodes. Consequently, Cu/CeO_2 can be considered less active in its ability to catalyze carbon deposition. This anode material is a poorer electrocatalyst as evidenced by smaller amounts of CO and CO_2 in the exhaust, but the fuel that does oxidize on the Cu/CeO_2 anode does so more efficiently given the larger P_{CO_2}/P_{CO} ratio.

These findings should prove valuable to evolving models of chemical oxidation in SOFCs and to assessing the impact of using SOFCs on environmental quality and human health. Results clearly motivate the need for SOFC systems to employ fuel recovery technologies to reclaim the considerable amounts of unreacted fuel (and fuel byproducts) present in SOFC exhaust. Furthermore, data presented above suggest that alternative anode materials (such as Cu/CeO_2) may have distinct advantages over commonly used systems (Ni/YSZ) in terms of their ability to more completely convert incident fuels to their thermodynamic endpoint.

5. References

(1) Song, C. S. *Catal. Today* **2002**, *77*, 17.

(2) Sheng, C. Y.; Dean, A. M. *J. Phys. Chem. A* **2004**, *108*, 3772.

(3) McIntosh, S.; Vohs, J. M.; Gorte, R. J. *J. Electrochem. Soc.* **2003**, *150*, A470.

(4) Air and Radiation - Basic Information - Six Common Air Pollutants - Carbon Monoxide: Chief, 2005. http://www.epa.gov/air/urbanair/co/chf1.html.

(5) Ormerod, R. M. *Chem. Soc. Rev.* **2003**, *32*, 17.

(6) Brown, M.; Primdahl, S.; Mogensen, M. *J. Electrochem. Soc.* **2000**, *147*, 475.

(7) Srikar, V. T.; Turner, K. T.; Ie, T. Y. A.; Spearing, S. M. *J. Power Sources* **2004**, *125*, 62.

(8) Weber, A.; Ivers-Tiffee, E. *J. Power Sources* **2004**, *127*, 273.

(9) Mizusaki, J.; Tagawa, H.; Saito, T.; Kamitani, K.; Yamamura, T.; Hirano, K.; Ehara, S.; Takagi, T.; Hikita, T.; Ippommatsu, M.; Nakagawa, S.; Hashimoto, K. *J. Electrochem. Soc.* **1994**, *141*, 2129.

(10) Mogensen, M.; Skaarup, S. *Solid State Ionics* **1996**, *86-8*, 1151.

(11) Primdahl, S.; Mogensen, M. *J. Electrochem. Soc.* **1997**, *144*, 3409.

(12) Hirabayashi, D.; Tomita, A.; Brito, M. E.; Hibino, T.; Harada, U.; Nagao, M.; Sano, M. *Solid State Ionics* **2004**, *168*, 23.

(13) Gorte, R. J.; Kim, H.; Vohs, J. M. *J. Power Sources* **2002**, *106*, 10.

(14) Shao, Z. P.; Haile, S. M.; Ahn, J.; Ronney, P. D.; Zhan, Z. L.; Barnett, S. A. *Nature* **2005**, *435*, 795.

(15) Demircan, O.; Sukeshini, M.; Pomfret, M. B.; Jackson, G. S.; Walker, R. A.; Eichhorn, B. W. "Formation of Carbon Deposits from Hydrocarbon Fuels in SOFC: Towards a Mechanistic Understanding"; 205th Meeting of The Electrochemical Society, 2004, San Antonio, TX.

(16) Minh, N. Q. *Solid State Ionics* **2004**, *174*, 271.

(17) Bron, M.; Holze, R. *Fresenius J. Anal. Chem.* **1998**, *361*, 694.

(18) Busca, G. *Catalysis Today* **1996**, *27*, 323.

(19) Park, S.; Wasileski, S. A.; Weaver, M. J. *Electrochim. Acta* **2002**, *47*, 3611.

(20) Wu, Q.-H.; Abernathy, H.; Liu, M. "FTIR Studies and Kinetic Modeling of Oxygen Reduction on Cathode Materials for SOFCs"; 204th Meeting of the Electrochemical Society, 2003.

(21) Putna, E. S.; Stubenrauch, J.; Vohs, J. M.; Gorte, R. J. *Langmuir* **1995**, *11*, 4832.

(22) Mathieu, D. M.; Dean, A. M.; Grenda, J. M.; Green, J. W. H. *J. Phys. Chem. A* **2003**, *107*, 8552.

Chapter 5: High-Temperature Raman Spectroscopy of Solid Oxide Fuel Cell Materials and *In-Situ* Studies of Fuel Oxidation in Solid Oxide Fuel Cells

1. Introduction

Solid oxide fuel cells (SOFCs) convert fuel – typically H_2, CO, CH_4 or higher molecular weight hydrocarbons – to water, carbon dioxide, electricity and heat.[1-3] Given their ability to produce electricity efficiently, cleanly and with high power densities, SOFCs have become an integral element of a growing, world-wide energy infrastructure.[4-6] Despite the popularity of these devices, little is known about mechanisms responsible for fuel oxidation and power production. The distinct absence of molecularly specific information about how carbon containing fuels are electrochemically oxidized hampers efforts to develop quantitative, predictive models of SOFC operation. Experiments described below present the first direct, *in-situ* measurements of relevant chemical species formed on SOFC anodes operating with both butane and CO fuel feeds. Raman spectroscopy is used to acquire vibrational spectra from SOFC cermet anodes at 715 °C during operation. The appearance and disappearance of different carbonaceous species on SOFC anodes as well as the cell potential-dependent presence of these intermediates point to different mechanisms of fuel utilization that depend on fuel and operating conditions.

One perplexing question plaguing SOFC development involves how carbon deposits grow on SOFC anodes and how these deposits impact overall device performance.[2,7-10] Butane (C_4H_{10}) often serves as a model for higher molecular

weight hydrocarbon fuels, and McIntosh, et. al. reported enhanced power production from porous ceria anodes when butane was used as a fuel.[8,9] To explain this observation, the authors proposed a mechanism whereby conducting carbon deposits improved the connectivity of the porous anode, thus increasing the effective anode surface area and improving current collection. This observed behavior challenged the conventional wisdom that carbon deposition in SOFC assemblies leads to diminished performance.[7,8] *Ex-situ* analysis identified polyaromatic hydrocarbons as the conducting carbon on the Cu/CeO_2 anodes.[8,9]

Understanding the role of carbon in SOFC chemistry has proven difficult, in part, due to a lack of non-invasive techniques capable of identifying intermediates *in-situ* under typical operating conditions.[11-13] Electrochemical methods such as voltammetry and electrochemical impedance spectroscopy are effective for quantifying cell performance,[14,15] but these measurements lack the chemical specificity necessary to identify the underlying chemistry. Existing electrochemical experiments and models of fuel oxidation can only speculate about the relative importance of different oxidation pathways and relative fuel conversion efficiencies,[14,16,17] because identification of chemical intermediates has proven difficult. In contrast, optical spectroscopy *is* capable of identifying molecular structures present on SOFC electrode surfaces. Siebert and coworkers used Raman spectroscopy to study oxygen adsorption on Pt electrodes at temperatures up to 500 ˚C, a process directly relevant to cathode operation in SOFCs.[13] Similarly, Liu and coworkers examined the infrared emission from SOFC cathodes at 550 ˚C with an FTIR spectrometer and, based on spectral changes that depended upon applied

potential, assigned vibrational features to surface oxide anions.[18] These pioneering studies demonstrated the power and ability of noninvasive, optical methods to identify species present in SOFCs. However, both reports described experiments carried out at temperatures lower than is common for standard SOFC operation, and both reports focused on cathodic processes.

Chemistry at anodes is much more complex than the oxygen reduction that happens at cathodes, especially if the fuel consists of a heterogeneous mixture of H_2, CO, and/or saturated and unsaturated hydrocarbons. Oxidation of the anode electrocatalysts, such as nickel, is known to compromise SOFC performance while carbon deposition can either promote or inhibit electrochemical processes, depending on the details of the specific SOFC system.[9,19,20]

To examine the electrochemical oxidation of fuels in a working SOFC, we constructed an optically accessible, electrochemical rig that operates at a temperature of 715 ˚C. (Figure V.1) Experiments presented below use Raman spectroscopy to characterize material properties and processes occurring on anode materials at temperatures typical of working SOFCs. Specifically, spectra show that the F_{2g} phonon band of YSZ can serve as internal measure of temperature and electrolyte structure due to a linear shift in band frequency and lattice expansion with increasing temperature. Furthermore, strong Raman signals from NiO[21] and nanocrystalline graphite (NCG)[22,23] allow for the study of kinetics of cell processes on the order of minutes. These processes include the oxidation of Ni and the reduction of NiO, as well as the formation of NCG as a result of butane flow and the degradation of the NCG as the surface is exposed to a weakly oxidizing atmosphere.

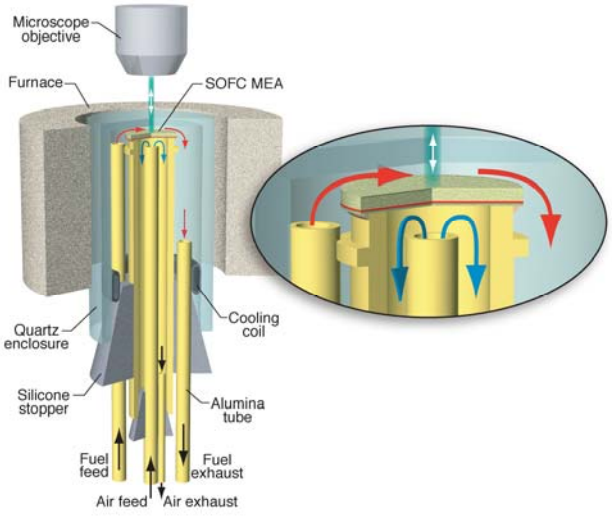

Figure V.1. This schematic shows the optically accessible, electrochemical rig that allows for acquiring Raman data from SOFCs operated at 715 ˚C.

The *in-situ* Raman technique is then used to examine relevant chemical species formed on SOFC anodes operating with both butane and CO fuel feeds. Raman spectroscopy is used to acquire vibrational spectra from SOFC cermet anodes at 715 °C during operation. The appearance and disappearance of different carbonaceous species on SOFC anodes as well as the cell potential-dependent presence of these intermediates point to different mechanisms of fuel utilization that depend on fuel and operating conditions.

2. Experimental

2A. Sample Preparation

The SOFC materials used in this study consisted of a polycrystalline, 8 mole % yttria YSZ electrolyte (Tosoh), pressed to a thickness of 0.8 mm and sintered at 1500 °C, and a Ni/YSZ porous layer (NexTech Materials Lot # 112-45). The Ni/YSZ cermet patch was prepared by a tape casting method followed by

sintering at 1000 °C, resulting in a layer with a thickness of ~100 μm covering approximately one half of a side of the 25 mm YSZ disk. The cermet consisted of 50% Ni and 50% YSZ (by weight) post-reduction. The disks were attached Ni/YSZ-side-out to an alumina tube (25 mm O.D.) with a high temperature, zirconia-based ceramic paste. Alumina tubes of smaller diameters (6 mm O.D.) were used for the gas feeds. A quartz tube with an optically transparent window on one end was used to encase the rig, creating a closed chamber while allowing for optical probes. A split-tube furnace is then fitted around the upper two-thirds of the quartz tube. The bottom of the tube is fitted with a water-cooled coil. This allows for an active cell or a substrate at the top to be heated while the bottom of the tube is cool enough to be stopped with a silicone plug.

The SOFCs used in this study consisted of a 0.8 mm thick polycrystalline, 8 mole% yttria YSZ electrolyte (Tosoh), sintered at 1500 °C, a Ni/YSZ (50% Ni and 50% YSZ by weight) porous anode (NexTech Materials Lot # 112-45) and a LSM/YSZ (50% $La_{0.85}Sr_{0.15}MnO_3$ and 50% YSZ by weight) cathode. The electrodes were prepared by tape casting and sintering at 1300 °C, resulting in thicknesses of ~20 μm covering 12.5 mm circles centered on the 25 mm YSZ disk. The disks were attached anode-side-out to an alumina tube assembly with zirconia paste as shown in Figure V.1. A quartz tube closed on one end encased the rig. A split-tube furnace was fitted around the upper two-thirds of the assembly while the bottom was water-cooled. A picture of the fully-assembled rig and furnace appears in Figure V.2.

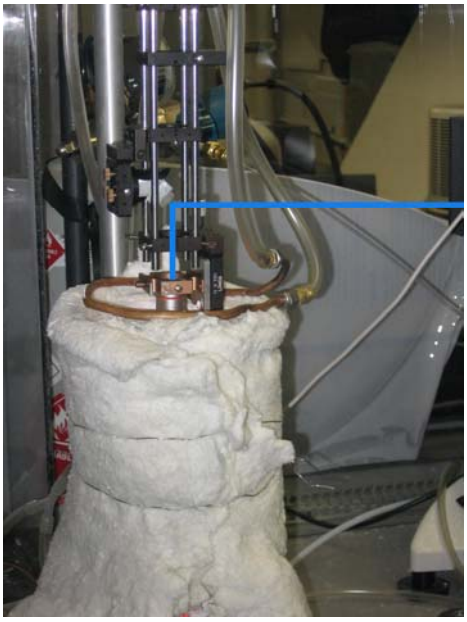

Figure V.2. A picture of the exterior of the experimental rig. The rig itself is contained inside a tube furnace (Thermcraft). A blue line is drawn to show the path of the 488 nm excitation. Signal collection occurs as 180° reflectance of the incident beam.

2B. Gas Flows

In the optical SOFC assembly, the graphite formed by hydrocarbon fuels can block the optical window. Therefore, the C_4H_{10} flow must be regulated such that the window can be kept clean while a constant cell polarization is applied. For the material studies a constant 150 sccm of Ar was flowed over both sides of the disk. The Ni/YSZ side of the disk was subjected to various atmospheres including 1:2 H_2:Ar, 1:19 H_2O:Ar, 1:2 air:Ar, and 1:1:5 H_2:C_4H_{10}:Ar.

The gas flows for the *in-situ* Raman experiments of operation SOFCs are as follows. To sustain constant polarization an Ar/H_2 feed is flowed (150 sccm Ar, 30 sccm H_2). 5 cc of C_4H_{10} is then "burst" on top of the base flow over the course of 10 s. This technique for fuel introduction allows for the investigation of the effects of cell exposure to butane on a well resolved time scale. CO flows are constant

(150 sccm Ar, 90 sccm CO). 90 sccm of Air was flowed over the cathode. Rotameters (Omega) regulated flow rates.

2C. Electrochemical Operation and Data Collection

Cell polarization and electrochemical measurements were controlled by Gamry Instruments PCI4 Potentiostat/Galvanostat/ZRA. Cells were polarized at three cell voltages: open circuit voltage (OCV or 1.06 for both fuels), 0.76 V, and 0.46 V. All V-I plots are corrected for electrolyte IR losses.

2D. Raman Measurements

Raman spectra were obtained with a Renishaw In-Via Raman microscope using a custom-built optical accessory. The custom accessory duplicates the function of the microscope while allowing for a 50x objective to be lowered into the furnace. Samples were irradiated with the 488 nm output of an Ar ion laser (25 mW) focused to a 1 μm-diameter spot. For C_4H_{10}, Raman spectra of the anode surface were acquired immediately before exposure to C_4H_{10} (30 co-added 1 s scans), every minute for the first 4 minutes after exposure (30 co-added 1 s scans for each), and a longer, more well resolved scan was taken over the 7^{th}-14^{th} minutes after exposure (200 co-added 1 s scans). For CO, Raman spectra (200 co-added 1 s scans) of the anode surface were acquired at time = 0 min, 10 min, and 20 min. Reported Raman frequencies are accurate and reproducible to within 1 cm^{-1}.

2E. XRD Measurements

XRD data were acquired using a Bruker C2 Discover X-ray Powder Diffractometer with a HiStar area detector and CuK_α radiation. Six frames were

collected with the area detector and merged to give 2θ scan ranges from 4° to 90°. Unit cell indexing and refinements were carried out using the MDI Jade software package.

2F. XPS Measurements

The X-ray photoelectron spectroscopy measurements were carried out using a Kratos Axis 165 spectrometer at a vacuum of $4x10^{-10}$ Torr with monochromatic Al Kα radiation. The X-ray power used for the measurements was 144 W. A wide scan survey, as well as various element specific regions (Y 3d, Zr 3d, O 1s and C 1s), were measured. All measurements were carried out in hybrid lens mode using both electrostatic and magnetic lenses with a step size of 0.1 eV and sweep time of 60 s. Survey spectra were only 2 scans with a pass energy of 160 eV. All individual region spectra were recorded in the FAT analyzer mode with pass energy of 80 eV, and an average of 10 scans. The charge neutralizer was on during the measurements to compensate for surface charging and binding energies were calibrated with respect to C 1s at 284.6 eV. Data processing is done using Vision processing software. After subtraction of a linear background, all spectra are fitted using 60% Gaussian / 40% Lorentzian peaks, taking the minimum number of peaks consistent with the best fit.

3. Results and Discussion

3A. Material Studies

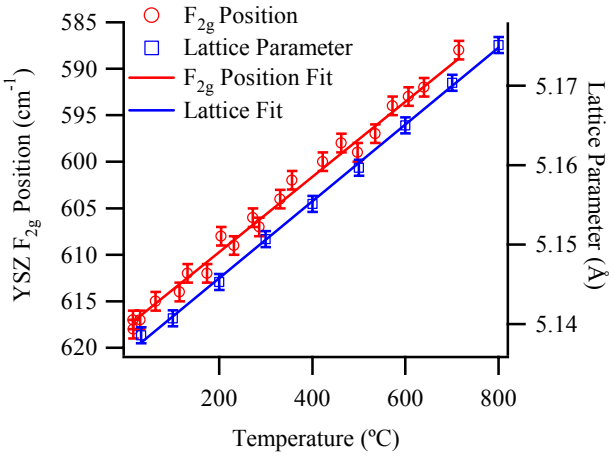

Figure V.3. The temperature dependence of the YSZ F_{2g} Raman band maximum frequency and of its lattice constant as measured by XRD.

The most common electrolyte used in SOFCs is cubic YSZ. The cubic crystal structure of this material has a very distinct X-ray diffraction (XRD) pattern as well as a Raman active phonon band at 618 cm^{-1} at 20 °C.[24] This lattice vibration is assigned to the triply degenerate, anti-symmetric motion of adjacent oxide ions in the lattice and is assigned a symmetry label of F_{2g}. As a function of temperature, the frequency of the F_{2g} mode shifts more than 30 cm^{-1} between room temperature and 715˚C. Data from XRD experiments show the lattice parameter of YSZ to have a similar dependence on temperature. The correlation between shifts in the lattice parameter and F_{2g} peak position are readily apparent in Figure V.3, and the spectroscopic results compare favorably with the limited amount of previously published data.[25,26] Raman spectra and XRD patterns of YSZ at 20 °C and 700 °C are shown in Figure V.4.

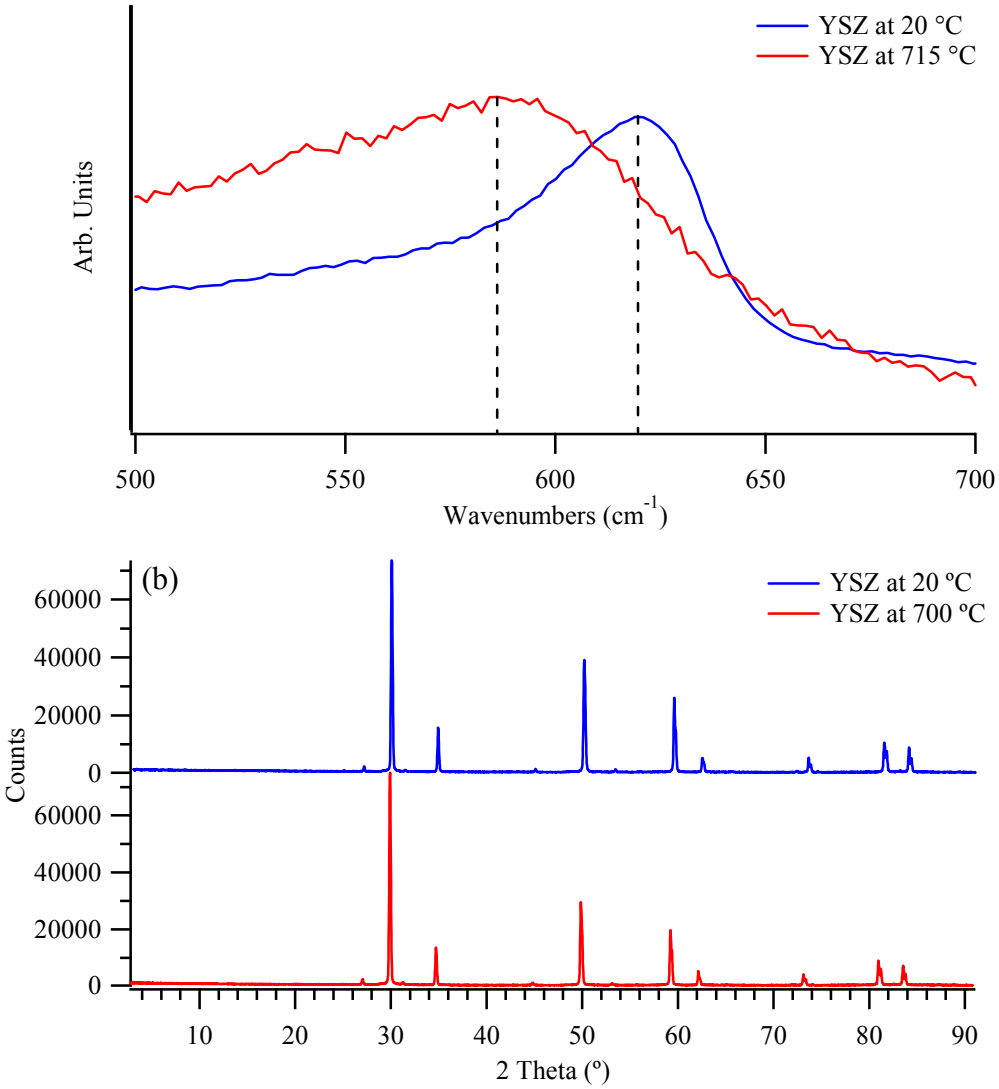

Figure V.4. (a) Raman spectra of the prominent F_{2g} peak of cubic YSZ at 20 ºC and 715 ºC. (b) XRD patterns of the cubic YSZ lattice at 20 ºC and 715 ºC.

This correlation between a spectroscopic signature and both temperature and structural properties means that SOFC assemblies having exposed YSZ surfaces can be monitored *in-situ* and noninvasively with Raman spectroscopy. The pronounced ~30 cm^{-1} shift of the F_{2g} band over a 700 °C window provides a convenient internal diagnostic that allows for a determination of the absolute temperature to within 25 °C. (Independent temperature measurements were made with thermocouples.) Unlike

earlier work that compared signal intensities from the Stokes and anti-Stokes spectra of ZnO[27] and graphite[28] to measure sample temperatures, using the temperature dependent, Raman signature of YSZ as an internal thermometer is both direct and simple. This *in-situ* diagnostic should prove useful in identifying electrochemically active and inactive sites across a SOFC.

Temperature dependent shifts in the Raman bands of other materials that figure prominently in SOFC chemistry have also measured. Upon heating from room temperature to 715 °C, the dominant phonon band of NiO (2LO) shifts lower by ~40 cm^{-1} from 1095 cm^{-1} to 1055 cm^{-1}. A Raman feature of graphite – assigned as the G peak (E_{2g}, 1580 cm^{-1})[22] – shifts lower ~20 cm^{-1} over the same temperature window. The latter is evident in Raman spectra of highly ordered pyrolytic graphite (HOPG, shown in Figure V.5) collected at 20 °C and higher temperatures (550-715 °C). Again, spectra show band shifts to lower frequency with increasing temperature in a manner consistent with previous studies.[28]

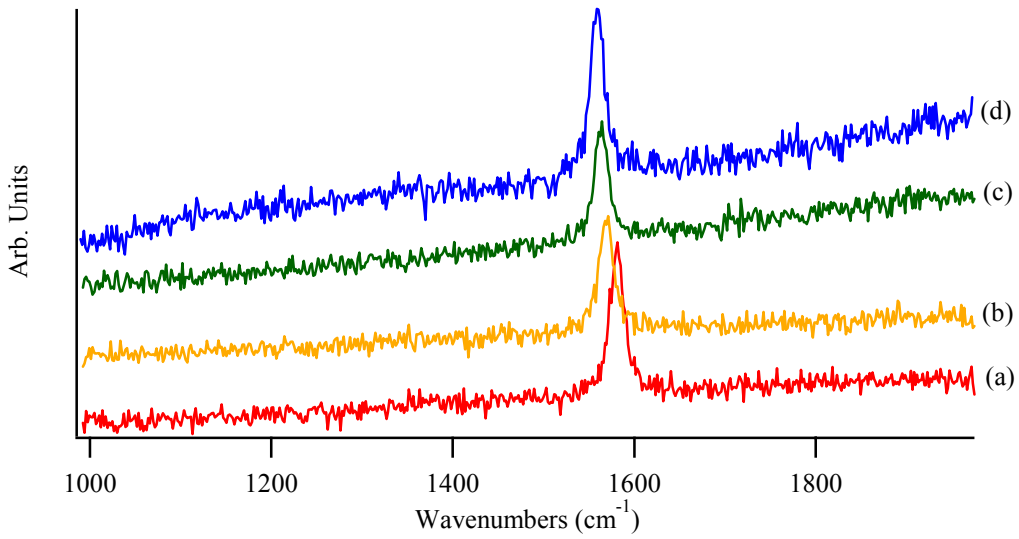

Figure V.5. Raman spectra of highly ordered pyrolytic graphite (HOPG) collected at (a) 20 °C, (b) 570 °C, (c) 640 °C, and (d) 715 °C which show that the band shifts from 1581 to 1561 cm^{-1} within the experimental temperature range in a non-linear manner consistent with previous studies.[28]

Acquisition of Raman spectra at elevated temperatures is particularly useful for studying kinetic processes occurring on SOFC materials. Of particular relevance for SOFC operation are the kinetics of reversible processes including Ni oxidation/reduction as well as carbon deposition and oxidation on anode substrates. Ni/YSZ cermets are the benchmark SOFC anode material and their resilience to redox cycling and resistance to oxidation under load is a matter of practical importance for SOFC applications. Previous studies of Ni oxidation and reduction have been applied to understand the kinetics and rate limiting steps of Ni anode oxidation and reduction and the detrimental effects of redox cycling on FC performance.[20,29,30] However, these studies all examined the condition of Ni anodes after operating the SOFC under controlled conditions and then cooling the assembly for post-mortem evaluation. Thus, researchers were left to infer how chemical and structural changes observed after operation corresponded to measured performance during operation.

Furthermore, additional processes (e.g., material contraction) are likely to occur during cooling that may complicate *ex-situ* measurements.

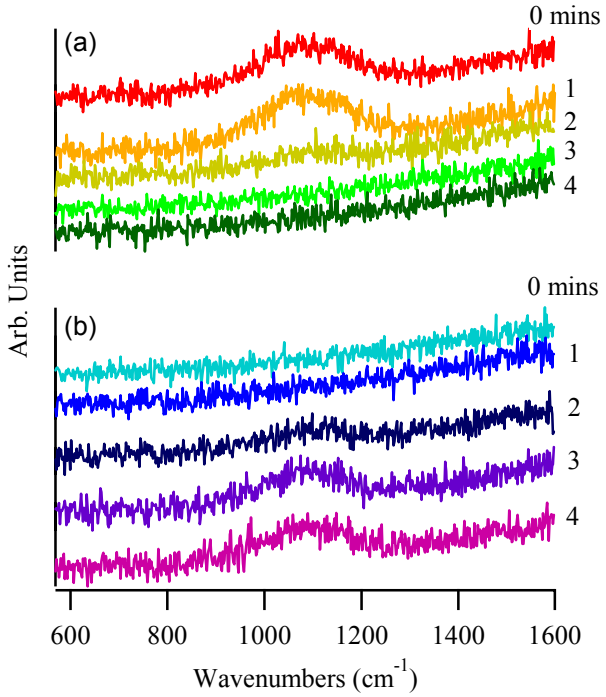

Figure V.6. The evolution of the NiO 2LO Raman second order band at 715 °C with scans collected every minute for (a) reduction of NiO with 33% H_2 in Ar and (b) oxidation of Ni in air.

Figure V.6a shows a series of timed acquisition Raman spectra taken from an oxidized Ni/YSZ cermet at 715˚C as the gas phase environment above the cermet changes from oxidizing (air) to reducing (1:2 H_2:Ar). Exposure to H_2 leads to a rapid decrease in the intensity of the NiO band at 1072 cm^{-1} as the NiO is reduced to metallic Ni. The data show that Ni reduction is complete within two minutes of initial exposure to H_2. In less reducing atmospheres (such as wet CH_4 (8% in Ar)) the reduction rates are slower, but the process is still completed within ten minutes of initial exposure. (Figure V.7) Switching the gas phase environment back to air (Figure V.6b) reoxidizes the Ni to NiO, and the process is again complete within minutes. These data show that *in-situ* Raman spectroscopy is sensitive enough to

report the loss and appearance of the NiO band as well as to follow the kinetics of this process on the timescale of minutes, a timescale that is particularly relevant for electrochemical processes occurring in SOFCs.[30]

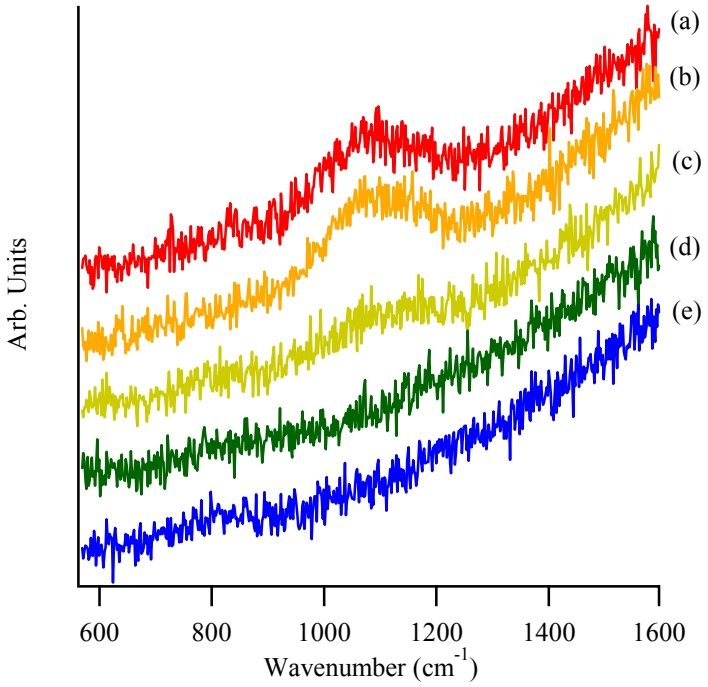

Figure V.7. Raman spectra showing the reduction rate of NiO in a wet CH_4 (4% H_2O, 8% CH_4 in Ar) flow. The presented spectra where aquired (a) 0, (b) 3, (c) 4, (d) 5, and (e) 6 min after the introduction of wet CH_4. The reduction rates are slower than in H_2 where Ni reduction is complete within two minutes of initial exposure.

A second species that plays an important role in SOFC chemistry is solid carbon deposited on anode surfaces by catalytically activated hydrocarbon fuels. In some instances, the presence of deposited carbon (or "coke") has improved SOFC power densities by as much as 40%.[31] The mechanism proposed for such enhancement is that the deposited carbon improves connectivity between electronically isolated metallic islands in the cermet resulting in enhanced current collection. However, carbon formation on anodes can also lead to diminished

performance and SOFC failure by occupying active sites and/or reducing transport through porous anode materials.[32]

Hindering the development of models that can predict the impact of carbon on SOFC performance is the lack of molecularly specific, *in-situ* data from these high temperature systems. Frequently, researchers need to infer how chemical and structural changes observed in post-mortem examinations correspond to chemical evolution that occurred at temperature during electrochemical operation. These studies are unable to account for any partial oxidation or annealing of deposited carbon that occurs as the entire assembly cools. Figure V.8 displays Raman spectra from a fully reduced Ni/YSZ cermet (top, featureless spectrum), a Ni/YSZ cermet that has been exposed to 5 mL of C_4H_{10} (second from top), and then successive spectra acquired as the Ni/YSZ surface is exposed to a weakly oxidizing atmosphere consisting of H_2O (4%) in Ar. The cermet exposed to C_4H_{10} shows the presence of carbon on the cermet surface as indicated by the characteristic carbon Raman D and G bands.[22] These data are important because they highlight our ability to observe directly chemical processes occurring at high temperatures. Furthermore, the quality of the spectra allow for a semi-quantitative evaluation of the type of carbon being deposited. The integrated D and G band intensities indicate with the amount of "disordered" (or sp^3) carbon present relative to the amount of ordered (or sp^2 "graphitic") carbon, respectively. A ratio of these two band intensities provides a quantitative measure of the effective domain size of the carbon deposits.[33] The spectrum shown in Figure V.8 has a D/G ratio of 1.3 corresponding to an average domain size of ~3-4 nm. We note, however, that D/G ratios observed *in-situ* show

tremendous spatial heterogeneity and are sensitive to duration and amount of exposure, location of the hydrocarbon source, and the presence of small amounts of molecular oxygen.

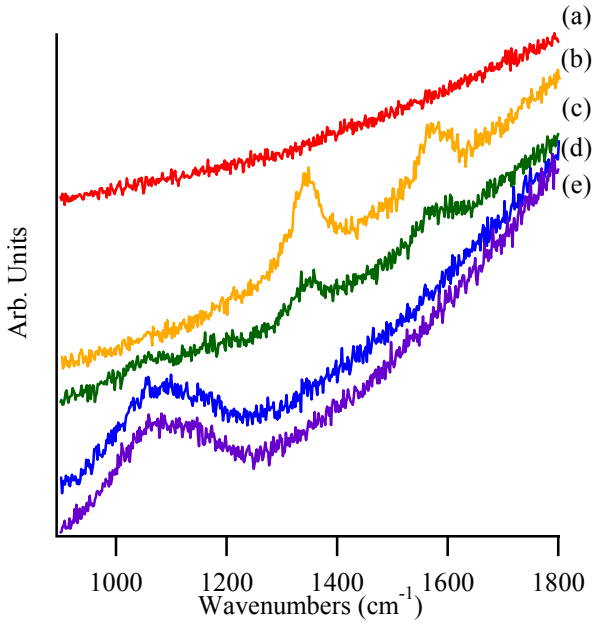

Figure V.8. High-temperature (715 °C) Raman spectra of (a) a Ni/YSZ cermet anode, (b) graphitic carbon peaks resulting from exposure to 5 mL of C_4H_{10}, (c) partial removal of the carbon and of the Ni/YSZ cermet oxidation after 3 minutes of wet (4% H_2O) Ar flow, (d) after 6 minutes of wet Ar flow, and (e) after 9 minutes of wet Ar flow. These scans show the capability of Raman spectroscopy to resolve kinetics.

In the presence of an inert or reducing atmosphere (Ar or H_2 in Ar), the signatures of deposited carbon remain stable for hours. However, the introduction of an oxidizing agent to the gas phase atmosphere above the carbon containing Ni/YSZ cermet leads to rapid degradation of the carbon deposits and the growth of NiO. The last three traces of Figure V.8 show the effects of adding H_2O (4%) to the Ar flowing through the cell. Spectra were acquired in 3 minute intervals. Soon after water is introduced to the Ar gas flow, the carbon bands diminish in intensity and the NiO band near 1060 cm^{-1} begins to emerge. In the first scan following the addition of water (covering the time of exposure t = 0 to 3 minutes), both the carbon and the NiO

bands can be seen. Given the absence of carbon features in the second spectrum after the introduction of water, we conclude that the carbon deposits have disappeared from the Ni/YSZ surface.

3B. *In-situ* Raman Data

Figure V.9 shows *in-situ* Raman spectra acquired from the same Ni/YSZ porous anode operating at three different cell voltages. The top, featureless trace results from a 1 minute scan of the clean anode operating with a H_2/Ar feed. Exposure to 5 cc of butane (at 1 atm and 296K in the rotometer) leads to the formation of carbon deposits on the anode. When significant current is being drawn from the cell (a cell potential of 0.46 V), a transient feature appears at 1585 cm^{-1}. (Figure V.9, left panel) This vibrational band is assigned to the G mode of graphite and it appears during the first minute after exposure.[22,23] At this cell potential, the graphite disappears in 2-3 minutes. Butane introduced at a higher cell voltage (0.76 V) again results in graphite formation. (Figure V.9, middle panel) Accompanying the pronounced G feature is weak, broad intensity centered near 1350 cm^{-1}. This lower frequency band is assigned to the D mode of carbon rings and is associated with disordered graphite having a disproportionately large number of defects, edges and/or grain boundaries.[22,23,34,35] Several minutes after exposure to a limited amount of butane, no detectable carbon remains on the anode operating at 0.76 V.

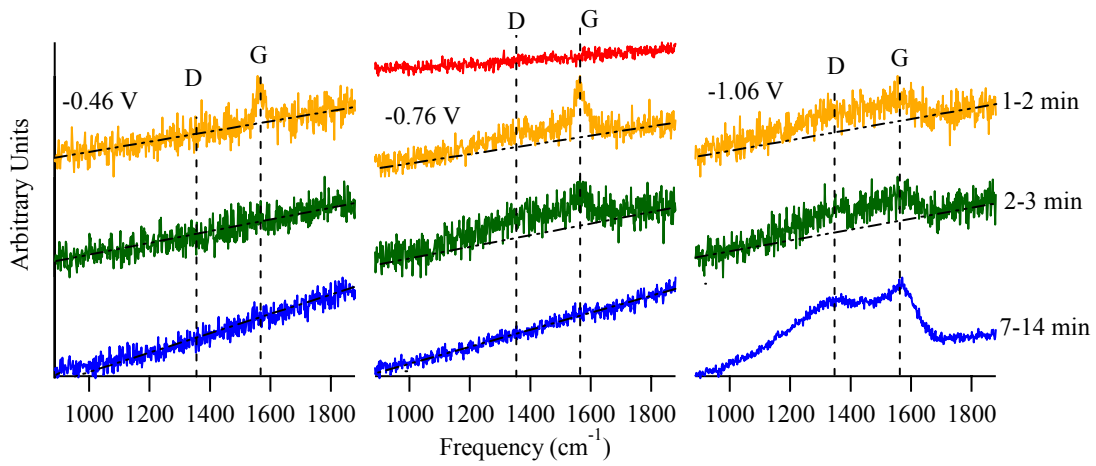

Figure V.9. Raman spectra acquired from a Ni/YSZ porous anode operating at 0.46 V (left), 0.76 V (center), and 1.06 V (= open circuit voltage) (right). The top, featureless trace results from a clean, reduced Ni/YSZ anode. When the cell voltage is 0.46 V, the G mode of graphite at 1585 cm^{-1} appears 1 min after exposure to 5 cc butane. (second row from top) After 2 min the graphite disappears. (third row from top) At a cell voltage of 0.76 V both the G and D peaks form 1 min after exposure to butane (second row from top) and are degrading, but still present after 2 min (third row from top). After several minutes no detectable carbon remains in the polarized anode cases (fourth row from top). When the cell is operated at OCV, both the G and D peaks form and remain indefinitely.

These observations have direct and immediate consequences for proposed mechanisms of electrochemical oxidation in SOFCs operating with hydrocarbon fuels. First, at low cell potentials (with correspondingly high oxide fluxes through the electrolyte) only highly ordered graphite forms. Higher potentials promote the formation of both ordered and disordered graphite. In both instances carbon deposition is reversible meaning that continued operation in the absence of additional carbon containing fuel oxidizes any graphitic deposits. When the cell is held at OCV (1.06 V) and exposed to butane, graphite grows quickly and irreversibly, an anticipated result given the ability of Ni to catalyze carbon-hydrogen bond cleavage.[36] In fact, introducing as little as 5 cc of butane forms so much graphite that the height of the surface changes altering the focusing conditions of the microscope assembly.

Re-optimization of the Raman signal, shows two broad, strong features in the OCV spectrum indicating large amounts of disordered graphite as evidenced by a broad D band (at 1350 cm^{-1}) accompanying the G band (at 1585 cm^{-1}). (Figure V.9, right panel) In the absence of an oxidant, these deposits are stable, persist indefinitely, and provide *in-situ* evidence of Ni's ability to promote autocatalytic formation of coke.[36,37]

The second fuel studied in this work was CO. Bursts of CO added to a H_2/Ar fuel feed led to no discernable features in the resulting Raman spectra. Instead, cells were operated with a continuous CO/Ar fuel feed for 30 min (corresponding to 2.7 L of CO exposure). Figure V.10 displays the Raman spectra of SOFC anodes polarized to three different cell potentials. Data are background corrected to accentuate differences between the three conditions. At OCV (1.06 V) the SOFC may show trace amounts of ordered graphite as evidenced by the shoulder at ~1570 cm^{-1}, this assignment is suspect given the experimental S/N of the experiment. At a moderate cell voltage of 0.76 V the G peak appears although its intensity is considerably smaller than that observed from just 5 cc of C_4H_{10}. A second weak feature at 1480 cm^{-1} is assigned tentatively to a Ni-COO intermediate species based on previous studies on similar surface systems.[38] When operating at a lower cell potential (0.46 V), the spectrum is once again featureless. We note that the vibrational bands in all spectra appearing in Figure V.10 are quite weak compared to those observed in the butane studies. However, the reproducible appearance and reversible behavior of the spectra with CO as a fuel instill confidence in the assignments.

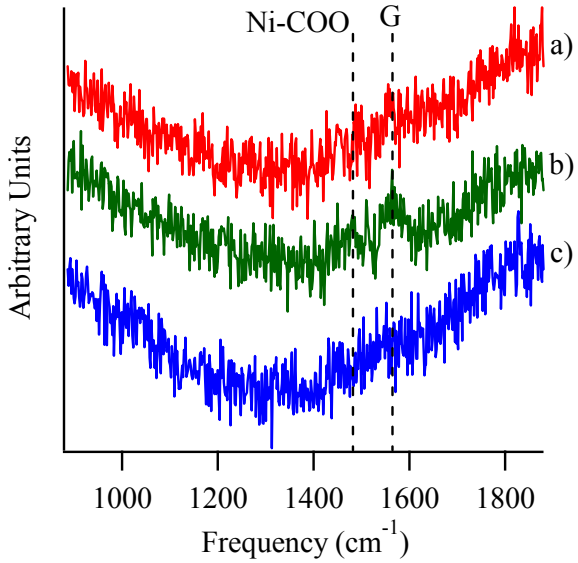

Figure V.10. Raman spectra acquired from a Ni/YSZ porous anode operating at 1.06 V (a), 0.76 V (b), and 0.46 V (c). At OCV (a) the SOFC shows a hint of a weak shoulder at ~1570 cm^{-1}. At a moderate cell voltage of 0.76 V (b) the G peak appears as well as a weak feature at 1480 cm^{-1}, assigned tentatively to Ni-COO. No distinguishable features appear at a cell voltage of 0.46 V (c).

Supporting the assignment of nickel carboxylate in the Raman spectra from anodes operated at intermediate potentials are independent, *ex-situ* X-ray photoelectron spectra of SOFC anodes operated with fuels at the same intermediate potential and cooled under Ar. The left panel of Figure V.11 shows XPS spectra of anodes operated with H_2 (a) and CO (b). Both spectra display a standard impurity of sp^3 hybridized carbon at 284.6 eV. This impurity results from ambient contaminants and disappears upon sputtering the sample. (Sputtering, however, also removes all surface species of interest.) Consequently the 284.6 eV feature is used as an internal calibrant. Anodes exposed to CO show a peak that appears at 288.4 eV. (Figure V.11b) This feature is absent in the XPS spectrum from the H_2 fueled SOFC.(Figure V.11a) Literature reports attribute C 1s peaks near 288.4 to various M-C-O species.[39] *Ex-situ* Raman spectra of SOFC anodes operated with H_2 and CO

and cooled under Ar are shown in Figure V.11c and V.11d, respectively. The presence of small NiO bands in the H_2 system (Figure V.11c) are likely results of residual water in the anode chamber. The spectrum in Figure V.11d (CO fuel) shows a strong feature assigned to the anti-symmetric stretch of carboxylate groups bound to Ni. The NiO bands in the CO case are not surprising considering that partial oxidation of the anode in a CO atmosphere can occur when the cell is polarized at modest potentials. Experiments are currently being carried out to quantify more accurately the dependence of nickel anode oxidation on cell operating conditions. Strong correlation between the XPS signal feature at 288.4 eV and the observed Raman band at ~1440 cm^{-1} supports the assignment of this species as a carboxylate adsorbed to the Ni.

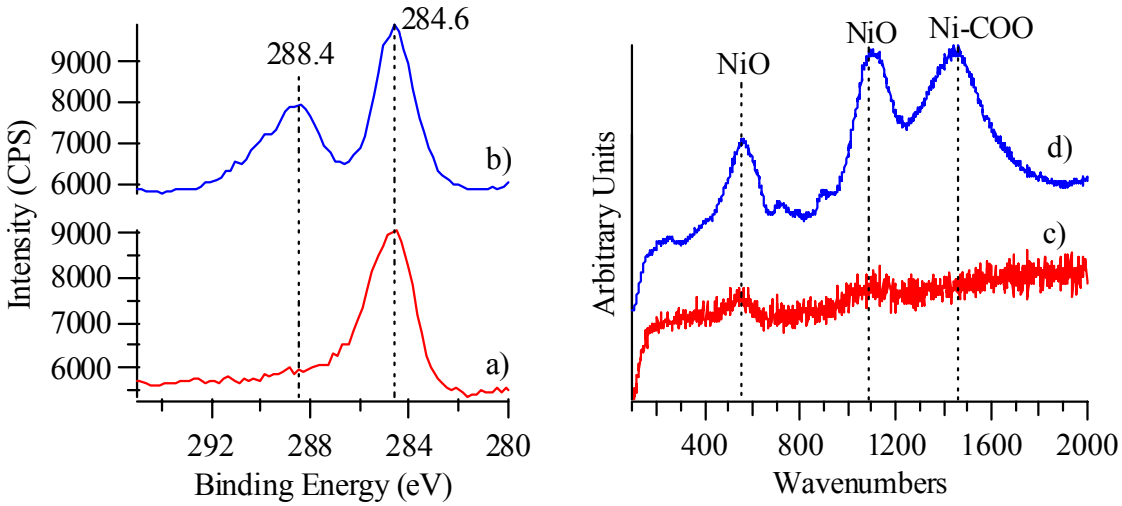

Figure V.11. XPS spectra in of the C 1s region of a SOFC anode operated with H_2 fuel (a) and CO fuel (b) and Raman spectra of a SOFC anode operated with H_2 fuel (c) and CO fuel (d). Both XPS spectra display a standard carbon impurity peak at 284.6 eV while the anode exposed to CO show a peak at 288.4 eV that is assigned to 288.4 to a Ni-C-O species. The Raman spectrum in (c) shows only very small NiO bands, indicated that the anode was only slightly oxidized, while the spectrum in (d) shows both NiO and Ni-COO bands. Please note that the spectrum in (c) has been expanded 4:1 on the y-axis against the spectrum in (d) to clearly show the NiO bands.

The Raman data obtained while operating with the two fuels show clearly that more graphite is produced at OCV with a hydrocarbon fuel than with CO. Furthermore, steady state concentrations of graphite with a CO feed depends sensitively on operating conditions with ordered graphite being the only extended carbon structure observed. Under no conditions explored in this work does disordered graphite appear on the Ni cermet anode operating with a CO fuel feed. The potential dependent appearance of ordered graphite with a CO fuel feed suggests that intermediate cell potentials may favor oxide-induced, Boudouard-type chemistry ($2\ CO_{(ads)} \rightarrow C_{(ads)} + CO_{2(g)}$)[40,41] or other side reactions (i.e. $2\ CO_{(ads)} \rightarrow 2\ C_{(ads)} + O_{2(g)}$) whereas anodes appear much more resistant to carbon deposition in both the high and low cell potential limits. Results also show that the structure of the carbon deposit from introducing butane to the SOFC depends on the cell's operating potential and corresponding oxide flux through the electrolyte. As the cell potential is increased (away from OCV conditions), the relative intensity of the D vibrational band increases, strongly suggesting that the higher oxide flux preferentially oxidizes the disordered, amorphous-like carbon. As a result, the graphitic G band (near 1585 cm^{-1}) is the sole feature observed at low cell potentials.

3C. Electrochemical Data

Having identified graphite to be the primary form of carbon deposited on Ni/YSZ anodes, we can now understand how graphite impacts overall cell performance. The "burst" technique employed in the butane experiments allows for characterization of incipient processes responsible for the impact of graphite on overall SOFC performance. Figure V.12 shows voltammetry data from a SOFC with

a Ni/YSZ cermet anode at OCV before C_4H_{10} exposure, after the 5th burst (25 cc cumulative exposure) and after the 15th burst (75 cc cumulative exposure). Overall, the results resemble those from previous studies that demonstrated improved cell performance correlated with extensive carbon growth.[9] However, additional insight into the mechanism of this behavior comes from data acquired at low C_4H_{10} exposure levels. During the initial stages of graphite formation the power density drops by approximately a factor of two, only to recover after additional graphite forms. Performance improves to the point that the power density after 15 bursts (75 cc) of C_4H_{10} approaches that of the SOFC prior to butane exposures. A possible cause of this systematic and reproducible variation in the electrochemical behavior is the initial blockage of active sites throughout the porous anode followed by improved current collection as graphite "wires together" more and more of the anode architecture.

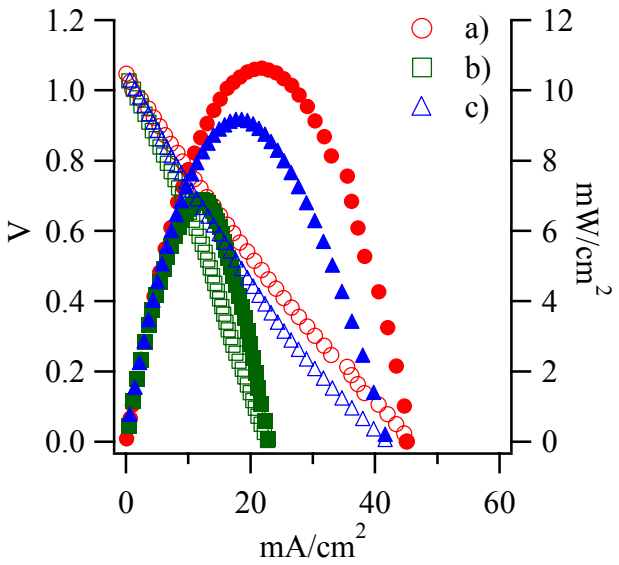

Figure V.12. Voltammetry (open marks) and power density (closed marks) data from a SOFC at OCV before C_4H_{10} (a) exposure and after the 5th (b) and 15th bursts (c) of butane corresponding to 25 and 75 cc exposure, respectively.

Unlike cells operated with butane, those using CO as the fuel show no connection between performance and the amount of deposited carbon. Rather, performance decreases as a function of cell operating voltage and does not recover. Figure V.13 shows voltammetry data from an SOFC operating with CO following 20 min of stable operation at each voltage. While the trace amounts of carbon observed in Raman spectra may play a small role in reduced SOFC performance (as is the case following exposure to small amounts of C_4H_{10}), a more likely explanation of the data is that at lower potentials the oxide flux through the YSZ electrolyte is sufficient to oxidize the Ni in the anode especially near the interface with the electrolyte. Similar effects are not seen in cells operating with the C_4H_{10} bursts, because the persistent presence of excess H_2 keeps the Ni reduced and therefore electrocatalytically active. Supporting this picture are ongoing *ex-situ* experiments that profile NiO formation through anode cross sections.

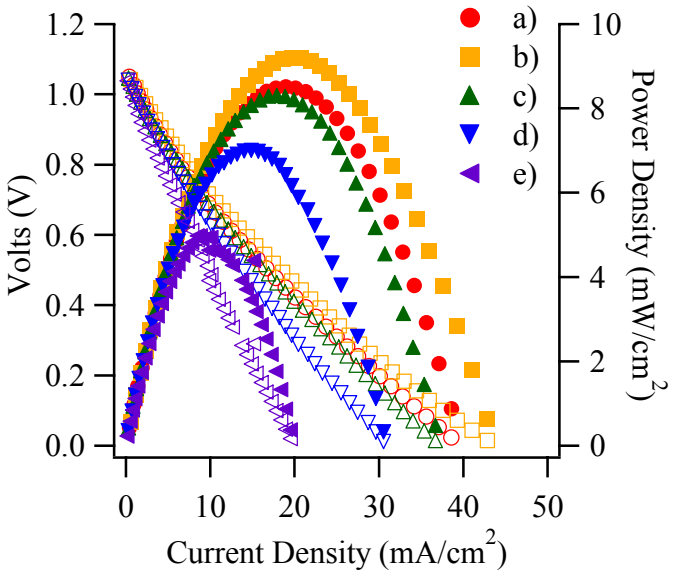

Figure V.13. Voltammetry (open marks) and power density (closed marks) data from an SOFC operated with CO following 20 min of stable operation at OCV (a), 0.91 V (b), 0.76 V (c), 0.81 V (d) and 0.46 V (e).

4. Conclusion

Data show Raman spectroscopy to be a very valuable means of characterizing *in-situ* chemical processes occurring in high temperature environments. Specific systems examined in this work are particularly relevant for the operation of SOFCs, and include temperature dependent structural changes in YSZ electrolytes, reversible reduction and oxidation of Ni, carbon formation from hydrocarbon feeds and subsequent oxidation of the deposited carbon by atmospheric H_2O.

Furthermore, these studies provide the first direct, *in-situ* measurements of chemical intermediates present on SOFC anodes under realistic operating conditions. Both C_4H_{10} and CO form graphitic intermediates but under very specific and very different conditions. In the limit of a large oxide flux, excess butane forms ordered graphite but only transiently. At higher cell potentials ordered and disordered graphite form on the Ni anode following exposure to butane. Again these deposits are oxidized if the cell continues to operate without a source of carbon in the fuel feed. The most graphite forms on Ni anodes held under OCV conditions and the distribution is weighted heavily towards disordered graphite. The chemistry of CO oxidation should be simpler given that CO requires adding one oxygen to form CO_2. However, the *in-situ* Raman data tell a more complicated story. At intermediate cell potentials ordered graphite forms and a target intermediate on the path to CO oxidation appears. These species are not evident at higher or lower cell potentials. Taken together, the results presented in this work provide the first direct, *in-situ* identification of chemical species present in SOFCs operating under realistic

conditions. Such information will prove essential in establishing quantitative, predictive mechanisms for these technologically important devices.

5. References

(1) Holtappels, P.; De Haart, L. G. J.; Stimming, U.; Vinke, I. C.; Mogensen, M. *J. Appl. Electrochem.* **1999**, *29*, 561.

(2) Lin, Y.; Zhan, Z.; Liu, J.; Barnett, S. A. *Solid State Ionics* **2005**, *176*, 1827.

(3) Primdahl, S.; Mogensen, M. *J. Electrochem. Soc.* **1997**, *144*, 3409.

(4) Alanne, K.; Saari, A.; Ugursal, V. I.; Good, J. *J. Power Sources* **2006**, *158*, 403.

(5) Calise, F.; Palombo, A.; Vanoli, L. *J. Power Sources* **2006**, *158*, 225.

(6) Fontell, E.; Phan, T.; Kivisaari, T.; Keranen, K. *J. Fuel Cell Sci. Technol.* **2006**, *3*, 242.

(7) Atkinson, A.; Barnett, S.; Gorte, R. J.; Irvine, J. T. S.; McEvoy, A. J.; Mogensen, M.; Singhal, S. C.; Vohs, J. *Nature Materials* **2004**, *3*, 17.

(8) McIntosh, S.; He, H. P.; Lee, S. I.; Costa-Nunes, O.; Krishnan, V. V.; Vohs, J. M.; Gorte, R. J. *J. Electrochem. Soc.* **2004**, *151*, A604.

(9) McIntosh, S.; Vohs, J. M.; Gorte, R. J. *J. Electrochem. Soc.* **2003**, *150*, A470.

(10) Minh, N. Q. *Solid State Ionics* **2004**, *174*, 271.

(11) Dong, J.; Cheng, Z.; Zha, S. W.; Liu, M. L. *J. Power Sources* **2006**, *156*, 461.

(12) Lu, X.; Faguy, P. W.; Liu, M. L. *J. Electrochem. Soc.* **2002**, *149*, A1293.

(13) Sum, O. S. N.; Djurado, E.; Pagnier, T.; Rosman, N.; Roux, C.; Siebert, E. *Solid State Ionics* **2005**, *176*, 2599.

(14) Bebelis, S.; Neophytides, S. *Solid State Ionics* **2002**, *152-153*, 447.

(15) Bieberle, A.; Meier, L. P.; Gauckler, L. J. *J. Electrochem. Soc.* **2001**, *148*, A646.

(16) Bieberle, A.; Gauckler, L. J. *Solid State Ionics* **2002**, *146*, 23.

(17) Sunde, S. *Electrochim. Acta* **1997**, *42*, 2637.

(18) Lu, X. Y.; Faguy, P. W.; Liu, M. L. *J. Electrochem. Soc.* **2002**, *149*, A1293.

(19) Song, C. S. *Catal. Today* **2002**, *77*, 17.

(20) Waldbillig, D.; Wood, A.; Ivey, D. G. *J. Power Sources* **2005**, *145*, 206.

(21) Xu, C.; Xu, G.; Wang, G. *J. Mater. Sci.* **2002**, *38*, 779.

(22) Kakihana, M.; Osada, M. Raman Spectroscopy as a Characterization Tool for Carbon Materials. In *Carbon Alloys: Novel Concepts to Develop Carbon Science and Technology*; Yasuda, E., Inagaki, M., Kaneko, M., Endo, M., Oya, A., Tanabe, Y., Eds.; Elsevier Science, Ltd.: Oxford, UK, 2003; pp 285.

(23) Tuinstra, F.; Koenig, J. L. *J. Chem. Phys.* **1970**, *53*, 1126.

(24) Pomfret, M. B.; Stoltz, C.; Varughese, B.; Walker, R. A. *Anal. Chem.* **2005**, *77*, 1791.

(25) Cai, J.; Raptis, C.; Raptis, Y. S.; Anastassakis, E. *Phys. Rev. B* **1995**, *51*, 201.

(26) Feinberg, A.; Perry, C. H. *J. Phys. Chem. Solids* **1981**, *42*, 513.

(27) Yang, Y. L.; Yan, H. W.; Fu, Z. P.; Yang, B. F.; Xia, L. S.; Xu, Y. D.; Zuo, J.; Lu, F. Q. *J. Phys. Chem. B* **2006**, *110*, 846.

(28) Tan, P. H.; Deng, Y. M.; Zhao, Q.; Cheng, W. C. *Appl. Phys. Lett.* **1999**, *74*, 1818.

(29) Malzbender, J.; Wessel, E.; Steinbrech, R. W. *Solid State Ionics* **2005**, *176*, 2201.

(30) Tikekar, N. M.; Armstrong, T. J.; Virkar, A. V. *J. Electrochem. Soc.* **2006**, *153*, A654.

(31) McIntosh, S.; Vohs, J. M.; Gorte, R. J. *J. Electrochem. Soc.* **2003**, *150*, A470.

(32) Kim, T.; Liu, G.; Boaro, M.; Lee, S. I.; Vohs, J. M.; Gorte, R. J.; Al-Madhi, O. H.; Dabbousi, B. O. *J. Power Sources* **2006**, *155*, 231.

(33) Ferrari, A. C.; Robertson, J. *Phys. Rev. B* **2000**, *61*, 14095.

(34) Chhowalla, M.; Ferrari, A. C.; Robertson, J.; Amaratunga, G. A. J. *Appl. Phys. Lett.* **2000**, *76*, 1419.

(35) Rao, A. M.; Richter, E.; Bandow, S.; Chase, B.; Eklund, P. C.; Williams, K. A.; Fang, S.; Subbaswamy, K. R.; Menon, M.; Thess, A.; Smalley, R. E.; Dresselhaus, G.; Dresselhaus, M. S. *Science* **1997**, *275*, 187.

(36) Reinhold, M.; McGrady, J. E.; Perutz, R. N. *J. Am. Chem. Soc.* **2004**, *126*, 5268.

(37) Abild-Pederson, F.; Lytken, O.; Engbaek, J.; Nielsen, G.; Chorkendorff, I.; Norskov, J. K. *Surf. Sci.* **2005**, *590*, 127.

(38) Li, C.; Sakata, Y.; Arai, T.; Domen, K.; Maruya, K.; Onishi, T. *J. Chem. Soc., Faraday Trans. I* **1989**, *85*, 929.

(39) Wagner, C. D.; Naumkin, A. V.; Kraut-Vass, A.; Allison, J. W.; Powell, C. J.; Rumble, J. R. NIST X-ray Photoelectron Spectroscopy Database; Version 3.4 ed.; National Institute of Standards and Techonology, 2003; Vol. 2005. http://srdata.nist.gov/xps/.

(40) Laosiripojana, N.; Assabumrungrat, S. *Chem. Eng. Sci.* **2006**, *61*, 2540.

(41) Nakano, H.; Ogawa, J.; Nakamura, J. *Surf. Sci.* **2002**, *514*, 256.

Chapter 6: Hydrocarbon fuels in solid oxide fuel cells: *In-situ* Raman studies of graphite formation and oxidation

1. Introduction

Solid oxide fuel cells (SOFCs) offer great potential for clean, highly-efficient power generation in a growing, hydrogen-based, global economy.[1-3] SOFC development has been pursued vigorously in recent years because of their potential to achieve electrical energy conversion efficiencies approaching 70% in conjunction with a gas turbine cycle and noise levels that are ~20 dB below those of conventional turbine engines.[4] These cells are already being developed for an array of commercial applications, including public transportation.[5] Unlike low-temperature proton-exchange membrane fuel cells (PEMFC's), SOFCs with their high operating temperatures have the potential to convert a wide range of fuels – not just molecular hydrogen – into electricity and simple chemical byproducts.[6-10]

Despite the expected tolerance of SOFCs to most hydrocarbon fuels that reduce performance in other devices, SOFCs are still susceptible to carbon deposition (or "coking") from carbon-containing fuels in the porous anode architectures. Excessive carbon deposition represents a primary mechanism for anode destruction and, ultimately, device failure.[11-15] The specific chemical mechanisms responsible for carbon deposition in SOFC anodes remain uncertain. Elemental nickel (Ni) – the most common anode electrocatalyst – is a well known catalyst for C-H bond activation and subsequent graphite formation under appropriate conditions.[16,17] Furthermore, carbon deposition is thought to be autocatalytic,[18-20] meaning that trace

amounts of carbon on the anode will rapidly promote further growth. To avoid carbon formation on porous, Ni-based anodes particularly those exposed to higher molecular weight hydrocarbon fuels, there must be adequate oxidizing agents in the form of a) oxide ions that migrate through the electrolyte to the electrochemically active region and/or b) steam formed from hydrocarbon oxidation or added intentionally to the fuel inlet.[21,22] Functionally-graded porous anode structures with outer diffusion barriers have been developed to foster improved hydrocarbon steam reforming by increasing the water product concentration within the porous media.[23-26]

Understanding the mechanism(s) of carbon formation on SOFC anodes is limited by a lack of knowledge about the molecular species present in the gas phase as well as on the electrocatalyst and electrolyte surfaces. Most hydrocarbon fuels undergo extensive pyrolysis at temperatures common in operational SOFCs. For example, at temperatures above 650 ˚C, butane undergoes gas-phase pyrolysis to form smaller saturated and unsaturated hydrocarbons. A representative distribution of the products formed at 800 ˚C shows that a fuel stream originally consisting of butane contains (by mole fraction) 39.8% ethylene, 36.3% methane, 13.0% propylene, 5.6% ethane, and only 4.3% butane.[27] Such a heterogeneous mixture is likely to lead to multiple pathways for fuel oxidation as well as carbon deposition. The associated coupled chemistry further complicates efforts toward modeling electrochemical mechanisms and kinetics, fuel utilization efficiencies and device durability.

The general lack of molecularly specific data acquired during SOFC operation presents a critical impediment to understanding chemistry in SOFC anodes.

Numerous challenges confront the use of optically-based spectroscopic techniques at temperatures in excess of 700 ˚C, where typical SOFC electrolytes such as yttria-stabilized zirconia (YSZ) need to operate. While voltammetry and electrochemical impedance spectroscopy (EIS) can show clearly how cell performance responds to varying conditions,[7,28], results from these measurements do not reveal the molecular origins of observed changes. Recently, Raman spectroscopy has emerged as a promising *in-situ* tool for probing processes in operating SOFCs.[29,30] Raman spectroscopy measures vibrational transitions meaning that the technique is inherently sensitive to molecular and material identity. By examining vibrational band intensities and frequencies, one can observe directly molecular structure as well as interactions between species. Furthermore, with the appropriate choice of excitation wavelength, one can avoid the blackbody background problems that plague traditional IR absorbance based measurements.[30]

Experiments described below present a study of carbon formation and subsequent electrochemical oxidation in SOFCs operating with various hydrocarbon fuels. Raman spectroscopy is used to characterize *in-situ* the carbon formed on Ni/YSZ cermet anodes in an SOFC operating at 715 °C. The effect of cell potential on the oxidation of the deposits is characterized using timed-acquisition Raman spectra. The hydrocarbon fuels used in these studies – methane, ethylene and propylene – were chosen because they represent the primary components of butane pyrolysis in a study that most closely compares to our conditions (accounting for nearly 90% of the carbon products found in a butane feed that has passed through a high temperature fuel delivery line).[27] Butane is often used as a simple "heavy"

hydrocarbon fuel, and previous studies examining butane-fed SOFC's have shown that carbon deposition can have nonintuitive effects on SOFC performance. For example, McIntosh, et. al. reported enhanced power production from porous ceria anodes when butane was used as a fuel.[28,31] *Ex-situ* analysis of the anodes showed that these anodes had suffered significant carbon deposition. To explain their observation, the authors proposed a mechanism whereby conducting polyaromatic hydrocarbon deposits improved the connectivity of the porous anode, thus increasing the effective anode surface area and improving current collection.[12,31] Other studies have shown unequivocally that nanocrystalline graphite is the conducting carbon species contributing to cell performance enhancement on similar Cu/CeO_2 anodes.[32,33] Collectively, these studies raise the possibility that carbon deposition can actually improve SOFC performance under controlled circumstances.

This study presents spectroscopic data showing that smaller hydrocarbon fuels lead to distinctly different types of carbon deposits on Ni/YSZ cermet anodes. Simultaneous electrochemical measurements provide direct correlation between the carbon formed on the anode and overall device performance. Correlations between the different carbon structures formed and the hydrocarbon fuel imply that no single post-pyrolysis species is responsible for the cell behavior observed with butane fuel feeds. Carbon formed from propylene shows the strongest resemblance to that formed by butane, but propylene-formed deposits do not result in the same electrochemical enhancement observed with carbon deposits produced from direct butane feeds. These results suggest that carbon deposition in SOFC anodes reflects a complicated dependence on the pyrolysis species present. Results presented in this

work mark the first attempts to isolate the contributions of individual hydrocarbon species on SOFC anode performance. These studies provide the molecularly specific data necessary for spurring development of kinetic models that can describe accurately SOFC behavior and durability under a wide variety of anticipated operating conditions.

2. Experimental

2A. Fuel Cell Construction

The SOFC electrolytes were constructed using 8 mole% yttria stabilized zirconia (YSZ) powder acquired commercially from Tosoh. 2 g of the powder were pressed at 20,000 psi for 10 min and then sintered at 1500 °C for 1 hour with a heating and cooling rate of 1 °C per minute. The resulting electrolyte disks had diameters of 25 mm and thicknesses of 0.80 mm. The porous anodes are made using Ni/YSZ paste (50% Ni, 50% YSZ by weight, post-reduction) acquired from NexTech Materials (Lot # 112-45). The 12.5 mm diameter anodes were tape-cast in the center of the electrolyte disk with and sintered at 1300 °C for 3 hours with a heating and cooling rate of 1 °C per minute, resulting in a thickness of ~20 μm. Porous cathodes were made from a LSM/YSZ (50% $La_{0.85}Sr_{0.15}MnO_3$ and 50% YSZ by weight) paste made in-house. The paste was tape-cast in a 12.5 mm diameter area opposite the anode and sintered. The sintering procedure for the cathode was multi-stepped and included heating to 400 °C at 0.33 °C per min, holding the temperature at 400 °C for 1 hour, heating to 1300 °C at 1 °C per min, holding the temperature at 1300 °C for 1 hour, and cooling to room temperature at 3 °C per min.

Gold wires were attached to the anodes and cathodes of the completed membrane-electrode assemblies (MEAs) using Au ink (Engelhard #A1644) and Pt ink (Engelhard #6926), respectively. Once the wires had adhered, the disks were attached anode-side-out to an alumina tube assembly with zirconia paste. A quartz tube, closed on one end, encased the alumina-supported MEA. The cathode and anode chambers were sealed with tapered, silicone rubber plugs (McMaster-Carr). A split-tube furnace (ThermCraft) was fitted around the upper two-thirds of the assembly while the bottom was cooled by water and compressed air to preserve seals. A schematic of the assembled fuel cell rig is shown in Figure VI.1.

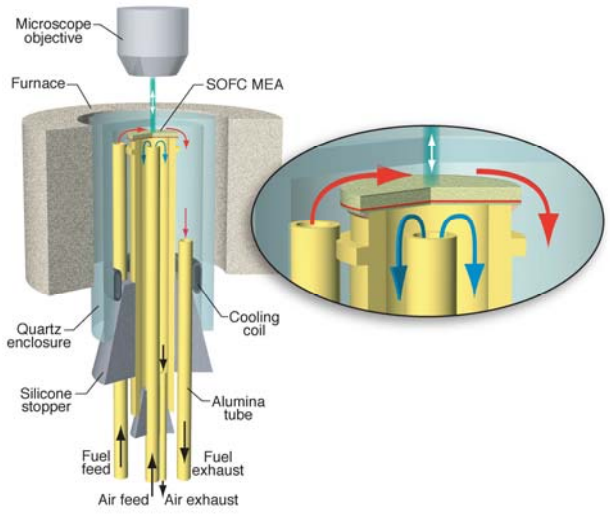

Figure VI.1. This schematic shows the optically accessible, electrochemical rig used to acquire Raman data from SOFCs operated at 715 ˚C.

2B. Gas Flows

Fuel flows must be regulated to keep the optical window clean while a constant cell polarization is applied. To sustain constant cell voltage an argon/hydrogen feed was flowed (150 sccm Ar, 30 sccm H_2). 5 cc of a specified hydrocarbon was then "burst" for 10 s on top of the base Ar/H_2 flow. This technique allows for the investigation of the effects of cell exposure to hydrocarbons on a well

resolved time scale. For electrochemical data collection, the anode-side flow was 150 sccm Ar and 100 sccm H_2. In the case of a constant methane flow, the fuel feed was 150 sccm Ar, 25 sccm methane. 90 sccm of Air was flowed over the cathode during all measurements. Rotameters (Omega) regulated flow rates with precisions of ± 1 sccm, and all experiments described in this work use "dry" (i.e., non-humidified) gases.

2C. Electrochemical Operation and Data Collection

Cell polarization and electrochemical measurements were taken by a Gamry Instruments PCI4 Potentiostat/Galvanostat/ZRA. Cells were polarized at three voltages: open circuit voltage (OCV or 1.05 V), 0.75 V, and 0.45 V. Throughout this text, descriptions of cell operating conditions will refer to cell potentials in terms of magnitude relative to OCV. In other words, cells operated at "low" potential correspond to (relatively) high currents and a cell potential having small magnitude (such as 0.45 V). The use of dry H_2 led to some variability in the measured OCV. This sensitivity results from the fact that the OCV reflects a balance between reactants (H_2, O^{2-}) and products (H_2O) due to the dependence of the Nernst Equation on the equilibrium constant. The exceedingly low partial pressures of $H_2O_{(g)}$ in the anode chamber meant that the measured OCV was susceptible to very small numbers in the denominator of K_{eq}. Previous studies have shown that the OCV can drop by approximately 0.1 V when the H_2 partial pressure is reduced to 0.1 atm.[34]

Typically, the OCV measured for the cells in this study was between 1.05 and 1.10 V. During the course of an individual series of experiments (carried out using the same cell), however, OCV varied by less than 0.02 V. Voltammetry and EIS

measurements were made periodically during the Raman experiments to ensure proper cell operation. In order to avoid carbon oxidation, experiments designed to study the growth of carbon deposits left cells at OCV during hydrocarbon exposure. In these experiments, impedance was measured after every hydrocarbon "burst" and voltammetry measurements were made after the 5^{th}, 10^{th}, and 15^{th} "bursts". Linear voltammetry sweeps with only H_2 as the fuel species were conducted between OCV and 0.00 V cell potential with a scan rate of 10 mV/s and a step size of 20 mV. Electrochemical impedance data also with only H_2 at OCV as the fuel were acquired between frequencies of 100,000 Hz and 0.05 Hz with 10 points per decade and an AC excitation voltage of 10 mV. The cathode effects can be identified with the high frequency arc noticed in all of the impedance plots and were identified by symmetric cell experiments discussed elsewhere.[35] The IR loss attributed to the electrolyte is subtracted from each V-I plot.

2D. Raman Measurements

Raman spectra were obtained with a Renishaw In-Via Raman microscope using a custom-built optical accessory that allowed the microscope objective to be lowered into the furnace to focus the incident beam on the anode surface. The objective is cooled by a constant flow of compressed air. Samples were irradiated with the 488 nm output of an Ar^+ ion laser (25 mW) focused to a 1 μm-sized spot. For each fuel, Raman spectra of the anode surface were acquired immediately before exposure to the hydrocarbon (30 1 s scans), and every minute for the first 4 minutes after exposure (30 1 s scans for each). This measurement was followed immediately

by a 200 s scan to improve the signal-to-noise ratio of any species that remained on the anode surface.

The spectra presented in the next section show two features associated with the formation of graphitic carbon. The vibrational band at 1585 cm^{-1} arises from extended domains of highly ordered graphite and is generally labelled "G" (for graphite) or by its symmetry, E_{2g}.[36] The band at 1365 cm^{-1} – labelled in most references as either "D" or A_{1g} – is much broader and corresponds to tetrahedral carbon defects within a graphite lattice.[36] Some reports associate this low frequency feature explicitly with "disorder",[37] although this disorder could result from a multitude of sources such as grain boundaries, point vacancies, or chemical heterogeneity. In the discussion below, G and D labels are used to assign graphitic features formed on Ni/YSZ anodes from carbon-containing gas phase fuels. When interpreting the magnitude of the D band in terms of the type of carbon formed, we use the term "disorder" to refer explicitly to carbon that disrupts the extended, sp^2 bonding characteristic of highly ordered graphite.

3. Results and Discussion

3A. Potential Dependence of Carbon Deposition

Methane, ethylene and propylene were introduced into SOFCs operating at three different cell potentials using the "burst" technique. Figure VI.2 shows *in-situ* Raman spectra of systems operated with methane. The top, featureless trace results from a 30 s scan of the clean anode operating with a hydrogen/Argon feed. Exposure to 5 cc of methane (or ~2.0 x 10^{-4} moles) at 1.05 V (OCV) leads to no measurable signal, indicating a lack of carbon deposits on the anode. Carbon also fails to deposit with methane exposure under moderate and high current conditions (corresponding to

cell potentials of 0.75 V and 0.45 V, respectively as shown in Figure VI.2, center and right panels). While the absence of carbon deposits under typical operating conditions with O^{2-} fluxes from the electrolyte and product H_2O generation should not be surprising, the lack of carbon deposition on the Ni/YSZ anode with methane at OCV contrasts dramatically with the higher weight hydrocarbons. Butane, for example, will form large amounts of disordered graphite on Ni cermet anodes at OCV with exposures of $\leq$ 1 cc (4×10^{-5} moles) as indicated in the Raman data from a SOFC operated with butane in Figure VI.3. When the SOFC is operating, the carbon formed by butane on the Ni cermet anode persists for a time that depends upon cell potential. Higher cell potentials (and correspondingly lower currents) lead to longer carbon persistence and vice versa.[30] At OCV, the graphite formed by butane remains stable indefinitely. As noted by Sheng and Dean, butane in SOFC feeds rarely survives intact due to high-temperature, gas-phase pyrolysis, and methane is the second most abundant pyrolysis product (36.3% by mole fraction)[27]. However, methane is unable to form detectable carbon deposits even under OCV conditions due to its lack of a C-C bond and associated reduced activity in comparison to butane.[38,39] This lower reactivity allows spectroscopic experiments to use a constant flow (25 sccm) of methane (on top of an Ar diluent) without risk of forming carbon deposits on windows and occluding optical transparency. (Figure VI.4) The carbon that forms on the cermet anode at OCV appears to take the form solely of ordered graphite as evidenced by the single discernable feature at 1580 cm^{-1}, assigned to the graphitic G band.

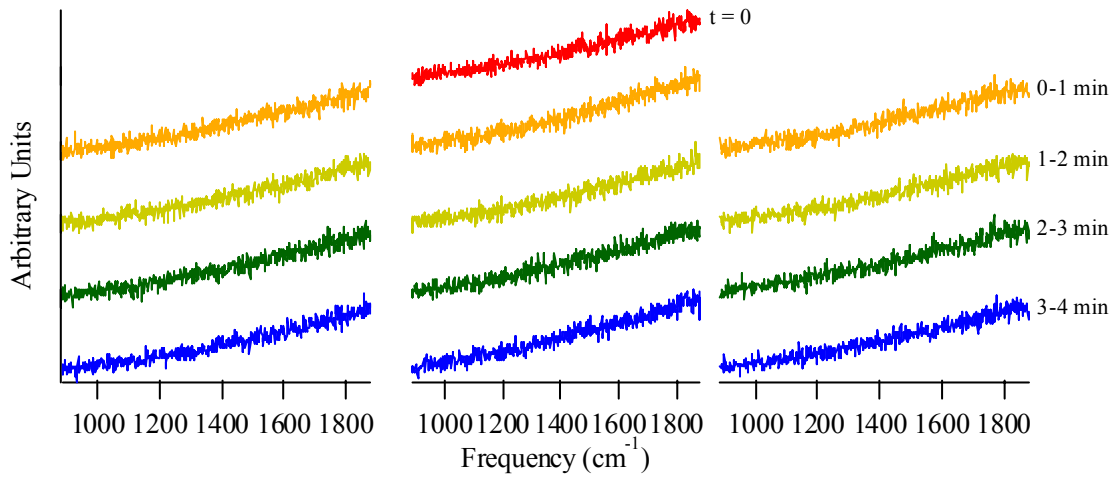

Figure VI.2. Raman spectra acquired from a Ni/YSZ porous anode operating at 1.05 V (OCV) (left), 0.75 V (center), and 0.45 V (right). The top, featureless trace results from a clean, reduced Ni/YSZ anode. A burst of 5 cc of methane leads to no measurable carbon deposition on the anode surface.

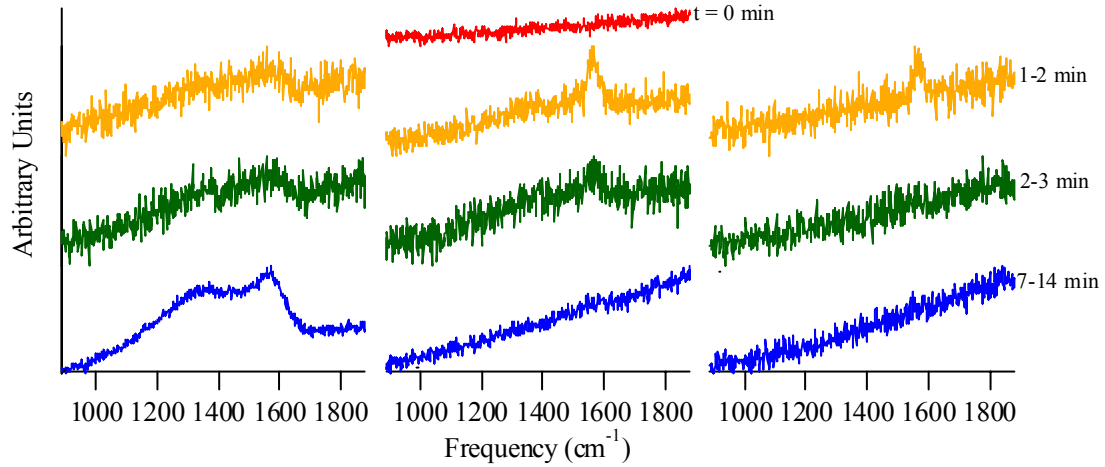

Figure VI.3. Raman spectra acquired from a Ni/YSZ porous anode operating at 1.06 V (OCV) (left), 0.76 V (center), and 0.46 V (right) and with butane as the fuel. The top, featureless trace results from a clean, reduced Ni/YSZ anode. When the cell voltage is 0.46 V, the G mode of graphite at 1585 cm^{-1} appears 1 min after exposure to 5 cc butane. (second row from top) After 2 min the graphite disappears. (third row from top) At a cell voltage of 0.76 V both the G and D peaks form 1 min after exposure to butane (second row from top) and are degrading, but still present after 2 min (third row from top). After several minutes no detectable carbon remains in the polarized anode cases (fourth row from top). When the cell is operated at OCV, both the G and D peaks form and remain indefinitely.

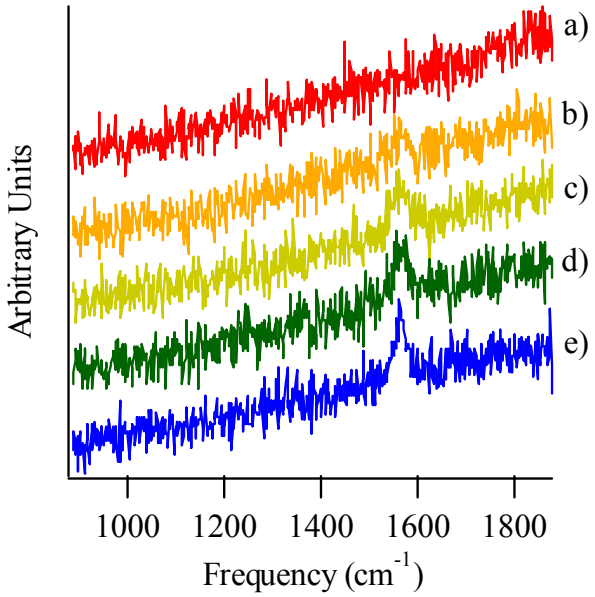

Figure VI.4. Raman spectra acquired from a Ni/YSZ anode surface as a constant flow of 25 sccm methane is flowed. The top spectrum (a) is of the anode surface before exposure to methane. The subsequent spectra were acquired at 0-1 min (b), 1-2 min (c), 4-5 min (d), and 8-9 min (e). This series shows a clear, controlled growth of ordered graphite deposits.

Figure VI.5 shows *in-situ* Raman spectra acquired from a Ni/YSZ cermet anode operating with ethylene (C_2H_4). Ethylene is the major component of butane gas phase pyrolysis (under the conditions employed in these studies), comprising 39.8% of the products.[27] Like Figure VI.2, the top, featureless trace results from a 30 s scan of the clean anode operating at OCV with a hydrogen/argon feed. Unlike methane, a single 5 cc burst of ethylene leads to observable formation of carbon deposits on the anode as evidenced by the vibrational band that appears at 1585 cm^{-1}. (Figure VI.5, second row) This vibrational band is assigned to the G mode of highly ordered graphite and it appears during the first minute after exposure. The propensity of ethylene to form carbon deposits on the Ni/YSZ anode mirrors that of butane with one important difference. Exposure to 5 cc of butane leads to the formation of both ordered and disordered graphite based on the distinct G and D bands in the Raman

spectrum (at 1585 cm^{-1} and 1360 cm^{-1}, respectively).[30] Furthermore, the low frequency feature characteristic of disordered graphite dominates the graphite formed from butane, whereas the same D band from the graphite formed from ethylene is much weaker and not well resolved in these short scans. Only in longer, higher S/N spectra (acquired under OCV conditions) can a weak D signal be observed in the graphite formed on the Ni/YSZ anode by ethylene. (*Vide infra*.)

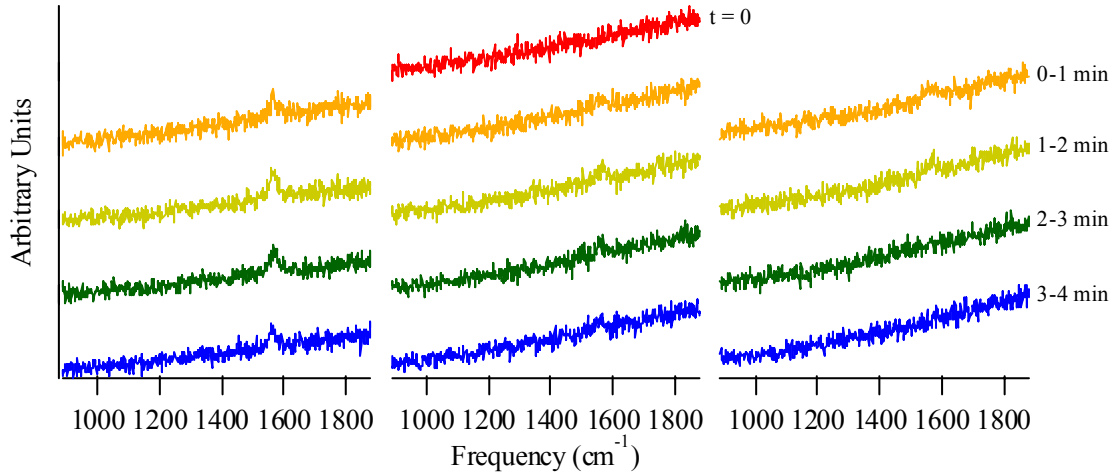

Figure VI.5. Raman spectra acquired from a Ni/YSZ porous anode operating at 1.05 V (OCV) (left), 0.75 V (center), and 0.45 V (right). The top, featureless trace results from a clean, reduced Ni/YSZ anode. When the cell voltage is 0.45 V, the G mode of graphite at 1585 cm^{-1} appears 1 min after exposure to 5 cc ethylene. (second row from top) After 2 min the graphite disappears. (third row from top) At a cell voltage of 0.75 V the G peak again forms 1 min after exposure to ethylene (second row from top) and degrades. When the cell is operated at OCV, the G peak forms and remains indefinitely. These short acquisitions (30 1 s scans) do not resolved the D peak.

Under OCV conditions, the G and D bands of ethylene-formed graphite persist indefinitely (under both Ar and Ar/H_2 mixtures), indicating that the graphite formed with ethylene is stable in the absence of an oxide flux through the electrolyte. At the lower cell potentials of 0.75 V and 0.45 V the graphite formed from an ethylene burst disappears on the order of minutes. The time required for the graphite

to disappear depends upon the cell potential. At 0.75 V, the intensity of the graphite peak diminishes significantly after 2 min, although measurable intensity still exists after 4 min. (Figure VI.5, middle panel) At 0.45 V, the graphite formed from the ethylene burst disappears completely after 2 min. (Figure VI.5, right panel) Oxidation rates of carbon deposits formed on Ni/YSZ cermet anodes from bursts of butane showed a similar dependence on cell potential.[30]

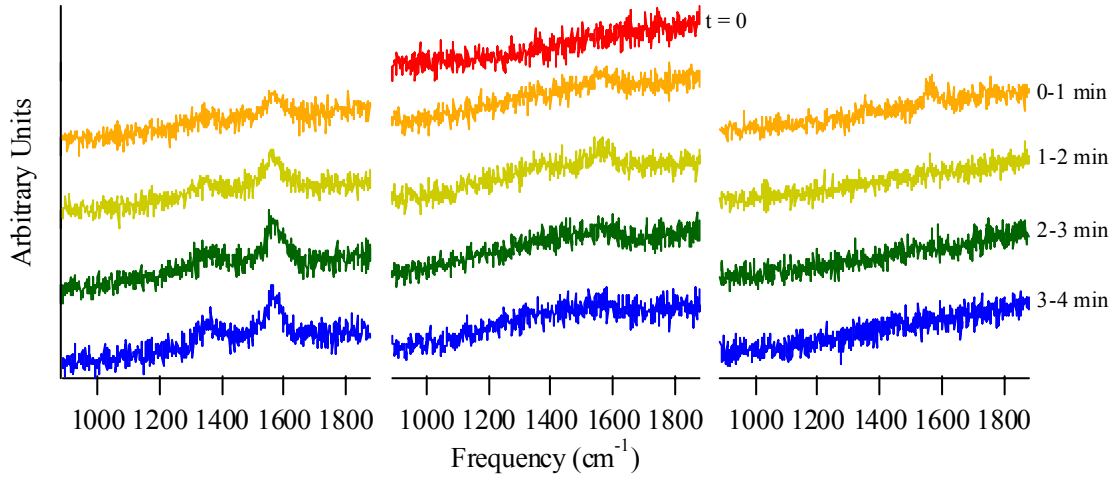

Figure VI.6. Raman spectra acquired from a Ni/YSZ porous anode operating at 1.10 V (OCV) (left), 0.80 V (center), and 0.50 V (right). The top, featureless trace results from a clean, reduced Ni/YSZ anode. When the cell voltage is 0.50 V, the G mode of graphite at 1585 cm^{-1} appears 1 min after exposure to 5 cc propylene. (second row from top) After 2 min the graphite disappears. (third row from top) At a cell voltage of 0.80 V both the G and D peaks form 1 min after exposure to propylene (second row from top) and are degrading, but still present after 4 min (bottom row). When the cell is operated at OCV, both the G and D peaks form and remain indefinitely. This carbon deposition is indistinguishable from that seen when butane is used as a fuel.

The final fuel tested in these studies was propylene, a hydrocarbon that constitutes ~13.0 % of the products formed by butane pyrolysis. *In-situ* Raman spectra acquired from an anode operating with H_2 and propylene bursts are displayed in Figure VI.6. Again, the top, featureless trace is of the clean anode operating with a hydrogen/argon feed. The carbon deposits that result from 5 cc of propylene are

markedly different from those of ethylene. In these spectra both the G and D (at ~1350 cm^{-1}) features appear for all cells operating at all potentials, although these features are especially strong under OCV (1.10 V) conditions. (Figure VI.6, second row) As with graphite formed from ethylene, the propylene-formed graphite persists indefinitely under OCV conditions with no measurable change in the relative intensities of the D and G Raman bands. The relatively large D band suggests that the graphite formed with propylene is very similar to that formed with butane. This tendency is addressed in detail below.

As expected, the graphite is transient at the lower cell potentials of 0.80 V and 0.50 V. At 0.80 V, the intensity of the graphite peak diminishes considerably after 4 min. (Figure VI.6, middle panel) At 0.50 V, the graphite peaks disappears completely after 2 min. (Figure VI.6, right panel) At the lowest cell potential tested (corresponding to the highest oxide flux) the D band intensity diminishes faster than the G band intensity, suggesting defects in the graphite structure are the most reactive sites on the deposits and are most susceptible to oxidation.

Several important conclusions can be drawn from Figures 2-5. First, methane may be one of the primary pyrolysis products of higher weight hydrocarbons, but it is not the primary source of graphitic carbon formed on SOFC cermet anodes. Second, small hydrocarbons such as methane and ethylene show a much greater propensity to form ordered graphite as evidenced by a relatively strong feature in the *in-situ* Raman spectra at 1585 cm^{-1} and the virtual absence of intensity at ~1365 cm^{-1}. The fuel that shows a pattern of graphite formation most similar to that of butane is propylene, which represents only 13% of the products formed by butane pyrolysis.[27]

Nonetheless, Raman spectra of carbon deposited by this fuel match almost perfectly similar spectra of graphitic carbon that forms from a butane feed.

3B. Carbon Growth at OCV

The stable carbon deposits formed on SOFC anodes at OCV provide high quality Raman spectra for analysis. 200 s scan spectra of anodes after exposure to each of the three hydrocarbons are shown in Figure VI.7. The anode exposed to 5 cc of methane shows no evidence of carbon deposition, but the same amount of exposure for both ethylene and propylene produces significant graphitic carbon as indicated prominently in the OCV Raman spectra. Spectra from both ethylene and propylene show D and G features, with the spectrum of the graphite formed from propylene evincing much more disorder than the ethylene-formed graphite. The presence of both carbon peaks allows for quantitative characterization of graphite domain size using the ratio: $I_D/I_G = C_\lambda/L_a$, where I_x is the Raman peak intensity, C_λ is the Raman coupling coefficient (3.504 for 488 nm light) and L_a is the domain diameter in nm.[36,40] The resulting domain sizes from the three hydrocarbon fuels and butane are listed in Table VI.1. This analysis shows clearly that as fuels increase in molecular weight, the graphite domains become smaller, indicating an increase in disorder. Furthermore, the ethylene data indicate that the structure of the graphitic carbon domains changes with increased exposure.

Table VI.1: Domain Size of Graphite Formed with Hydrocarbon Fuels		
Fuel	I_D/I_G	Domain Size
CH4	0	N/A
C2H4	0.074	47.5 ± 7.1 nm
C3H6	0.855	4.1 ± 0.4 nm
C4H10	0.898	3.9 ± 0.4 nm

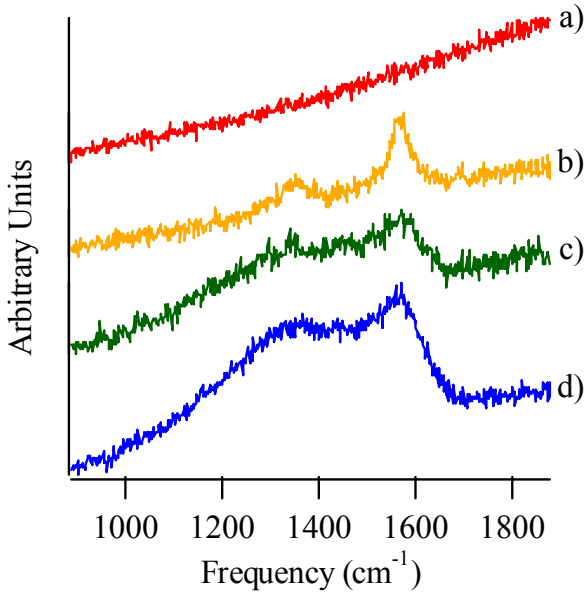

Figure VI.7. Long acquisitions (200 1 s scans) of Ni/YSZ cermet anode surfaces at OCV after exposure to 5 cc methane (a), ethylene (b), propylene (c), butane (d). The graphite formed with propylene and butane exhibits large amounts of disorder (large D peaks) indicating small domain sizes (~4 nm). The graphite formed with ethylene has a much smaller D peak and, therefore, a much larger domain size (47.5 nm).

The lack of a graphitic D band in Raman spectrum of the anode exposed to large amounts of methane indicates that the domain size of the graphite formed is large. Carbon growth likely proceeds by the addition of individual carbon atoms, thereby minimizing the number of defects incorporated into the graphite formed. Ethylene also results in graphite with a large domain size, but unlike the graphite formed by methane, the size of ethylene-formed graphite domains can be quantified due to the measurable D feature in the Raman spectrum. The more rapid growth of

graphite with ethylene likely leads to disorder due to the increased nucleation sites and faster growth kinetics. However, initial growth is still slow enough so that most carbon is integrated into thermodynamically stable, highly ordered graphitic structures having few defects and correspondingly large average domain sizes.

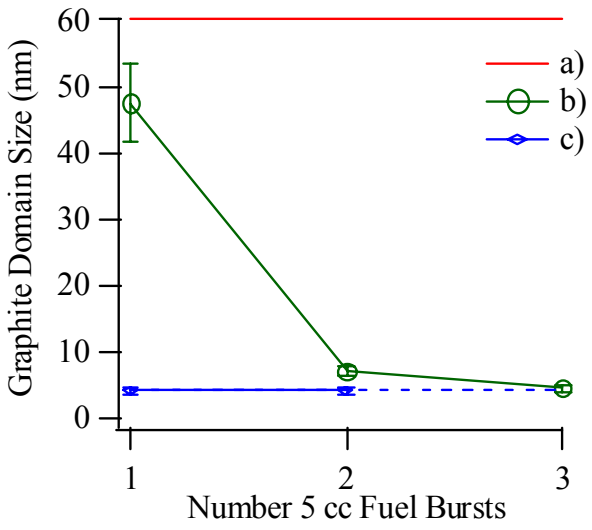

Figure VI.8. Graphite domain size with increased fuel exposure. The domain size of graphite formed with methane (a) can not be calculated from our data due to the lack of a D peak in the Raman spectrum, the line in this figure represents the fact that the graphite is highly ordered. The domain size of the graphite formed with ethylene (b) shows a dramatic decrease in domain size. In the case of propylene fuel, graphite with a 4.1 nm domain size forms immediately. A second burst of propylene results in no change in domain size. The dotted line signifies the assumption that ~4 nm is the lower limit for graphite domain size, however, the optical window is obscured after 2 bursts by carbon deposits on the quartz.

Differences in the spectra from subsequent bursts of ethylene indicate that the disorder in the graphite changes as more ethylene is added. Figure VI.8 shows the trend toward decreasing graphite domain sizes with successive bursts. The low-coordination, high energy sites of disordered graphite appear to promote additional disorder as more graphite is formed. As seen in Figure VI.5, methane forms only

highly ordered graphite. Similar experiments with ethylene, propylene and butane are not feasible in the current assembly due to excessive carbon growth that covers the cell window after just 2-3 bursts, ruining the optical transparency necessary for Raman measurements. However, repeated experiments carried out with propylene and butane show spectra of that lead to consistent I_D/I_G ratios, suggesting that ~4 nm may be the lower limit for graphite domain size on these anodes.

The additional methyl group in propylene (in reference to ethylene) has a striking effect on the carbon growth. The graphite formed from propylene is qualitatively different than that formed by ethylene and quantitatively quite similar in structure to that formed by butane. (Figure VI.6) Dominating the OCV spectrum of propylene-formed graphite is a strong, broad feature at 1365 cm^{-1} indicating that the graphite contains significant numbers of defects in the form of edges and grain boundaries.

3C. Effects of Carbon Deposits on Cell Performance

Data from cells using butane showed that graphite formation after the first 25 cc led to a 60% drop in power density, only to recover after an additional 50 cc of butane (Figure VI.9).[30] These results mirrored previous reports of improved SOFC performance with the formation of carbonaceous deposits on the anode.[28,31] One mechanism proposed to describe this effect requires that the carbon deposits be conducting and "wire together" isolated parts of the cermet anode.[28] With this model, the deposited carbon improved the current collecting ability of the anode thus improving overall performance. The diminished output of the SOFC observed in the experiments shown in Figure VI.9 might be interpreted as the initial blockage of

active sites followed by eventual expansion of the effective anode area as the conducting carbon deposits expand. An alternative proposal is that the graphite formation frees up hydrogen for electrochemical reactions and also enhances three-phase boundary interactions for a reduced polarization resistance.

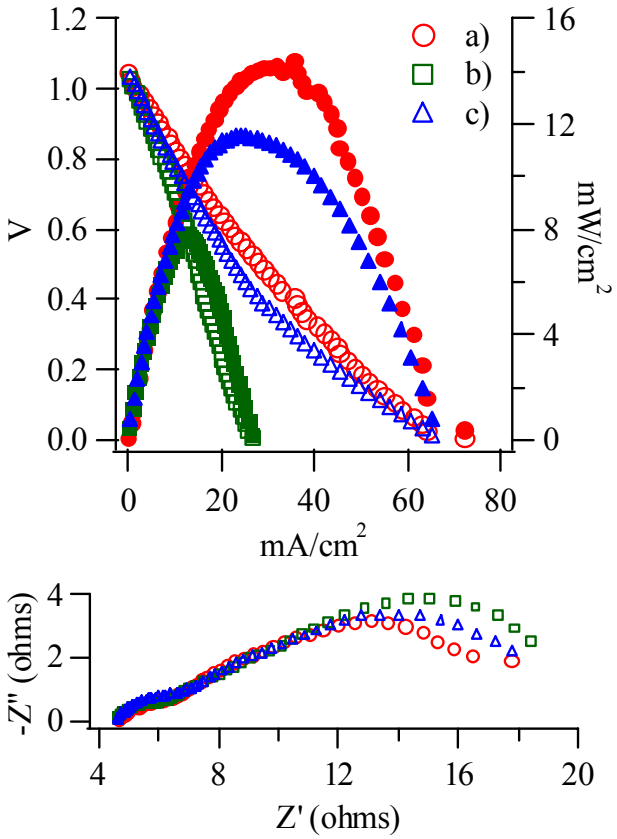

Figure VI.9. Electrochemical data acquired from cells operated with hydrogen fuel after exposure to 0 cc (a), 25 cc (b), and 75 cc (c) of butane. The top graph shows the voltammetry (open marks) and power density curves (closed marks). The bottom graph shows the electrochemical impedance data. The data show a clear drop of ~60% in cell performance after 25 cc of butane followed by a near-full recovery after 75 cc.

One goal of this study is to better understand this improved performance accompanying the creation of butane-formed graphite by examining individually the effect that each pyrolysis product hydrocarbon has on SOFC performance. These

experiments use both voltammetry and EIS to characterize SOFC performance after different amounts of exposure to the fuel of interest. During exposure the cell is kept under OCV conditions to prevent any graphite formed from simply being oxidized away in a matter of minutes. All electrochemical measurements are conducted with hydrogen as a fuel, so overall cell performance from experiment to experiment can be compared quantitatively. The important quantities obtained from these measurements include power and current densities and the polarization resistances. The impedance measurements shown in Figure VI.9 indicate that the initial drop in performance is due to an increase in the low frequency process dominating the polarization resistance. The increase in this portion of the polarization resistance suggests that over the time the surface carbon structure may facilitate electrochemical reactions thereby resulting in the recovery of the original lower polarization resistance. The mechanism for this is unknown and thus, it is valuable to employ Raman spectroscopy to explore the transient nature of the carbon deposit structures. Signs of cell degradation resulting from exposure to the hydrocarbon fuels appear as diminished current and power densities recorded in voltammetry experiments as well as increases in the polarization resistances measured in impedance spectra.

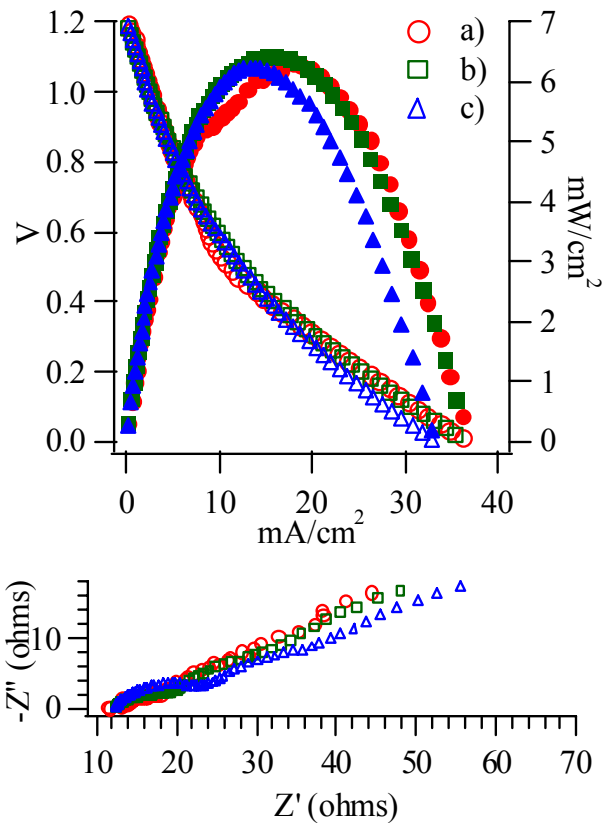

Figure VI.10. Electrochemical data acquired from cells operated with hydrogen fuel after exposure to 0 cc (a), 25 cc (b), and 75 cc (c) of methane. The top graph shows the voltammetry (open marks) and power density curves (closed marks). The bottom graph shows the electrochemical impedance data. There are only minimal variations in the data indicating that the ordered graphite formed with small amounts of methane does not affect SOFC performance.

The Raman measurements discussed in the previous section showed that small amounts of methane fuel resulted in no measurable carbon deposition, even at OCV. The electrochemical data following anode exposure to 25 and 75 cc of methane exposure are shown in Figure VI.10. As expected, small quantities of methane have minimal effect on the electrochemical performance of the cell. Maxima in both the current and power densities throughout the experiment vary by less than 5% from the initial data from the pristine cell. Impedance data show the same consistency with

number of fuel bursts. These measurements indicate strongly that methane found in the post-pyrolysis butane fuel feed is not responsible for the observed electrochemical behaviour associated with butane.

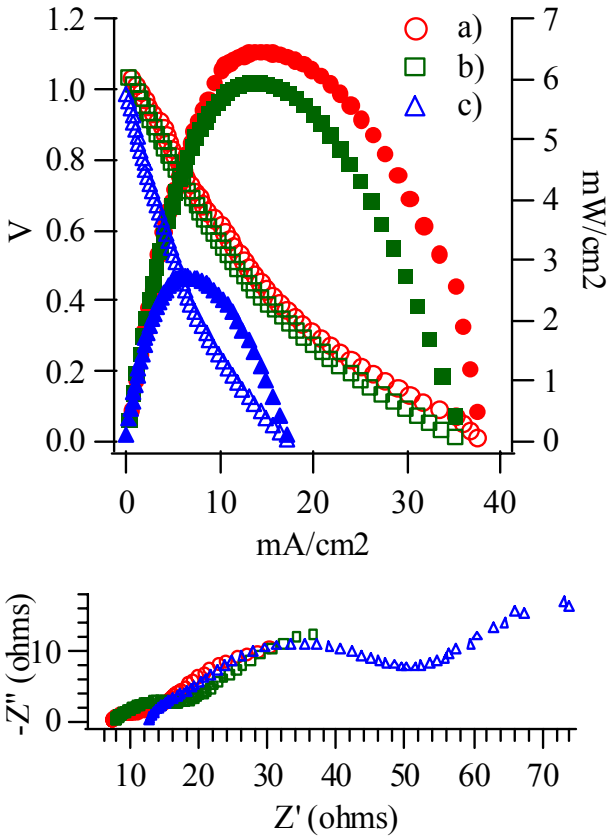

Figure VI.11. Electrochemical data acquired from cells operated with hydrogen fuel after exposure to 0 cc (a), 25 cc (b), and 75 cc (c) of ethylene. The top graph shows the voltammetry (open marks) and power density curves (closed marks). The bottom graph shows the electrochemical impedance data. Exposure of the Ni/YSZ anode to ethylene leads to measurable carbon build up and has a detrimental affect on cell performance. Cell performance, in terms of the current and power densities, is ~60% that of a clean cell.

Changes in SOFC electrochemical performance as a function of ethylene exposure are self evident in Figure VI.11. After exposure to 25 cc of ethylene, both the voltammetry and impedance data show that cell performance decreases by ~10%. This reduced performance constitutes a small change compared to the ~60%

reduction in performance when the anode sees the same amount (by volume) of butane. Given the qualitative differences in the ethylene-formed graphite vs. butane-formed graphite, this result is not surprising. Continued exposure to ethylene results in further degradation of cell performance. After 75 cc of ethylene, the voltammetry and impedance data show that the cell is operating at ~40% of its maximum performance with hydrogen compared to before the introduction of ethylene, and SOFC performance shows no sign of recovery. This behavior contrasts with observations when butane is used as a fuel. With a butane fuel feed, the drop in performance that accompanies initial exposure of the cell to the hydrocarbon fuel is followed by a recovery of the pre-exposure power and current densities. The *in-situ* Raman data and the electrochemical results indicate that the graphite formed with ethylene is fundamentally different from that formed with butane.

Spectroscopic data from anodes exposed to propylene show that this fuel leads to the same type of deposited graphite as butane. These results suggest that carbon formation in SOFCs using logistic fuels and, consequently, the SOFC performance behavior may be dominated by minority products of butane pyrolysis. However, the electrochemical data in Figure VI.12 do not support this supposition. Despite the similarities in graphite domain size, the cell operated with propylene exhibits electrochemical behavior more closely related to cells operated with ethylene. Namely, after 25 cc exposure the voltammetry and impedance data show very little decrease in cell performance, and after 75 cc the performance has decreased by 25% from the benchmark conditions defined by the pristine cell.

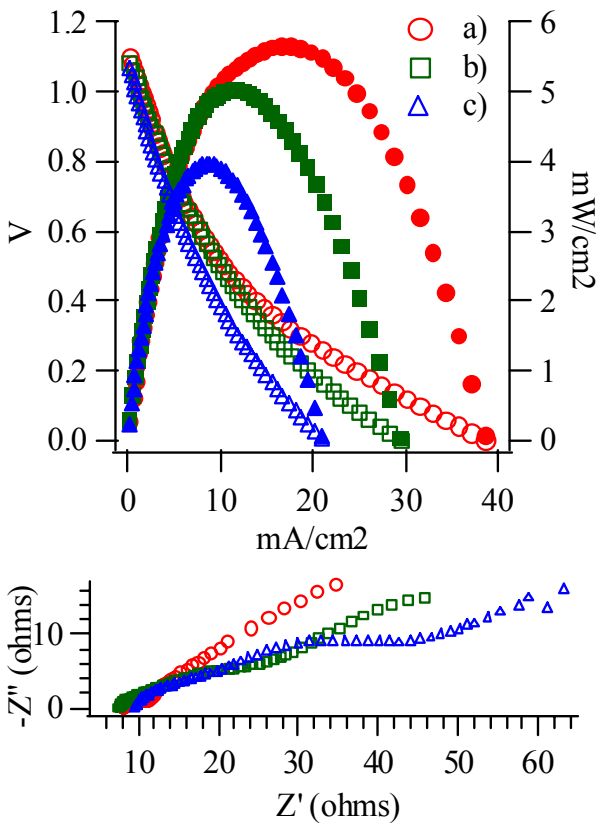

Figure VI.12. Electrochemical data acquired from cells operated with hydrogen fuel after exposure to 0 cc (a), 25 cc (b), and 75 cc (c) of propylene. The top graph shows the voltammetry (open marks) and power density curves (closed marks). The bottom graph shows the electrochemical impedance data. Exposure of the Ni/YSZ anode to propylene leads to measurable carbon build up. The graphite deposits are indistinguishable from those formed with butane, however, the performance of cell operating with propylene does not show the same recovery that is seen with butane fueled cells.

At first glance, the electrochemical data from all three fuels fail to support a mechanism whereby graphite formation on porous SOFC cermet anodes improves cell performance. This conclusion contradicts previous reports in the literature as well as results from our own studies.[16,28,30] However, one must recognize that reported butane pyrolysis product distributions (that have been adapted slightly to account for conditions relevant to the electrochemical assembly used in this work) do

not represent thermodynamically stable distributions and that the products themselves – propylene, ethylene and to a lesser extent methane – can also undergo pyrolysis.[38,41] From the SOFC assembly depicted in Figure VI.1, one can see that the fuel/carrier mix passes through the entire furnace assembly on its way to the anode chamber. This geometry means that any fuel passes through a ~10 cm region where the temperature is 1000 ˚C. Given the flow rates used in these experiments, the residence time for fuel in this region is approximately 1 s. Under these conditions, both ethylene and propylene undergo pyrolysis. Pyrolysis of ethylene is modest with a product distribution that still contains ~60% ethylene (by mole fraction of C) and ~15% hydrogen, with all other product yields below 10%.[41] Such large amounts of ethylene and hydrogen suggest that ethylene will still dominate the mechanism of graphite formation.

Pyrolysis of propylene is more complicated. At the high temperatures encountered by propylene in these experiments, the mix of products includes (by carbon mole fraction) benzene (25%), ethylene (22%), methane (16%), propylene (10%), hydrogen (10%), and trace amounts of conjugated C_2-C_4 hydrocarbons.[41] An important point to remember about the propylene-formed graphite on the SOFC anode is that a considerable amount of the material exists in a disordered state as evidenced by the very large, broad D peak in the Raman spectrum. This observation coupled with the results from smaller hydrocarbon fuels means that ethylene, methane, and hydrogen can be ruled out as primary contributors to the type of graphite formed from the propylene feed. Interestingly, one would also expect benzene – another major pyrolysis product – to form highly ordered graphite, given

that this six-membered aromatic structure is the fundamental subunit of graphene sheets. However, benzene is only a trace product of butane pyrolysis. The similarities between the graphite formed from propylene and butane pyrolysis together with the similarities and differences in their pyrolysis product distributions suggest that propylene itself may be the primary species responsible for the rapid build up of small grain graphite on the Ni/YSZ cermet anodes.

These considerations mean that simply adding representative amounts of ethylene or propylene individually will not expose the SOFC anode to the same mix of hydrocarbon fuels as if butane were used as the sole fuel. Furthermore, these observations raise the possibility that different fuels cooperate synergistically to improve overall SOFC performance, and that no one fuel individually is responsible for the effects previously observed.

Previous reports that observe improved performance of SOFCs following exposure to butane (and accompanying carbon deposition), typically operate with butane for periods of up to several hours before making benchmark measurements with H_2. Taking into account differences in experimental assemblies, the anodes used in Refs 28 & 32 are exposed to orders of magnitude more butane than are the anodes used in the "burst" experiments reported in this work. One goal of our studies is to identify species present in the early stages of carbon formation on Ni/YSZ cermet anodes. Specifically, we hope to correlate the type of graphite formed and its relative stability with the identity of the gas-phase fuel responsible for graphite growth. As a result, we intentionally keep the relative exposures limited compared to those studies using continuous carbon-containing fuel feeds.

3D. Analysis of the Mechanism of Carbon Deposition

Carbon formation on SOFC anodes is a complicated process, dependent on many variables, including fuel type, concentration, and the electrochemical potential of the cell. Reactions within the fuel feed itself will further complicate mechanistic interpretation of both the electrochemical oxidation and carbon deposition. The pyrolysis product distribution will be highly dependent on conditions from assembly to assembly, as suggested by recent studies in gas-phase pyrolysis of light hydrocarbons.[27,38,41]

Experiments using methane indicate that methane is the least reactive, in terms of carbon deposition, of the principal butane pyrolysis products. The little carbon formed on the anode surface by methane decomposition is highly ordered. The more highly ordered structure of the deposit is likely a result of the slow formation rates with pure methane feeds.

Ethylene is more reactive than methane on the anode surface due to the presence of the carbon-carbon double bond. Thus, more graphite is formed per equivalent amount (by mole) of fuel, Although initially like methane, ethylene produce rather large graphite domain sizes, as deposition continues, the domain size rapidly decreases (Figure VI.8) likely due to the autocatalytic nature of carbon deposition and the rapid carbon deposition kinetics of ethylene.

With an increase in size of the butane pyrolysis products to propylene, carbon deposition rates further increase. In fact, the relative size of the D bands in the Raman spectra in Figure VI.6 and the calculated domain sizes in Table VI.1 of graphite formed with propylene and butane are nearly identical. This observation

implies that propylene forms graphite on the surface much faster than the other butane pyrolysis products, and is likely a primary contributor to graphite formation in SOFC's fed by higher-weight logistics fuels. The considerably smaller domain size of graphite formed by propylene probably results from the asymmetry intrinsic to the molecule itself. If the carbon-carbon double bond is more labile and capable of promoting graphite formation and the methyl group is relatively unreactive thus creating a barrier to additional graphite growth, then adsorption of propylene to the Ni/YSZ surface will increase the likelihood of carbon deposition but only in an anisotropic manner. Anisotropic evolution, in turn, can create even more nucleation sites for carbon growth.

4. Conclusion

The chemistry of carbon deposition and oxidation in Ni-based SOFC anodes operated with hydrocarbon fuels is complicated due to fuel pyrolysis and requires the study of individual pyrolysis products. Results presented in this work show that the majority products of butane pyrolysis – methane, ethylene, and propylene – form a variety of carbon deposits that affect Ni/YSZ anode performance in various ways. Methane forms small amounts of highly ordered graphite that has little impact on cell performance relative to other fuels. Ethylene forms more graphite with a higher degree of disorder and, these deposits are detrimental to the anode performance. Propylene forms nanocrystalline graphite with the same domain size as butane. Unlike butane, the performance of cells operated with propylene continues to decline with continued exposure to the hydrocarbon fuel and does not recover. A complete understanding of the chemical mechanism of hydrocarbon fuel decomposition in

SOFCs requires further study. The results from this study however do show that such understanding can not be developed without careful analysis of the primary fuel decomposition products, all of which may play unique roles in the carbon deposition as well as fuel oxidation process. A more detailed mechanistic discussion appears in Chapter VIII.

5. References

(1) Alanne, K.; Saari, A.; Ugursal, V. I.; Good, J. *J. Power Sources* **2006**, *158*, 403.

(2) Calise, F.; Palombo, A.; Vanoli, L. *J. Power Sources* **2006**, *158*, 225.

(3) Fontell, E.; Phan, T.; Kivisaari, T.; Keranen, K. *J. Fuel Cell Sci. Technol.* **2006**, *3*, 242.

(4) Song, C. S. *Catal. Today* **2002**, *77*, 17.

(5) Ormerod, R. M. *Chem. Soc. Rev.* **2003**, *32*, 17.

(6) Holtappels, P.; De Haart, L. G. J.; Stimming, U.; Vinke, I. C.; Mogensen, M. *J. Appl. Electrochem.* **1999**, *29*, 561.

(7) Lin, Y.; Zhan, Z.; Liu, J.; Barnett, S. A. *Solid State Ionics* **2005**, *176*, 1827.

(8) Primdahl, S.; Mogensen, M. *J. Electrochem. Soc.* **1997**, *144*, 3409.

(9) Deluca, N. W.; Elabd, Y. A. *J. Polym. Sci. Part B-Polym. Phys.* **2006**, *44*, 2201.

(10) Litster, S.; McLean, G. *J. Power Sources* **2004**, *130*, 61.

(11) Yamaji, K.; Kishimoto, H.; Xiong, Y. P.; Horita, T.; Sakai, N.; Brito, M. E.; Yokokawa, H. *J. Power Sources* **2006**, *159*, 885.

(12) Kim, T.; Liu, G.; Boaro, M.; Lee, S. I.; Vohs, J. M.; Gorte, R. J.; Al-Madhi, O. H.; Dabbousi, B. O. *J. Power Sources* **2006**, *155*, 231.

(13) Mallon, C.; Kendall, K. *J. Power Sources* **2005**, *145*, 154.

(14) Yoon, S. P.; Han, J.; Nam, S. W.; Lim, T. H.; Hong, S. A. *J. Power Sources* **2004**, *136*, 30.

(15) Finnerty, C. M.; Coe, N. J.; Cunningham, R. H.; Ormerod, R. M. *Catal. Today* **1998**, *46*, 137.

(16) Atkinson, A.; Barnett, S.; Gorte, R. J.; Irvine, J. T. S.; McEvoy, A. J.; Mogensen, M.; Singhal, S. C.; Vohs, J. *Nature Materials* **2004**, *3*, 17.

(17) Pomfret, M. B.; Owrutsky, J. C.; Walker, R. A. *J. Phys. Chem. B* **2006**, *110*, 17305.

(18) Phillips, J.; Shiina, T.; Nemer, M.; Lester, K. *Langmuir* **2006**, *22*, 9694.

(19) Van Speybroeck, V.; Reyniers, M. F.; Marin, G. B.; Waroquier, M. *Chemphyschem* **2002**, *3*, 863.

(20) Wang, X. B.; Liu, Y. Q.; Zhu, D. B. *J. Nanosci. Nanotechnol.* **2002**, *2*, 33.

(21) Laosiripojana, N.; Assabumrungrat, S. *J. Power Sources* **2007**, *163*, 943.

(22) Chen, F. Z.; Zha, S. W.; Dong, J.; Liu, M. L. *Solid State Ionics* **2004**, *166*, 269.

(23) Zhu, H. Y.; Colclasure, A. M.; Kee, R. J.; Lin, Y. B.; Barnett, S. A. *J. Power Sources* **2006**, *161*, 413.

(24) Lin, Y. B.; Zhan, Z. L.; Barnett, S. A. *J. Power Sources* **2006**, *158*, 1313.

(25) Haberman, B. A.; Young, J. B. *J. Fuel Cell Sci. Technol.* **2006**, *3*, 312.

(26) Hecht, E. S.; Gupta, G. K.; Zhu, H. Y.; Dean, A. M.; Kee, R. J.; Maier, L.; Deutschmann, O. *Appl. Catal. A-General* **2005**, *295*, 40.

(27) Sheng, C. Y.; Dean, A. M. *J. Phys. Chem. A* **2004**, *108*, 3772.

(28) McIntosh, S.; Vohs, J. M.; Gorte, R. J. *J. Electrochem. Soc.* **2003**, *150*, A470.

(29) Dong, J.; Cheng, Z.; Zha, S. W.; Liu, M. L. *J. Power Sources* **2006**, *156*, 461.

(30) Pomfret, M. B.; Owrutsky, J. C.; Walker, R. A. *Anal. Chem.* **2007**, *79*, 2367.

(31) McIntosh, S.; He, H.; Lee, S.-I.; Costa-Nunes, O.; Krishnan, V.; Vohs, J. M.; Gorte, R. J. *J. Electrochem. Soc.* **2004**, *151*, A604.

(32) Demircan, O.; Sukeshini, M.; Pomfret, M. B.; Jackson, G. S.; Walker, R. A.; Eichhorn, B. W. "Formation of Carbon Deposits from Hydrocarbon Fuels in SOFC: Towards a Mechanistic Understanding"; 205th Meeting of The Electrochemical Society, 2004, San Antonio, TX.

(33) Demircan, O.; Pomfret, M. B.; Walker, R. A.; Eichhorn, B. W. **in preparation**.

(34) Costa-Nunes, O.; Gorte, R. J.; Vohs, J. M. *J. Power Sources* **2005**, *141*, 241.

(35) Sukeshini, A. M.; Habibzadeh, B.; Becker, B. P.; Stoltz, C. A.; Eichhorn, B. W.; Jackson, G. S. *J. Electrochem. Soc.* **2006**, *153*, A705.

(36) Ferrari, A. C.; Robertson, J. *Phys. Rev. B* **2000**, *61*, 14095.

(37) Kakihana, M.; Osada, M. Raman Spectroscopy as a Characterization Tool for Carbon Materials. In *Carbon Alloys: Novel Concepts to Develop Carbon*

Science and Technology; Yasuda, E., Inagaki, M., Kaneko, M., Endo, M., Oya, A., Tanabe, Y., Eds.; Elsevier Science, Ltd.: Oxford, UK, 2003; pp 285.

(38) Mathieu, D. M.; Dean, A. M.; Grenda, J. M.; Green, J. W. H. *J. Phys. Chem. A* **2003**, *107*, 8552.

(39) Pomfret, M. B.; Demircan, O.; Sukeshini, A. M.; Walker, R. A. *Environ. Sci. Technol.* **2006**, *40*, 5574.

(40) Matthews, M. J.; Pimenta, M. A.; Dresselhaus, G.; Dresselhaus, M. S.; Endo, M. *Phys. Rev. B* **1999**, *59*, R6585.

(41) Norinaga, K.; Deutschmann, O.; Huttinger, K. J. *Carbon* **2006**, *44*, 1790.

Chapter 7: A Mechanistic Understanding of Solid Oxide Fuel Cell Chemistry through *In-Situ* Raman Spectroscopy

1. Introduction

Solid oxide fuel cells (SOFCs) are integral alternative power sources for a proposed hydrogen economy. The popularity of SOFCs is due to the ability of the cells to efficiently convert a wide range of fuels – including hydrogen, carbon monoxide, and hydrocarbons – to electricity and clean products.[1,2] While other systems, such as polymer electrolyte fuel cells, are limited to using only hydrogen fuel, SOFCs have proven to be more durable.[3-8] However, deposits from carbon-containing fuels complicate fuel oxidation chemistry and can lead to cell breakdown.[9] This chapter presents work in which a newly developed *in-situ* Raman spectroscopy technique has been used to gain a molecularly specific understanding of hydrocarbon fuel chemistry previously unattainable.

Various anode and electrolyte materials are currently being investigated to increase the carbon tolerance of SOFCs.[10-16] Most studies use electrochemical methods of characterizing cell performance.[17-20] While vital to understanding cell performance, these techniques lack the molecular specificity that is necessary to understanding the oxidation mechanism of fuel on the anode side of the cell. The absence of molecule-level information about carbon-containing fuels hampers the development of quantitative models that are capable of predicting carbon deposition and fuel oxidation pathways.

Recently, optical spectroscopy has been used to identify molecular intermediates on both cathodes and anodes in operating SOFCs.[6,21] Specifically, Raman spectroscopy has been used *in-situ* to characterize carbon deposits and partially oxidized intermediates on Ni/YSZ cermet anodes with various carbon-containing fuels. Butane has been used as a model high-weight hydrocarbon and has been shown to rapidly deposit disordered graphite on the anode surface. Simultaneous electrochemical measurements characterized cell performance during the early-time butane flow, showing that graphite deposits resulting from butane initially degrade cell performance and further butane exposure leads to a partial recovery.[6] The mechanism of this behavior is complicated because butane pyrolyzes at SOFC operating temperatures. At 700 °C, the post pyrolysis flow consists of 39.8% ethylene, 36.3% methane, 13.0% propylene, 5.6% ethane, 4.3% butane, and a balance of other small hydrocarbons.[22] Methane, ethylene and propylene have been studied in an attempt to understand the high-weight hydrocarbon mechanism. While propylene fuel forms graphite deposits that are indistinguishable from those formed with butane, none of the small hydrocarbons duplicated the butane cell performance trend when used as singular fuels.[23]

The result of the study of SOFCs operated with hydrocarbon mixtures that mimic the stoichiometry of the post-pyrolysis butane flow are presented below. Methane/ethylene (1:1), methane/propylene (4:1), and ethylene/propylene (4:1) are used in an attempt to understand the cell performance trend that is evident with butane fuel. It has been found that the combination of ethylene and propylene leads to similar cell performance recovery indicating that while propylene is responsible for

the type of graphite that is formed, the cell performance recovers only when ethylene and propylene are used in concert.

2. Experimental

2A. Fuel Cell Construction

The SOFCs used in this study are constructed as described in previous work. Electrolytes are dense YSZ – 8 mole % yttria – with a thickness of 0.8 mm. The porous anodes are made using Ni/YSZ paste (50% Ni, 50% YSZ by weight, post-reduction) acquired from NexTech Materials (Lot # 112-45). Porous cathodes were made from a LSM/YSZ (50% $La_{0.85}Sr_{0.15}MnO_3$ and 50% YSZ by weight) paste made in-house. Both electrodes are ~20 μm thick.

The cells are attached anode-side-out to an alumina tube assembly with zirconia paste. A quartz tube, closed on one end, encased the alumina-supported rig. The cathode and anode chambers were sealed with tapered, silicone rubber plugs (McMaster-Carr). A split-tube furnace (ThermCraft) was fitted around the upper two-thirds of the assembly while the bottom was cooled by water and compressed air to preserve seals.

2B. Gas Flows

Fuel flows must be regulated to keep the window clean while a constant cell polarization is applied. A constant argon/hydrogen feed is flowed (150 sccm Ar, 30 sccm hydrogen) to allow for agreement with previous work. Hydrocarbon fuel mixtures are then "burst" for 10 s on top of the base flow. The bursts of each fuel mixture are as follows: 4 cc methane, 4 cc ethylene; 4 cc methane, 1 cc propylene;

and 4 cc ethylene, 1 cc propylene. This technique allows for the investigation of the effects of cell exposure to hydrocarbons prior to excessive carbon deposition that can block the optical window. For electrochemical data collection, the anode-side flow is 150 sccm Ar, 100 sccm hydrogen. 90 sccm of Air is flowed over the cathode. Rotameters (Omega) regulated flow rates with precisions of ± 1 sccm and all experiments described in this work use "dry" fuel gases.

2C. Electrochemical Operation and Data Collection

Cell polarization and electrochemical measurements were controlled by Gamry Instruments PCI4 Potentiostat/Galvanostat/ZRA. The growth of carbon deposits required that cells be kept at OCV while the cells were exposed to hydrocarbon fuels. Voltammetry measurements were made after every 10 s exposure. Linear voltammetry sweeps were conducted between OCV and 0.00 V cell potential with a scan rate of 10 mV/s and a step size of 20 mV. The IR loss attributed to the electrolyte is subtracted from each V-I plot.

2D. Raman Measurements

Raman spectra were obtained with a Renishaw In-Via Raman microscope using a custom-built optical accessory that allowed the microscope objective to be lowered into the furnace to focus the incident beam on the anode surface. The objective is cooled by a constant flow of compressed air. Samples were irradiated with the 488 nm output of an Ar^+ ion laser (25 mW) focused to a 1 μm-sized spot. For each fuel mixture, Raman spectra of the anode surface were acquired immediately before exposure to the hydrocarbon (30 1 s scans), and every minute for the first 4 minutes after exposure (30 1 s scans for each).

3. Results and Discussion

3A. Anodic Carbon Deposition

Hydrocarbon fuel mixtures are introduced to the anode chamber while the cell is at open circuit voltage (OCV) as indicated in the Methods section, following the "burst" procedure described in earlier work.[6] In this case each burst contains twice the amount – by mole – of each small hydrocarbon fuel as in the butane post-pyrolysis flow. Specifically, methane/ethylene bursts are 4 cc methane and 4 cc ethylene, methane/propylene bursts are 4 cc methane and 1 cc propylene, and ethylene/propylene bursts are 4 cc ethylene and 1 cc propylene. This procedural difference is due to the fact that the flows are operating near the low-flow limit of the rotameters. Therefore one mixed-fuel burst should be compared to two butane bursts.

Figure VII.1 presents the Raman spectra (30 s scans) of the SOFC anode surface after one burst of each fuel mixture. All spectra display peaks at 1570 cm^{-1} and 1345 cm^{-1}, which are assigned to the graphite G and D peaks, respectively. The D peak intensity is indicative of the amount of disorder in the structure of the graphite on the surface. The general trend of increasing disorder with heavier fuel mixtures is evident in the spectra. This is not surprising when one considers that the same trend holds for each hydrocarbon when used as a singular fuel. A quantitative comparison is possible when both carbon peaks are present using the equation: $I_D/I_G = C_\lambda/L_a$, where I_x is the Raman peak intensity, C_λ is the Raman coupling coefficient (3.504 for 488 nm light) and L_a is the domain diameter in nm. The resulting domain sizes are

4.7±1.0 nm for the methane/ethylene mix, 4.1±1.0 nm for the methane/propylene mix, and 2.4±1.0 nm for the ethylene/propylene mixture.

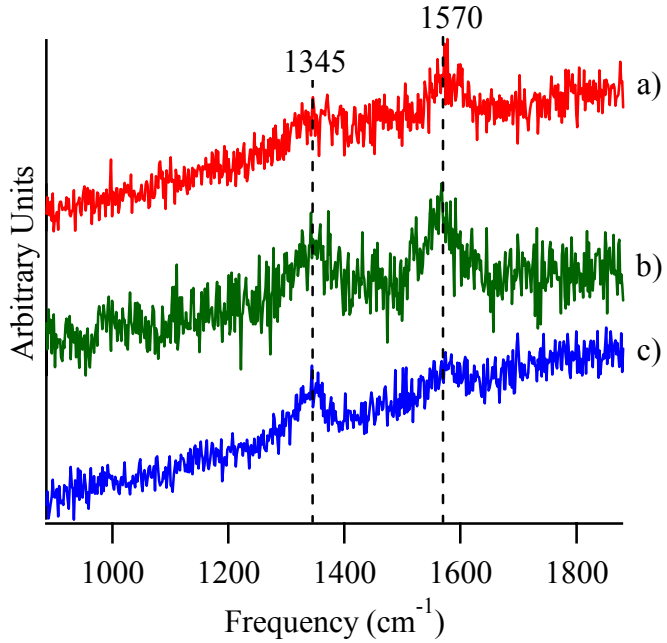

Figure VII.1. Raman spectra of graphite formed after exposing the anode to 5 cc of (a) methane/ethylene, (b) methane/propylene, and (c) ethylene/propylene fuel mixtures.

The trend toward small average domain sizes with increasing average fuel size agrees with results from earlier studies. However, all three mixtures result in average graphite domain sizes that are within experimental error of those formed with butane. One interesting discrepancy between the single fuel flows and the methane fuel mixture flows is that the single mixed burst of methane and ethylene results in graphite that is much more disordered than the graphite formed by ethylene alone. The average domain size more closely matches that of two ethylene bursts after which the D peak intensity, and therefore the disorder in the graphite, increases.[23] One explanation for this is that the mixed burst contains 60% more fuel by volume than the single fuel study. This suggests that methane alone forms ordered graphite,

but when in the presence of ethylene, methane contributes to the ethylene deposition mechanism. It is not clear if methane contributes similarly to propylene carbon deposition. The average graphite domain sizes for the deposits formed by a single burst of the methane/propylene mixture, a single propylene burst, and two propylene bursts are all within statistical error of each other – approximately 4 nm. The ethylene/propylene mixture deposits graphite with an average domain size that is lower than that of butane, but it falls within statistical uncertainty.

3B. Carbon Deposition Mechanism and Cell Performance

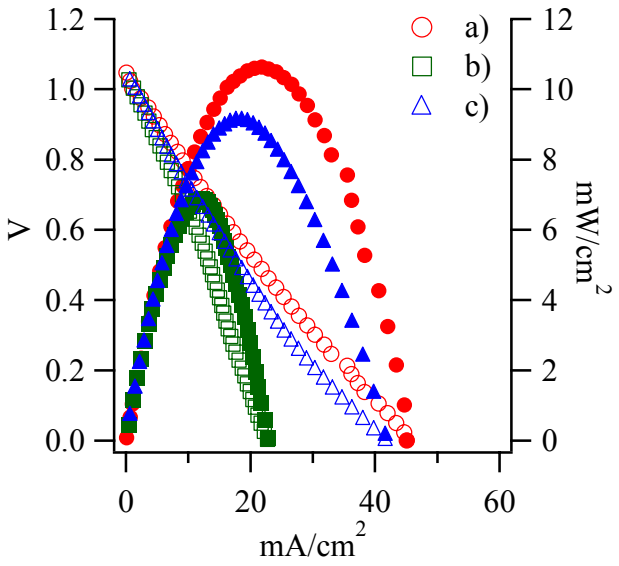

Figure VII.2. Voltammetry (open marks) and power density (closed marks) data from a SOFC at OCV before C_4H_{10} (a) exposure and after the 5th (b) and 15th bursts (c) of butane corresponding to 25 and 75 cc exposure, respectively.

Previous work has shown that exposing SOFC anodes to butane leads to increased cell performance. In cells at OCV with Ni/YSZ cermet anodes voltammetry measurements of early-time butane exposure show that the maximum current and power densities both drop after 25 cc of butane is flowed, followed by a partial performance recovery after 75 cc. This trend is demonstrated in Figure VII.2.

The mixtures of smaller fuels are studied in an attempt to assign this trend to one pair of post-pyrolysis flow components.

The electrochemical data from the cell operated with the methane/ethylene fuel mixture is shown in Figure VII.3. After two bursts – equivalent to the amount of methane and ethylene in four butane bursts – the performance increases by ~20% from that of the clean cell. It should be noted that the data in Figure VII.3 are from a cell that had anomalously low initial performance. The typical initial power density for the cells in this study is ~9 mW/cm^2. However, after eight bursts – equivalent to the amount of methane and ethylene in 16 butane bursts – the maximum current and power densities have dropped to ~85% of those exhibited by the cell prior to hydrocarbon exposure. A trend toward worsening performance continues as more fuel is added. The maximum current and power densities for up to 15 fuel bursts is shown in Figure VII.4. The performance of the cell continues to gradually degrade through burst 15. Much like the cells run on methane and ethylene as singular fuels, this behavior contrasts with that of cells run on butane. It is clear that there is no enhancement as more fuel is added and methane and ethylene, both as singular fuels or in tandem, are not responsible for the performance recovery.

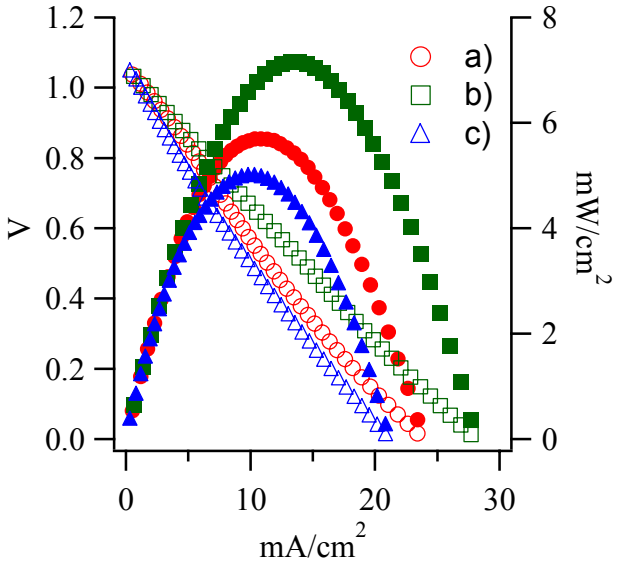

Figure VII.3. Voltammetry (open marks) and power density (closed marks) data from a SOFC at OCV before exposure (a) and after the 2nd (b) and 8th bursts (c) of the methane/ethylene fuel mixture.

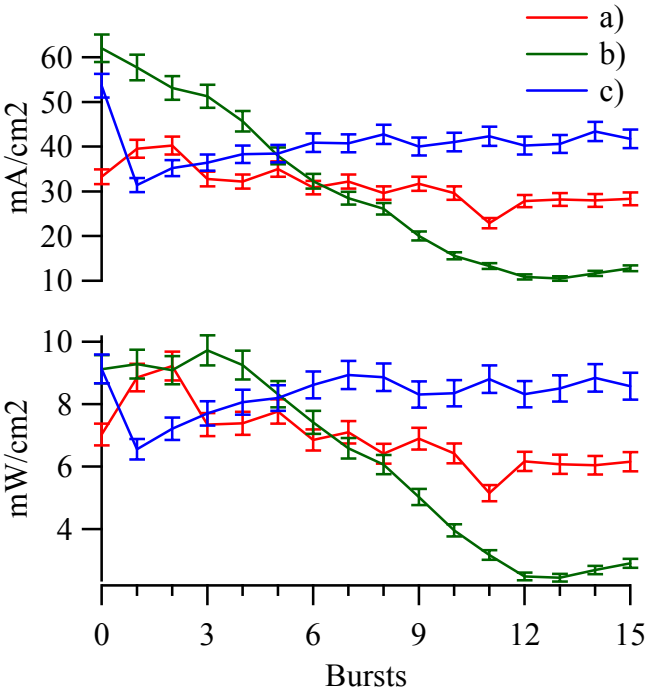

Figure VII.4. The maximum current densities (top) and power densities (bottom) after each burst of the (a) methane/ethylene, (b) methane/propylene, and (c) ethylene propylene fuel mixtures.

Figure VII.5 shows the voltage and power density plots for the methane/propylene fuel mixture. After two bursts the maximum current density

decreases from the clean cell by ~15% while the maximum power density increases by ~15%. As more fuel is added the performance begins to drop significantly. After 8 bursts the maximum current density is only ~50% of that of the clean cell, while the maximum power density drops ~20% with the same amount of fuel exposure. Figure VII.4 shows that cell performance continues to degrade. Compared to the methane/ethylene mixture, concurrent exposure of methane and propylene results in a more dramatic drop in performance. The power and current densities reach a minimum at the thirteenth burst, which theoretically corresponds to the amount of methane and propylene in 26 butane bursts. Again, it is clear that this behavior does not replicate that of cells run on butane. Like methane and ethylene, this combination of butane post-pyrolysis products is not responsible for the butane performance trend.

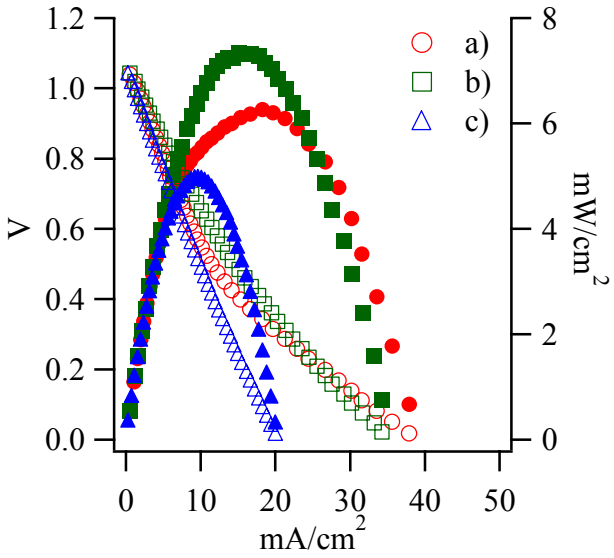

Figure VII.5. Voltammetry (open marks) and power density (closed marks) data from a SOFC at OCV before exposure (a) and after the 2nd (b) and 8th bursts (c) of the methane/propylene fuel mixture.

Voltage and power density plots from a cell exposed to the ethylene/propylene mixture at OCV are shown in Figure VII.6. Dramatic decreases in both the maximum current and power densities are apparent after two bursts. Compared to the cell prior

to hydrocarbon exposure the maximum current density has dropped ~20%, while the maximum power density is ~75% of the pristine cell. Unlike the other two fuel mixtures, the performance recovers as the anode is exposed to more hydrocarbon fuel. After 8 bursts the maximum current density climbs to 85% of that of the clean cell and the maximum power density recovers fully. The data from further ethylene/propylene exposure show that the recovery seems to plateau after seven bursts. This number of bursts corresponds to the amount of ethylene and propylene expected to be present in 14 bursts of butane fuel. The cell operated with butane showed a more dramatic initial decrease, while the recovery is more complete with the ethylene/propylene mimic mixture. However, the overall trends in both cases are extraordinarily close matches.

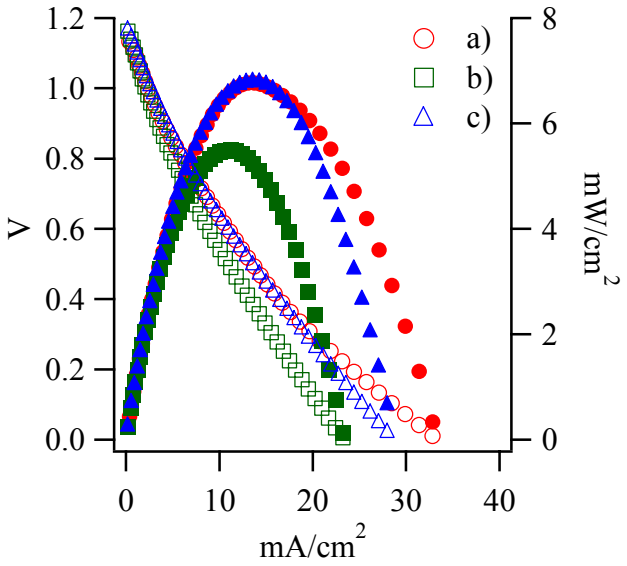

Figure VII.6. Voltammetry (open marks) and power density (closed marks) data from a SOFC at OCV before exposure (a) and after the 2nd (b) and 8th bursts (c) of the methane/propylene fuel mixture.

Previous studies have revealed that methane is relatively inactive compared to ethylene and propylene, especially for carbon deposition. While methane does form ordered graphite after a few minutes of continuous flow, no detectable amount of

carbon is formed after a single 5 cc burst. Successive bursts of methane have been shown to lead to little change in cell performance. The mixed fuel experiments show that methane is still nearly inactive in the presence of other fuels. The cell performance trends are unchanged as both methane mixtures lead to decreased current and power densities. This behavior is the same that is seen when ethylene and propylene are used as singular fuels.

Both ethylene and propylene are more reactive on the anode surface due to the presence of the carbon-carbon double bond, which is more reactive than the C-H bonds of methane. Therefore, it stands to reason that these two components would be the active ingredients in the butane post-pyrolysis fuel flow. Despite the fact that neither fuel alone reproduces the butane electrochemical trend, this study shows clearly that the combination of both fuels introduced simultaneously into the anode chamber does lead to cell performance recovery. Much like the butane case, propylene carbon formation appears to dominate carbon formation as the average domain size is smaller than both the ethylene and methane/ethylene cases. This is attributed to the presence of both carbon-carbon double bonds and methyl groups in the fuel molecules. The double bonds promote surface reactions leading to graphite formation while the methyl group is relatively inactive and likely to act as a terminal group leading to disorder in the graphite structure. This combination results in the anisotropic deposition of carbon on the anode surface.

Although the average domain sizes of deposits formed by butane and all fuel mixtures are within experimental error, the graphite deposits formed with butane and the ethylene/propylene mixture have the smallest domain size. Literature reports that

the conductivity of graphite is increased when the graphite structure becomes disordered.[24] The results show that the ethylene/propylene fuel mixture and butane alone form enough deposits to create a graphite network on the anode and that the graphite that forms the network exhibits adequate disorder to make the carbon layer electrically conductive over a sufficient area. Such a conductive, graphitic network would act as a current collector and anodic active sites once blocked by the deposits would regain activity when connected.

4. Conclusion

The chemical mechanism of electrochemical hydrocarbon fuel oxidation in SOFCs is complicated by carbon deposition that results in graphite formation on the anode. When heavier fuels, such as butane, are used fuel pyrolysis must be accounted for when considering the mechanism. Results presented in this work show that the electrochemical behavior that results when butane is used as a fuel is duplicated by a stoichiometric fuel mixture of ethylene and propylene. Methane has little effect when mixed with other components of the butane post-pyrolysis flow. Therefore, it can be concluded that methane contributes minimally to the chemical mechanism of fuel breakdown and oxidation in SOFCs operated with high-weight hydrocarbons. The type of graphite formed with butane, in terms of the average domain size of the deposits, can be duplicated with propylene alone, continued ethylene exposure, or any combination of post-pyrolysis products. However, the recovery of the current and power densities is only duplicated when the fuel flow contains ethylene and propylene. The recovery is reasoned to be the result of continued carbon deposition that leads to a conductive, graphitic network across the anode with sufficient disorder

to act as a current collector. Continuing work will focus the on the electrochemical oxidation mechanism of various fuels on SOFCs operated with various anode materials. A more detailed mechanistic discussion appears in Chapter VIII.

5. References

(1) Song, C. S. *Catal. Today* **2002**, *77*, 17.

(2) Zhu, W. Z.; Deevi, S. C. *Mater. Sci. Eng.* **2003**, *A362*, 228.

(3) Deluca, N. W.; Elabd, Y. A. *J. Polymer Science Part B-Polymer Physics* **2006**, *44*, 2201.

(4) Litster, S.; McLean, G. *J. Power Sources* **2004**, *130*, 61.

(5) Liu, J. *Prog. Chem.* **2006**, *18*, 1026.

(6) Pomfret, M. B.; Owrutsky, J. C.; Walker, R. A. *Anal. Chem.* **2007**, *79*, 2367.

(7) Ye, X. F.; Huang, B.; Wang, S. R.; Wang, Z. R.; Xiong, L.; Wen, T. L. *J. Power Sources* **2007**, *164*, 203.

(8) Zhan, Z. L.; Barnett, S. A. *Science* **2005**, *308*, 844.

(9) Atkinson, A.; Barnett, S.; Gorte, R. J.; Irvine, J. T. S.; McEvoy, A. J.; Mogensen, M.; Singhal, S. C.; Vohs, J. *Nature Materials* **2004**, *3*, 17.

(10) Ishihara, T.; Yan, J. W.; Shinagawa, M.; Matsumoto, H. *Electrochim. Acta* **2006**, *52*, 1645.

(11) McIntosh, S.; Vohs, J. M.; Gorte, R. J. *J. Electrochem. Soc.* **2003**, *150*, A470.

(12) Nesaraj, A. S.; Kumar, M.; Raj, I. A.; Radhakrishna, I.; Pattabiraman, R. *J. Iranian Chem. Soc.* **2007**, *4*, 89.

(13) Rupp, J. L. M.; Drobek, T.; Rossi, A.; Gauckler, L. J. *Chem. Mater.* **2007**, *19*, 1134.

(14) Shao, Z. P.; Haile, S. M.; Ahn, J.; Ronney, P. D.; Zhan, Z. L.; Barnett, S. A. *Nature* **2005**, *435*, 795.

(15) Wang, C.; Xui, L. H.; Tang, W. H. *Rare Metal Mater. Eng.* **2006**, *35*, 501.

(16) Zhang, X.; Robertson, M.; Deces-Petit, C.; Qu, W.; Kesler, O.; Maric, R.; Ghosh, D. *J. Power Sources* **2007**, *164*, 668.

(17) Bebelis, S.; Neophytides, S. *Solid State Ionics* **2002**, *152-153*, 447.

(18) Bieberle, A.; Gauckler, L. J. *Solid State Ionics* **2002**, *146*, 23.

(19) Bieberle, A.; Meier, L. P.; Gauckler, L. J. *J. Electrochem. Soc.* **2001**, *148*, A646.

(20) Sunde, S. *Electrochim. Acta* **1997**, *42*, 2637.

(21) Lu, X. Y.; Faguy, P. W.; Liu, M. L. *J. Electrochem. Soc.* **2002**, *149*, A1293.

(22) Sheng, C. Y.; Dean, A. M. "Comparison of Experimental Results to Model Predictions for n-Butane Pyrolysis Under High-Temperature Fuel Cell Conditions"; Third Joint Meeting of the U.S. Sections of the Combustion Institute, 2003, Chicago, IL.

(23) Pomfret, M. B.; Demircan, O.; Jackson, G. S.; Eichhorn, B. W.; Walker, R. A. *J. Electrochem. Soc.* **submitted**.

(24) Peres, N. M. R.; Guinea, F.; Castro Neto, A. H. *Phys. Rev. B* **2006**, *73*, 125411.

Chapter 8: Conclusions and Future Directions

1. Conclusions

Research described in this thesis has examined the electrochemical utilization and oxidation of carbon-containing fuels on the anode side of solid oxide fuel cells (SOFCs). A novel *in-situ* Raman technique has been developed to probe SOFC surfaces at an operating temperature of 715 °C. The successful implementation of this technique has allowed for the first, direct identification of relevant chemical species formed on cell anodes. The characterization of fuel oxidation intermediates, combined with the characterization of cell materials and quantitative exhaust studies, has provided unprecedented insight into the chemical mechanism of fuel processes in SOFCs.

1A. Material Characterization

Examination of the structural and compositional properties of YSZ shows that the Raman spectra of the material can be correlated to YSZ lattice parameter over a range of both Y_2O_3 dopant levels and temperatures. Additionally, exposing polycrystalline YSZ samples to a reducing environment at high temperatures leads to a chemical reduction of both the yttrium and zirconium to a lower valence at the surface. These findings have implications in fuel cell research where structure and composition of electrolytes may affect electrochemical operation. Furthermore, electrochemical impedance studies of YSZ surfaces show that the surface of the polycrystalline electrolytes can be reduced under OCV conditions to the point that

they have resistivities on the order of 10^{-4} Ω·cm. Polycrystalline surfaces exhibit reversible behavior; these surfaces are electrically insulating so long as the SOFC is operating at low enough cell potentials. The surface is found to be competitively resistive with a fuel cell circuit within 1-10 microns of the Ni/YSZ anode. Despite this finding, *in-situ* studies of the electrolyte found that the no carbon deposits formed on the electrolyte surface.

1B. Identification of Exhaust Components

IR absorbance data from SOFCs operating with CH_4 is a relatively poor fuel that leads to minimal electrochemical oxidation. In fact most of the CH_4 appears in the exhaust as unreacted fuel. CH_4 and C_2H_4 are both identified as gas phase products in SOFC anode exhaust. Interestingly, we see appreciable amounts of CH_4 in the exhaust from a $C_4H_{10(g)}$/Ni/YSZ system but virtually no C_2H_4, implying that ethylene is necessary to grow the graphitic deposits observed on anodes post-operation. Carbon deposition does not appear to inhibit fuel oxidation, however, as these systems produce ~4-5 times more CO and twice as much CO_2 than similar SOFCs operated with CH_4. SOFCs operating with Cu/CeO_2 anodes and a butane fuel feed show both CH_4 and C_2H_4 in their exhaust and no extensive carbon deposition. An examination of the P_{CO_2}/P_{CO} ratio for each of the three cases results in a quantitative conclusion about fuel conversion efficiency where by Cu/CeO_2 is considered to be a poorer electrocatalyst and less active in its ability to catalyze carbon deposition, but the fuel that does oxidize on the Cu/CeO_2 anode does so more efficiently given the larger P_{CO_2}/P_{CO} ratio.

1C. Characterization of Fuel Reactions on Ni/YSZ Cermet Anodes with *In-situ* Raman Spectroscopy

In-situ Raman measurements of chemical intermediates present on operating SOFC anodes show that all carbon containing fuels form intermediates, but each fuel is unique in the species that are formed. At moderate cell potentials ordered graphite and Ni-COO intermediates form, however, these species are not evident at higher or lower cell potentials. Butane forms ordered graphite at low cell potentials, but only transiently. At OCV, permanent disordered graphite deposits form on the anode following exposure to butane. Given, that butane is known to pyrolyze, a full understanding of high-weight fuel oxidation required the study of pyrolysis products as fuels. The majority products of butane pyrolysis – methane, ethylene, and propylene – each form distinct carbon deposits. An investigation of the products as singular fuels determined that the amount of disorder in the graphite deposits increases with fuel weight. Using mixtures of the small fuels always leads to graphite deposits that are indistinguishable from those formed with butane. These studies identified propylene as pyrolysis species most responsible for carbon deposition in cells using higher-weight fuels.

1D. Electrochemical Impact of Carbon Deposits

Voltammetry studies show that the formation of graphite with butane at OCV leads first to decreased cell performance after 25 cc butane, then recovered performance after 75 cc. This behavior is not observed when the lower-weight hydrocarbons are used as singular fuels. These deposits negatively impact cell performance and additional fuel exposure does not lead to recovered performance.

The cell performance trend seen in the butane studies was duplicated when C_2H_4 and C_3H_6 were used in a mixed-fuel flow, demonstrating that the trend is due to the mixture of small hydrocarbons, not one singular pyrolysis product.

2. Discussion of the Fuel Utilization Mechanism

Data presented in this thesis, combined with work done by collaborating groups at the Colorado School of Mines (CSM),[1-5] has led to unprecedented insight into hydrocarbon fuel utilization mechanisms in SOFCs. The exhaust and *in-situ* Raman studies presented in Chapters IV-VII have identified two fuel reactions: surface catalyzed carbon deposition and electrochemical carbon oxidation. The Dean group at (CSM) has studied extensively fuel pyrolysis.[1-3] The reaction pathway of butane – from the fuel tank to the exhaust, based on the results of these studies – is presented below.

The first phase of fuel utilization occurs in the fuel feed inlet, upstream from the anode catalyst. At SOFC operating temperatures high molecular weight hydrocarbons, such as butane undergo pyrolysis. At the time of this thesis, pyrolysis studies had not been done with the exact conditions of our cells. The numbers referred to in this discussion are a best approximation based on the most similar studies in literature.[3] The differing conditions and potentially differing post-pyrolysis flows may make a difference in the composition of pyrolysis products that reach the anode. For this discussion, we assume that butane pyrolyzes according to the scheme in Figure VIII.1.

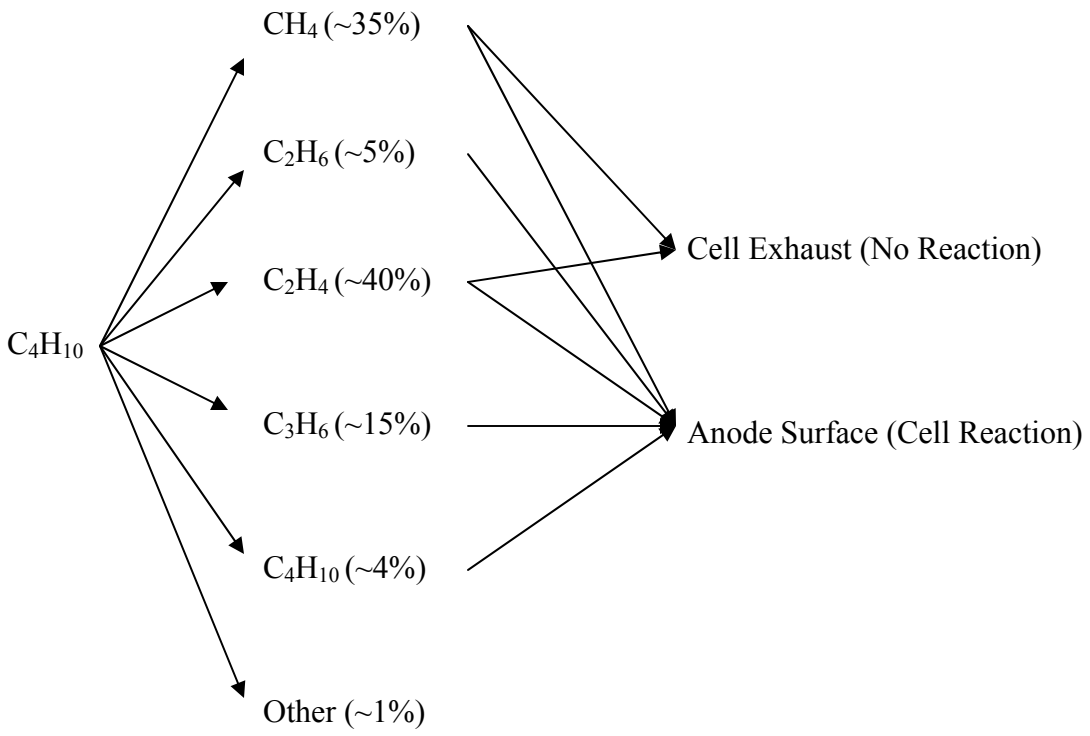

Figure VIII.1. Projected butane pyrolysis in our cells.[3]

Based on the exhaust data in Chapter IV, it is known that more than half of the methane that is introduced into the anode chamber passes through the cell without undergoing any reaction. Ethylene also appears in cell exhaust, however it also contributes to carbon deposition so the amount of ethylene in the exhaust flow relative to the inlet is unknown. All fuels participate in anodic reactions. At the anode, the fuels are catalytically broken down into their component atoms; hydrogen and carbon. The distinct lack of C-H Raman bands in the *in-situ* spectra indicate that hydrogen atoms, whether separate from or part of a (hyrdo)carbon structure, react immediately to form water. The carbon reaction is notably slower and excess fuel leads to carbon formation on the surface of the anode

Carbon formation on SOFC anodes as a result of high molecular weight hydrocarbon fuel usage is a complicated process. However, conclusions can be

drawn based on the studies of butane pyrolysis products in Chapters VI and VII. Experiments using methane indicate that methane is relatively unreactive not only in terms of carbon deposition, but in terms of oxidation. The little carbon formed on the anode surface by methane decomposition is highly ordered and remains so as more fuel is added. The more highly ordered structure of the deposit is likely a result of the slow formation rates with pure methane feeds that result from the reactant's stability.

Ethylene is more reactive than methane on the anode surface due to the presence of the unsaturated carbon-carbon double bond. Thus, more graphite is formed per equivalent amount (by mole) of fuel. Initially ethylene produces ordered graphite having large domain sizes. As deposition continues, however, the domain size rapidly decreases due to the rapid carbon deposition kinetics of ethylene. Furthermore, each mole of ethylene has two carbon atoms that can potentially act as nucleation sites, while methane only has one. A higher number of nucleation sites will lead to more defects and a correspondingly higher number of domains.

With propylene disorder within the deposited carbon increases further. Raman spectra show that propylene deposits are indistinguishable spectroscopically from those formed by butane. This observation implies that although propylene is only ~15% of the fuel flow, it is most responsible for the type of carbon present after butane exposure and therefore, must form graphite on the surface much faster than the other butane pyrolysis products. The considerably smaller domain size of graphite formed by propylene probably results from both the higher number of carbon atoms per mole of propylene as well as the asymmetry intrinsic to the molecule itself. If the carbon-carbon double bond is more likely to promote graphite formation than the

methyl group then carbon deposition is likely to occur in an anisotropic manner. Anisotropic evolution, in turn, can create yet more nucleation sites for carbon growth.

In Figure VIII.2, potential terminal sites (and grain boundaries) are designated by the letter "T". All labeled terminal site are methyl groups, where the carbon is saturated in a sp^3 hybridization and therefore less reactive than the sp^2 sites of the graphite structure or the incoming fuel with carbon-carbon double bonds. The propagation of these terminal sites with lead to grains and edge boundaries that will increase the amount of sp^3 coordinated carbon appearing in the "D" feature of the measured Raman spectra. The simple representation in Figure VIII.2 shows how the number of potential terminal sites increases from methane to propylene.

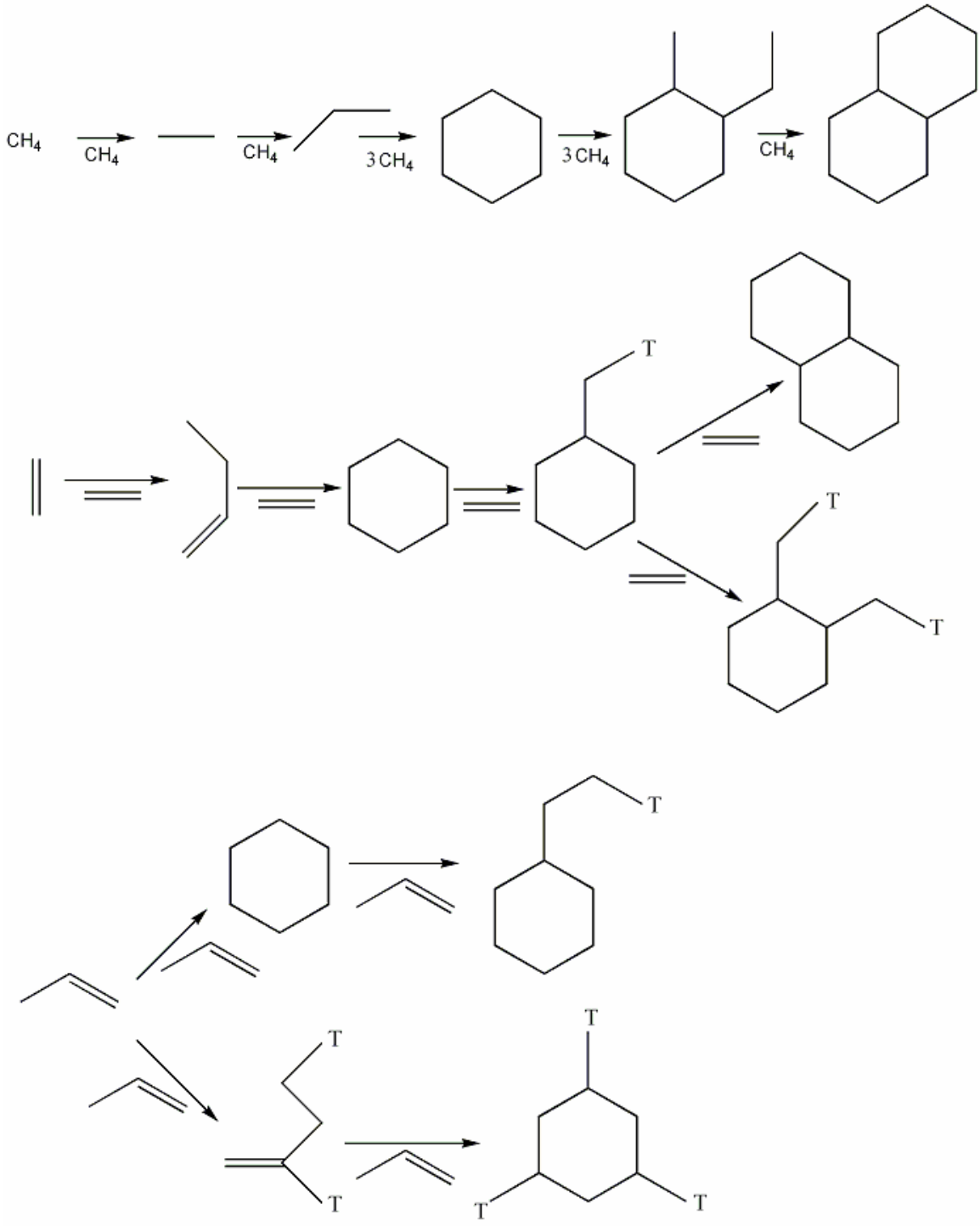

Figure VIII.2. Carbon deposition pathways of the three major butane pyrolysis products.

Once carbon deposits have formed on the anode they can be oxidized by polarizing the cell and inducing an oxide flux across the electrolyte membrane. The

anodes in this study are ~20 μm thick, falling within the range of anode thicknesses considered to be electrochemically active (10 – 90 μm).[6,7] In this case the deposits are susceptible to two sources of oxidation; oxide ions and water from the oxidation of hydrogen. This competition makes a kinetic study of carbon oxidation difficult. The resolution of reaction kinetics requires more than time-acquired Raman spectroscopy with a one minute temporal resolution. Kinetic modeling experiments based on this data are required and feasible, considering previously published work.[8,9] However, the probable reaction pathways can be hypothesized and are shown in Figure VIII.3.

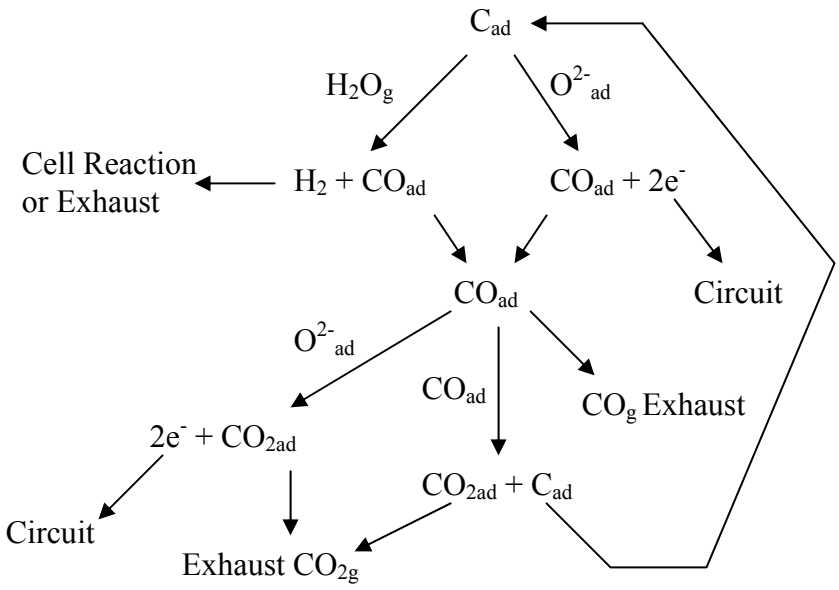

Figure VIII.3. Possible reaction pathways for the oxidation of carbon deposits adsorbed to the anode surface.

The complete oxidation of carbon requires two separate oxidation events. The first event must happen on the surface. The Raman data in Chapter VI shows that the G peak of ordered graphite diminishes more slowly than the D peak indicating that edge sites or other disordered regions are more easily oxidized. Once CO_{ad} is formed

there are multiple reactions that can occur. The simplest reaction is for CO to desorb from the surface. Once in the gas phase CO can either participate in a gas-phase shift reaction with water to form CO_2 and hydrogen gas or pass out of the cell through the exhaust flow. The presence of CO in the exhaust is clear from the data in Chapter IV that shows CO present in the effluent of both methane and butane fuels. Two surface reactions could occur: the electrochemical oxidation to CO_2, which would be ideal to efficient cell operation, or the surface Boudouard reaction that is discussed in Chapter V, which would lead to the non-electrochemical formation of CO_2 and deposited carbon.

This discussion is the best approximation of the hydrocarbon fuel oxidation reaction that can be concluded from the data in this thesis. A better resolved mechanism requires pyrolysis studies of fuel inlet conditions that more closely resemble the conditions in the *in-situ* Raman experiments. Nevertheless, the *in-situ* experiments have successfully identified surface species in working SOFCs and have resulted in the first experimental, chemically specific mechanistic information.

3. Future Directions

The work presented in this thesis has demonstrated the usefulness of optical spectroscopy in the study of fuel cell chemistry. Despite the resulting advancements in the mechanistic understanding fuel utilization, there remain many unanswered questions.

The most important mechanistic consideration is the proposed role of the three-phase boundary. This junction between the fuel, the anode and the electrolyte is obscured when cermet anodes are used. A full understanding of this interface

requires the use of *in-situ* Raman spectroscopy, a technique now proven to be capable of characterizing SOFC surfaces. Based on the results of the studies in this thesis, it is likely that the molecular species present on the anode and the electrolyte differ from each other. Furthermore, the interface between the metal and the ceramic is expected to change depending on the fuel used and polarization of the cell, two variables explicitly examined herein. The investigation of conditions across this boundary requires the use of a translational stage (already in place) to allow surface mapping. Characterizing the anode, electrolyte, and intermediates in this system will more clearly define the role of the individual components in the electrochemical fuel oxidation mechanism.

Studies of SOFCs with ceria-based anodes are already underway at the University of Maryland, however, *in-situ* spectroscopic experiments have not begun. Changing the anodic catalyst will undoubtedly change the fuel utilization reaction. Ceria, or any other potential anode material, will likely induce the formation of different deposits and intermediates. A less active electrocatalyst may afford the opportunity to identify non-graphitic species, such as polyaromatic-hydrocarbons and partially oxygenated carbon compounds. Aside from material considerations, temperature and architecture also play a role in cell operation. A cell operated at 850 °C will perform differently than a cell at 715 °C. Likewise, an anode-supported cell with perform differently from the electrolyte-supported cells in this study. Changing these three variables requires little to no adjustment to the optically accessible SOFC rig already in use. The result of these studies would lead to a comprehensive library of reaction intermediates, which would be one component of

an unparalleled understanding of SOFC operation – along with electrochemical characterization and kinetic modeling studies.

Further implementation of *in-situ* optical spectroscopy requires more considerable experimental adjustments. However, the experimental procedures developed in this study are capable of characterizing processes in other systems, such as proton exchange membrane fuel cells (PEMFCs). The materials and processes involved in PEMFCs are different, both in function and optically, from SOFC anodes. Most notably, PEMFCs are more susceptible to poisoning from carbon and sulfur fuel impurities. Fortunately, both carbon and sulfur are strong Raman scattering materials. The implementation of *in-situ* spectroscopy will require the construction of an optically accessible rig that is unique from the one used in SOFC studies, however, PEMFCs operate at much lower temperatures (~25 - ~120 °C) so less protection is required for temperature sensitive materials. Significantly less blackbody radiation will also allow for the opportunity to carry out complementary IR-based measurements.

There are many other high-temperature or volatile systems that can be studied *in-situ* with optical spectroscopy. Specifically, Raman spectroscopy has proven to be a technique that can provide significant insight about how these complicated devices operate. This thesis should serve as the first in a series of studies that will characterize such chemistry. Hopefully the impact of these and future results leads to the development of better fuel cell systems and, in turn, more widespread implementation of these environmentally and economically important devices.

4. References

(1) Gupta, G. K.; Dean, A. M.; Ahn, K.; Gorte, R. J. *J. Power Sources* **2006**, *158*, 497.

(2) Gupta, G. K.; Hecht, E. S.; Zhu, H. Y.; Dean, A. M.; Kee, R. J. *J. Power Sources* **2006**, *156*, 434.

(3) Sheng, C. Y.; Dean, A. M. *J. Phys. Chem. A* **2004**, *108*, 3772.

(4) Walters, K. M.; Dean, A. M.; Zhu, H. Y.; Kee, R. J. *J. Power Sources* **2003**, *123*, 182.

(5) Zhu, H. Y.; Colclasure, A. M.; Kee, R. J.; Lin, Y. B.; Barnett, S. A. *J. Power Sources* **2006**, *161*, 413.

(6) Brown, M.; Primdahl, S.; Mogensen, M. *J. Electrochem. Soc.* **2000**, *147*, 475.

(7) Divisek, J.; Jung, R.; Vinke, I. C. *J. Appl. Electrochem.* **1999**, *29*, 165.

(8) Bessler, W. G.; Warnatz, J.; Goodwin, D. G. *Solid State Ionics* **2007**, *177*, 3371.

(9) Zhu, H. Y.; Kee, R. J.; Janardhanan, V. M.; Deutschmann, O.; Goodwin, D. G. *J. Electrochem. Soc.* **2005**, *152*, A2427.

Appendix 1: Solid Oxide Fuel Cell Assemblies.

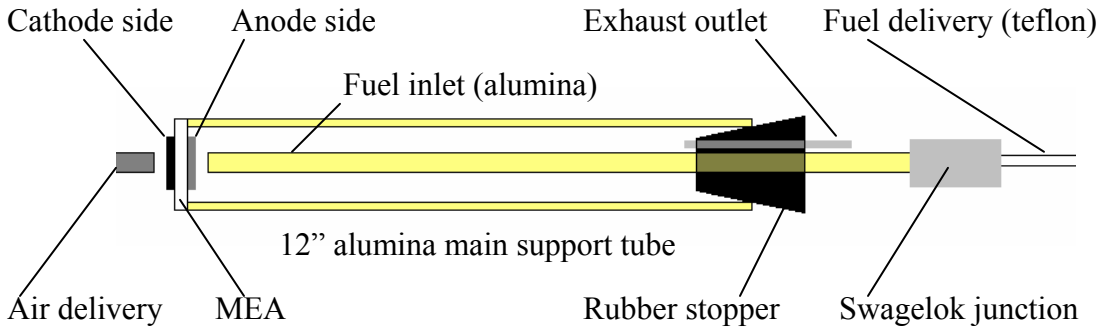

The fuel cell assembly, or rig, used in the non-optical experiments detailed in Chapters III and IV is shown above. Details of the preparation for each experiment are presented in the respective chapters. The rubber stopper is a trade size 3 rubber plug (15/16” larger end, 23/32” small end) with a 13/64” through hole (McMaster Carr). The inlet tube is place through the hole such that the inside end is 5 mm from the anode. The exhaust outlet is a needle that is fed through the bulk of the stopper. The fuel inlet is attached to the Teflon fuel delivery tube (1/8” outer diameter, 1/16” inner diameter) by a Swagelok junction. The air delivery tube is a Hastex Ni-alloy tube.

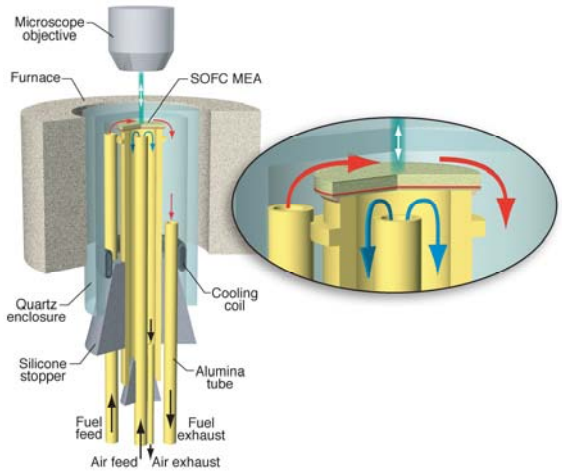

The fuel cell rig used in the optical experiments in Chapers V, VI, and VII is shown above. Details of the preparation for each experiment are presented in the respective chapters. The main alumina tube is 12” long, the fuel and air feed alumina tubes are 10” long and the exhaust tube is 6” long. The large silicone stopper has a 2-13/64” large end, a 1-7/8” small end and is 1” in height (McMaster Carr). A scalpel is used to bore holes in the stopper for the main, feed, and exhaust tubes as well as the inlet tubes for the cooling coil. The cooling coil is and HPLC coil scavenged from an unknown HPLC machine. The small rubber stopper, air feed and exhaust are assembled in the same manner as the fuel side of the non-optical rig. The quartz casing is a custom-designed piece that is 10” long, has 1/8” walls and an optically smooth window on the top end (Quark Enterprises). The furnace is a custom design with two 180° semi-cylindrical heaters that have 3” inner diameter (Thermcraft). The heating elements are 7” in length with a 2” vestibule on the bottom and a 1” vestibule on the top. The furnace control was also provided by Thermcraft and a K-type thermocouple was inserted through the bottom vestibule.

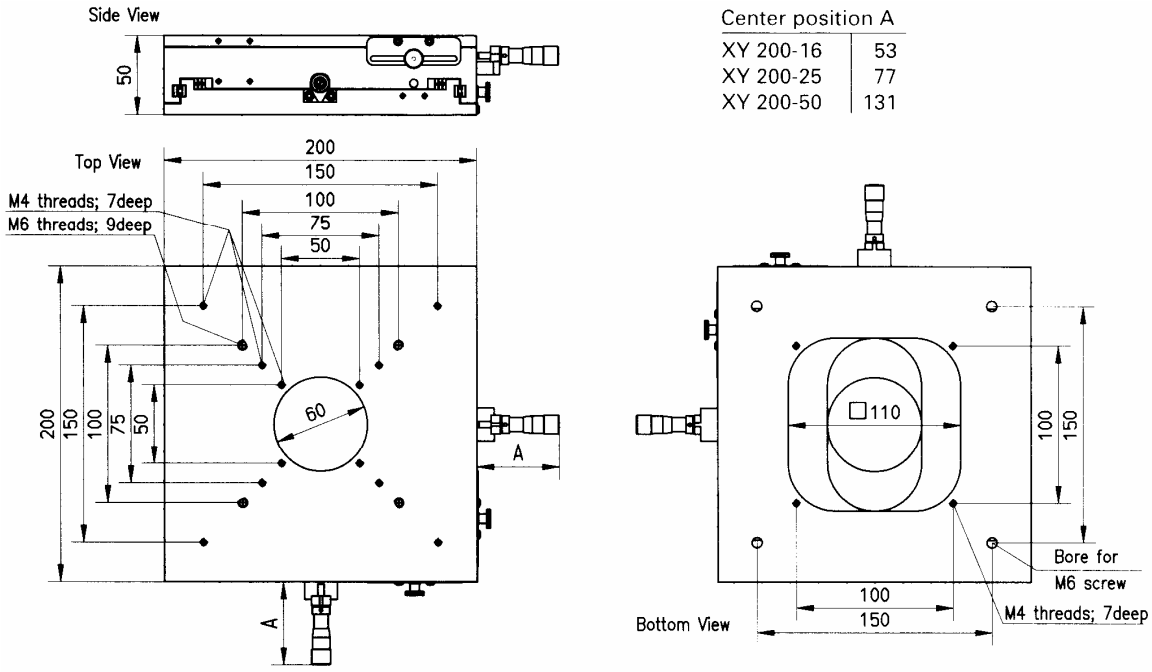

The translational stage used to allow the probing of various anode sites in the optical fuel cell rig is shown above (Linos). 2" support posts are screwed into the M6 threads on the top. 0.5" legs are screwed into the M4 threads on the bottom. Custom made aluminum legs and support posts are shown below.

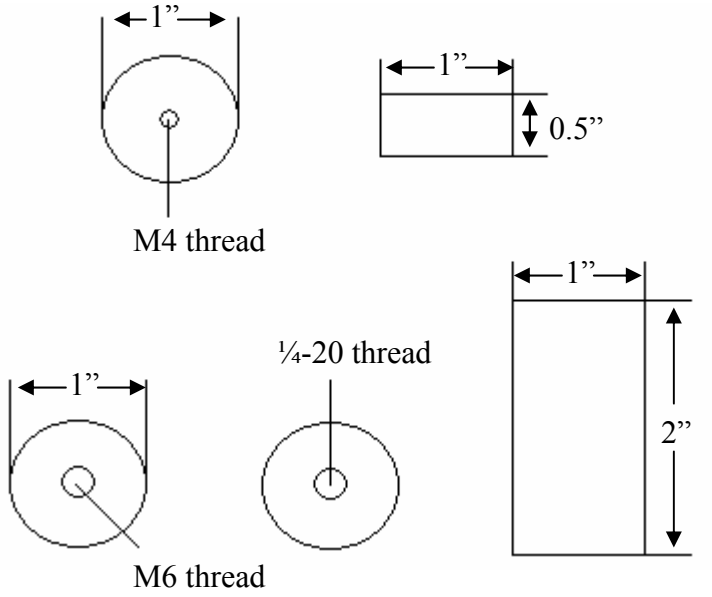

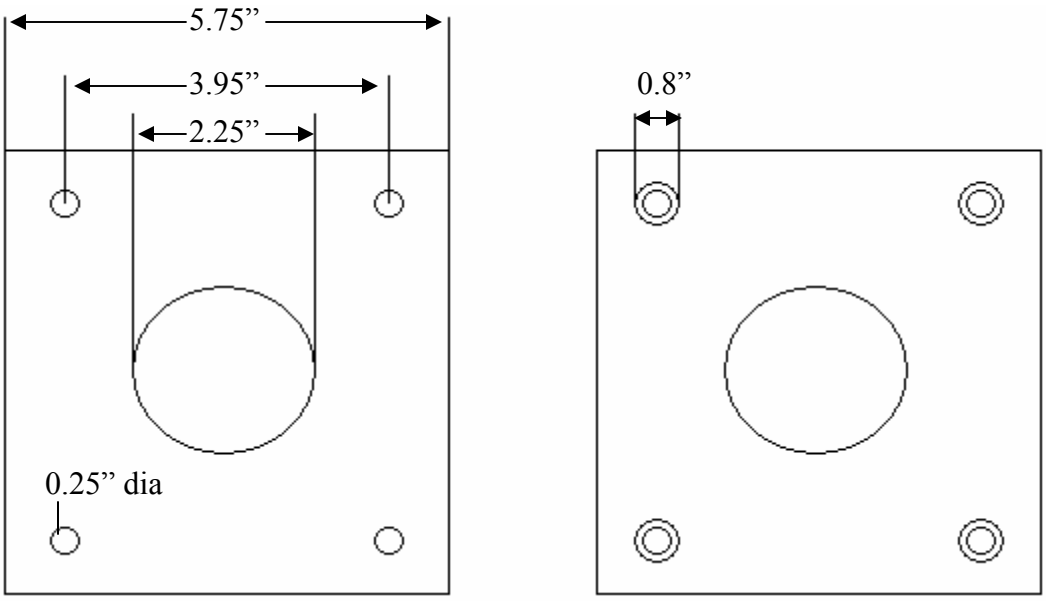

The furnace support for the optical fuel cell rig is shown above (custom made). The bottom view is shown on the left, top view on the right. The 1” thick support stage (stainless steel) is attached to the support posts shown above with ¼-20 set screws.

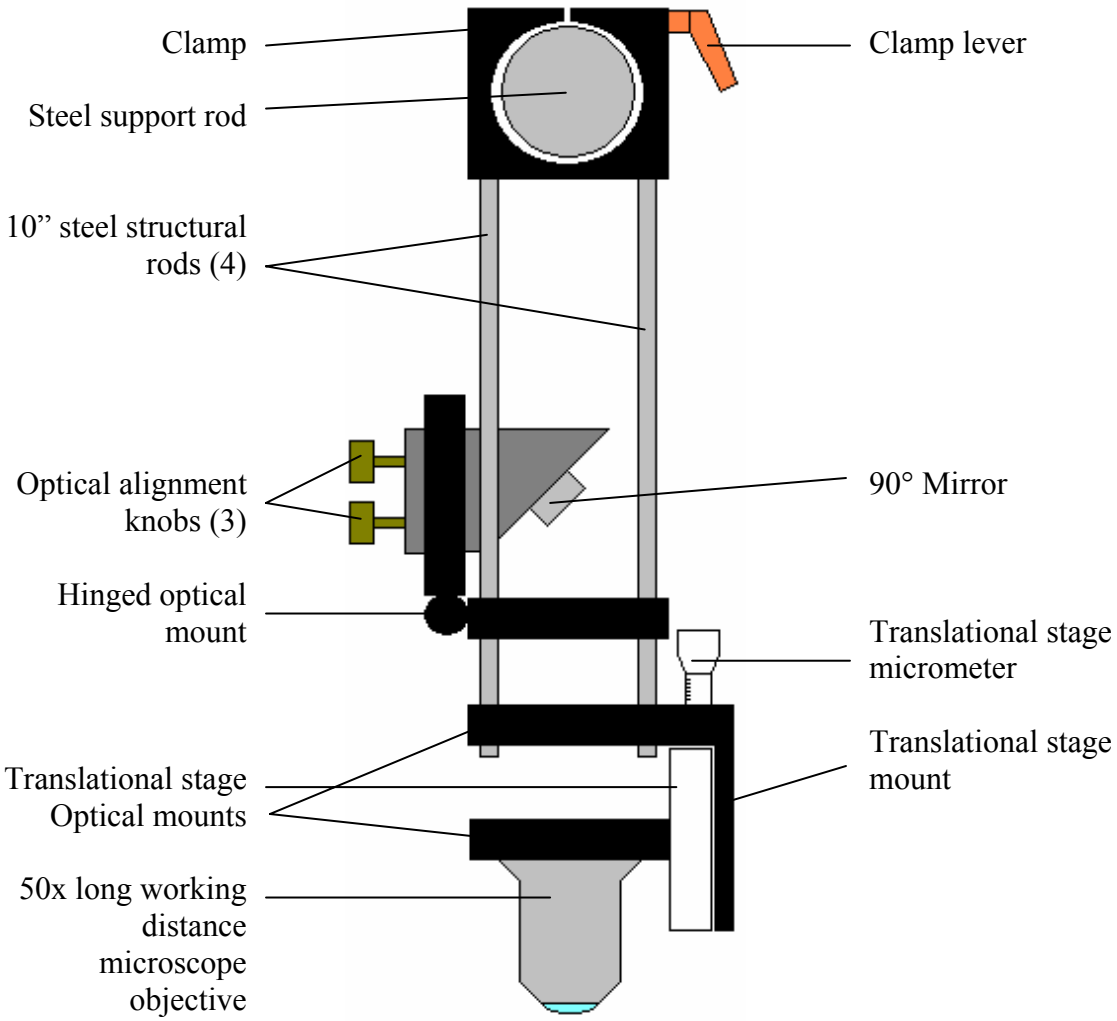

The optical arrangement is shown above. All pieces were acquired from Linos except the objective (Leica), mirror (Edmund Optics) and steel support rod (custom made). For clarity the Linos part numbers are given below.

Part	Number
Clamp	06 1082
Structural rods	06 1216
Adjustable mirror mount	06 5087
Hinge	06 5067
Optical mounts	06 1042
Translational stage	08 0211
Objective mount	06 5082

Appendix 2: Optical Fuel Cell Rig Diagnostics

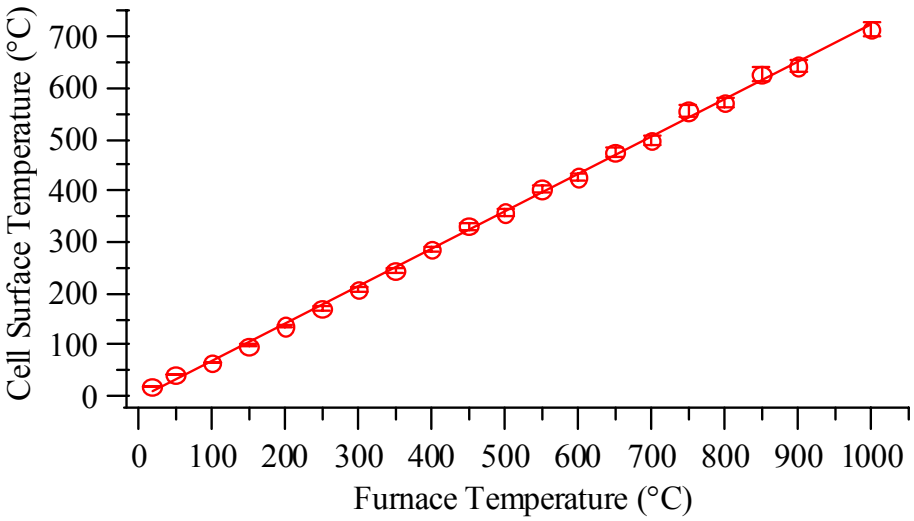

The calibration of the cell anode-side surface temperature to the regulated furnace temperature is shown above. The furnace temperature was measured by a thermocouple placed on the outside wall of the quartz tube at half the height of the heating elements. The cell surface temperature was measured by a thermocouple attached to the cell surface with zirconia paste. Both thermocouples were K-type.

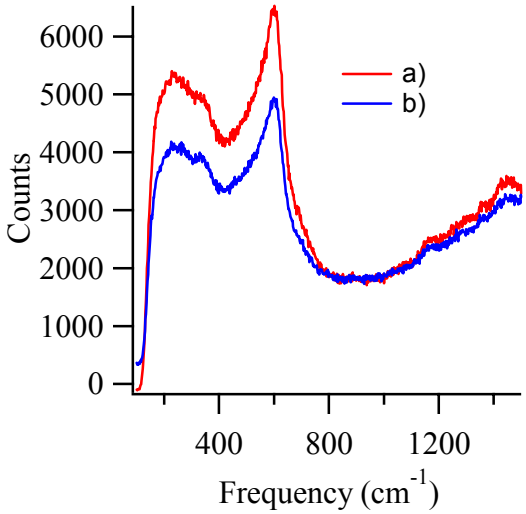

The *in-situ* investigation of YSZ reduction in a reducing atmosphere is shown above. Spectrum a) is of YSZ in air, spectrum b) is of the same sample in 5% H_2, 95% Ar. Both spectra were acquired at 800 °C. The net signal intensity drops by 25%, a mark comparable to the *ex-situ* results discussed in Chapter II.

Appendix 3: Representative Data

Representative data of the two types of high-temperature (715 °C) SOFC optical experiments are presented in this appendix. The first type of optical experiment is "Raman intensive" and is designed to identify carbon deposits that are formed at various cell potentials. Short Raman acquisitions allow the oxidation of the carbon deposits to be tracked with a temporal resolution of one minute.

Before the experiment begins three sets of Raman data are taken. The first is of the anode surface at operational temperature. This acquisition consists of 10 co-added 10 s scans over the 100-3200 cm^{-1} frequency range. An example is shown below.

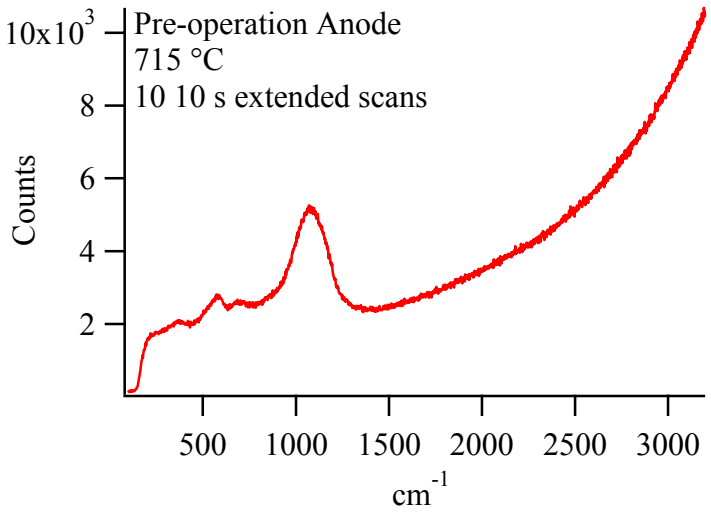

The second preliminary set is of the anode being reduced as H_2 is introduced to the anode chamber. Each spectrum consists of 30 co-added 1 s scans over the 600-1600 cm^{-1} frequency range. Each acquisition takes 1 min to complete. The H_2 flow is started at the beginning of the second acquisition and is slowly increased to 100 sccm over the course of 2 min. There is a constant 150 sccm Ar flow through the anode chamber.

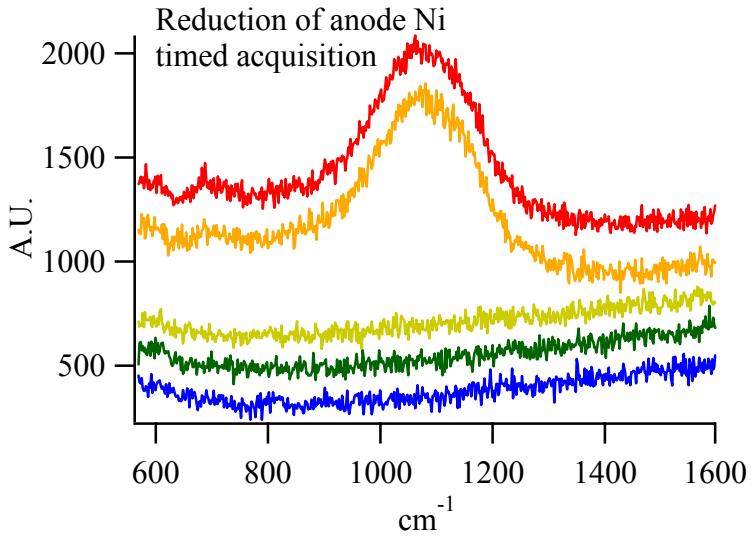

The final preliminary set of data tests the anode chamber for air leaks. The Raman acquisition procedure is the same as the anode reduction. The H_2 is flow is stopped at the beginning of the second. There is a constant 150 sccm Ar flow through the anode chamber.

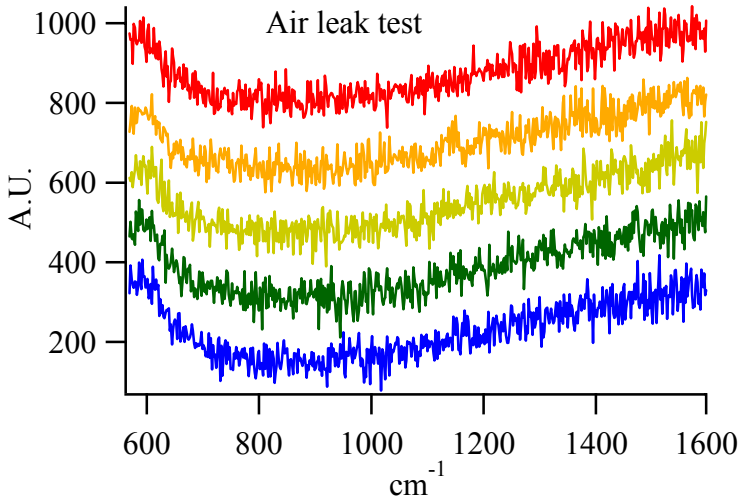

After a successful leak test the "burst" experiments described in Chapters V and VI begin. Raman data is acquired as described in the Experimental sections of those chapters at three cell potentials (OCV, OCV – 0.3 V, and OCV – 0.6 V). At the two higher cell potentials the lack of oxidant in that anode-side atmosphere allows carbon deposits to form on the optical window. In these cases Raman data is acquired until these deposits block the incident laser. Otherwise data for 5 "burst" are collected. Representative data from an ethylene experiment is shown below.

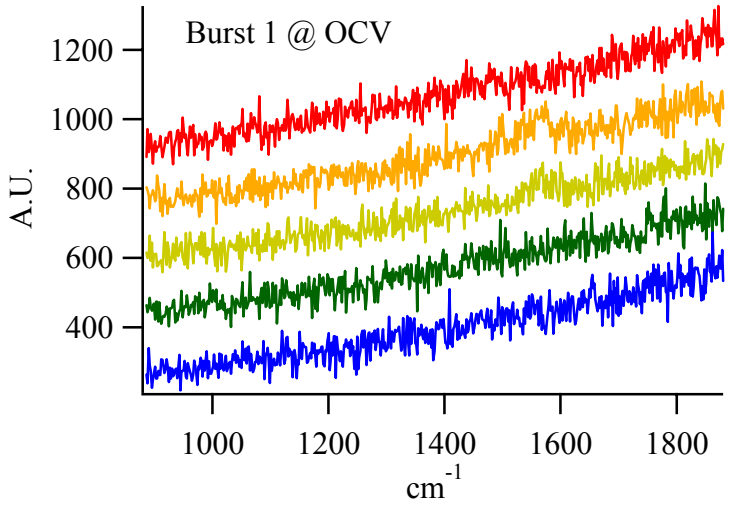

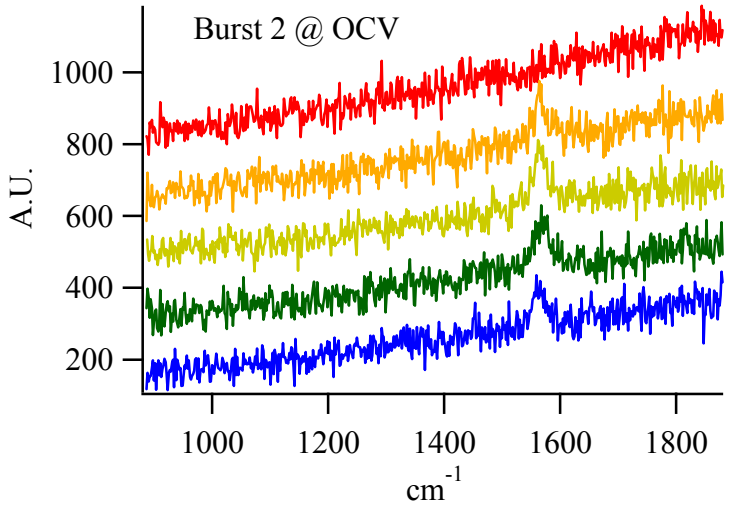

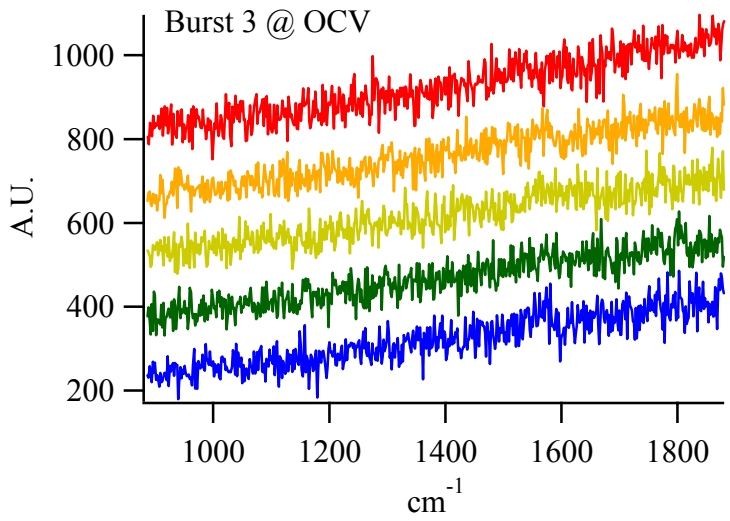
Burst 3 @ OCV
1000
800
600
400
200
A.U.
1000
1200
1400
1600
1800
cm-1

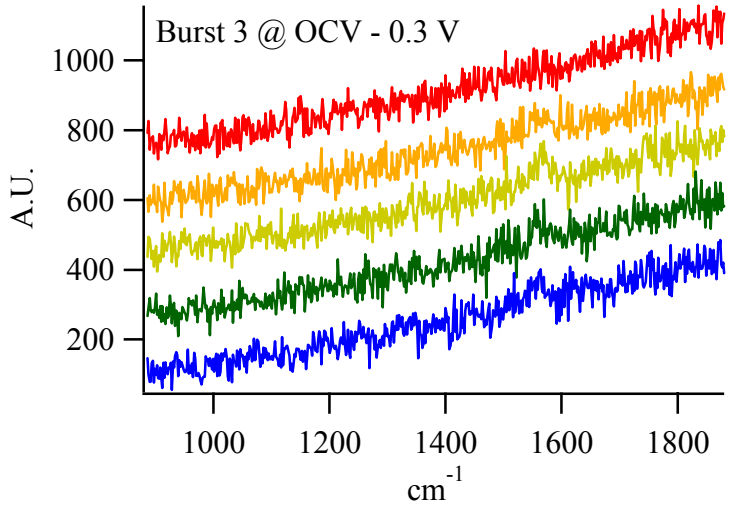
Burst 3 @ OCV - 0.3 V
1000
800
600
400
200
A.U.
1000
1200
1400
1600
1800
cm-1

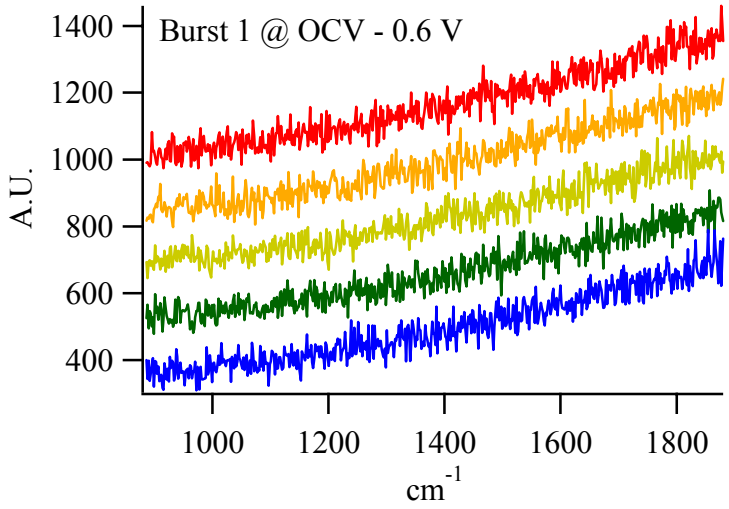
Burst 1 @ OCV - 0.6 V
A.U.
1400
1200
1000
800
600
400
1000
1200
1400
1600
1800
cm-1

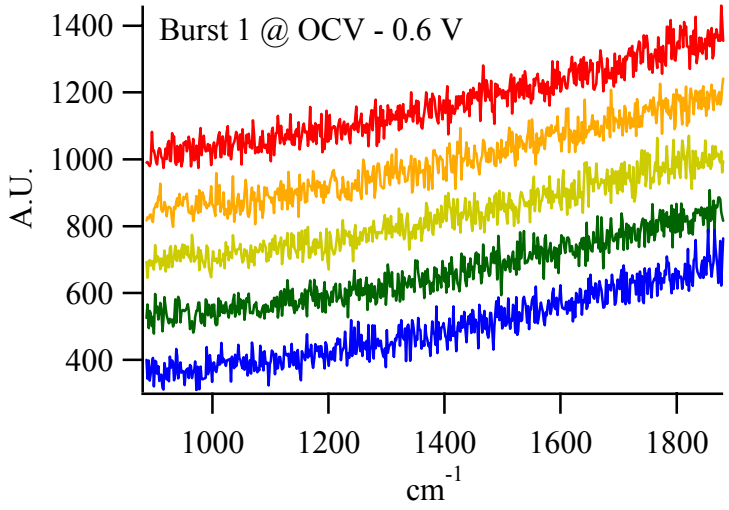
Burst 1 @ OCV - 0.6 V
A.U.
1400
1200
1000
800
600
400
1000
1200
1400
1600
1800
cm-1

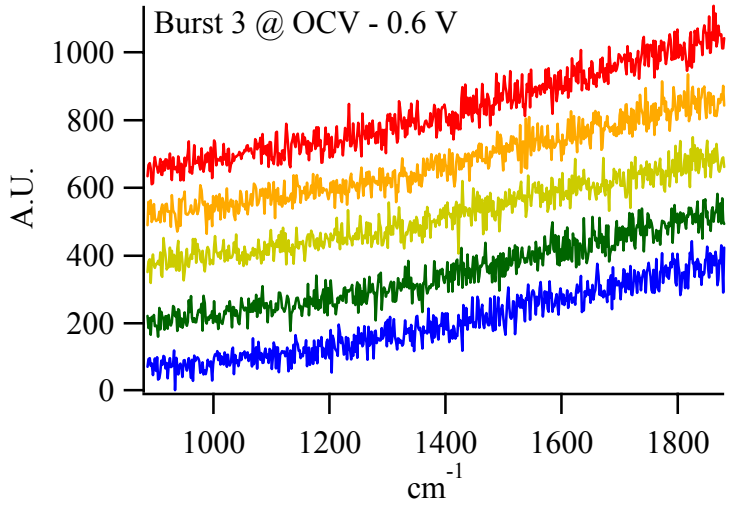
Burst 3 @ OCV - 0.6 V
A.U.
1000
800
600
400
200
0
1000
1200
1400
1600
1800
cm-1

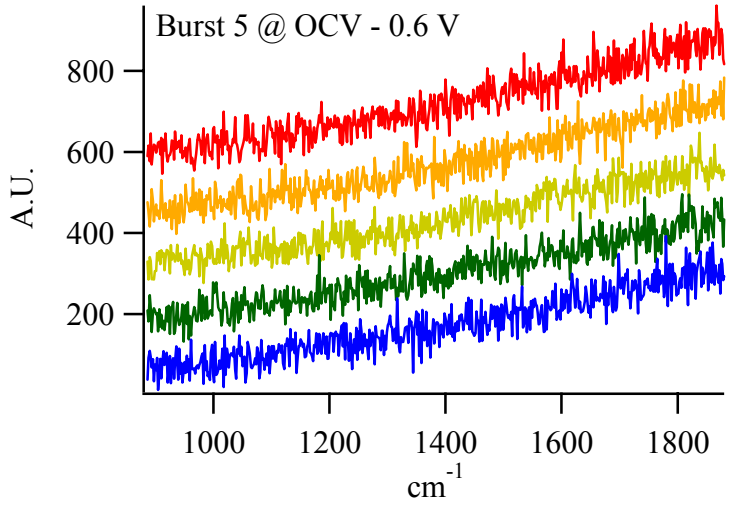
Burst 5 @ OCV - 0.6 V
A.U.
800
600
400
200
1000
1200
1400
1600
1800
cm-1

These experiments are focused on the characterization of the carbon deposits. Therefore, voltammetry scans are only taken before each over potential. The anode chamber is "cleaned" after each cell potential experiment by introducing air into anode-side flow. The anodes are then re-reduced and the voltammetry scan is taken. Representative data is shown below.

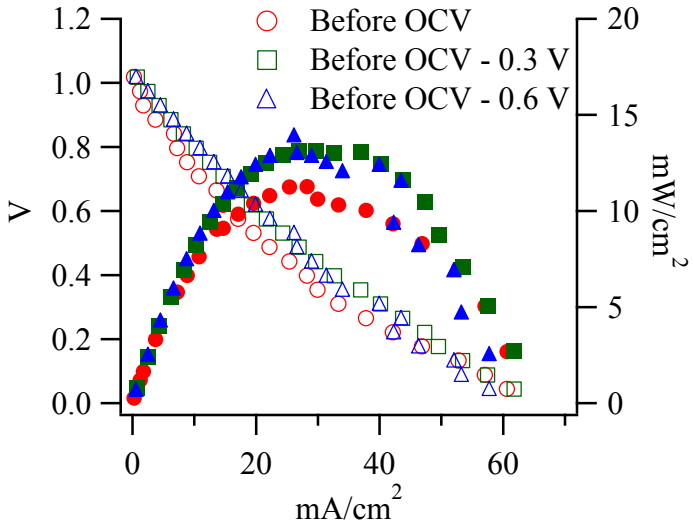

The second type of optical experiment is “electrochemically intensive” and is designed to track cell performance as carbon deposits are formed at OCV. The same preliminary tests are done prior to these experiments as were done for the first set. Raman data is acquire while the optical window is free of deposits, however this is typically on the order of only 3 or 4 bursts. Representative Raman scans from a propylene experiment are shown below.

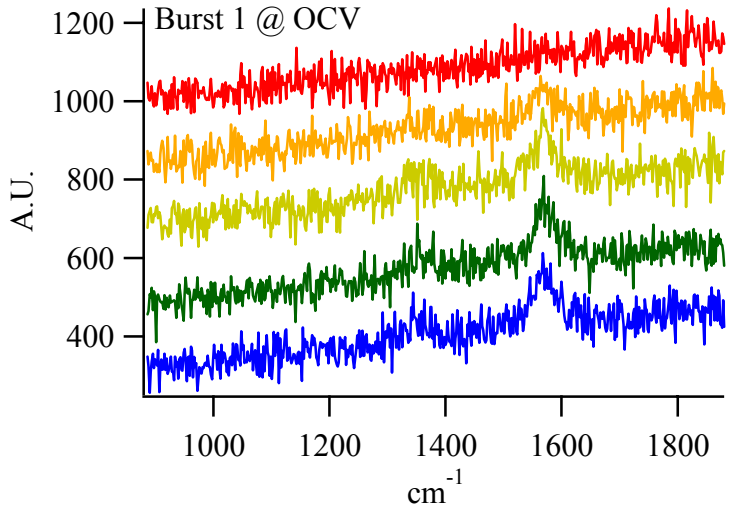

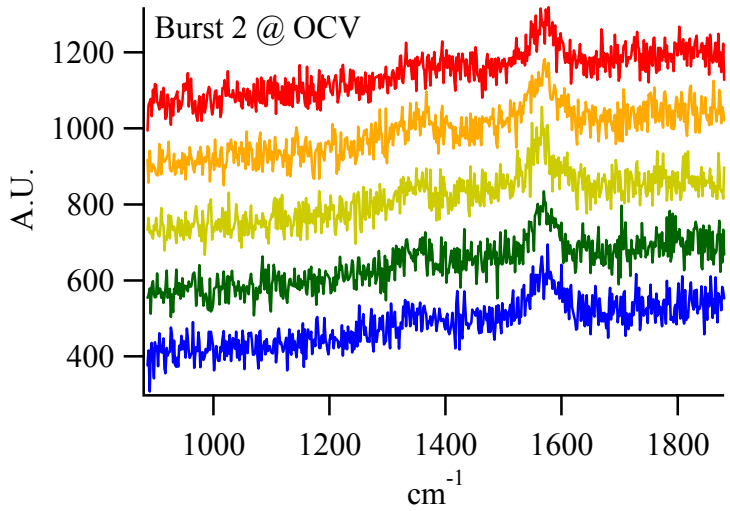

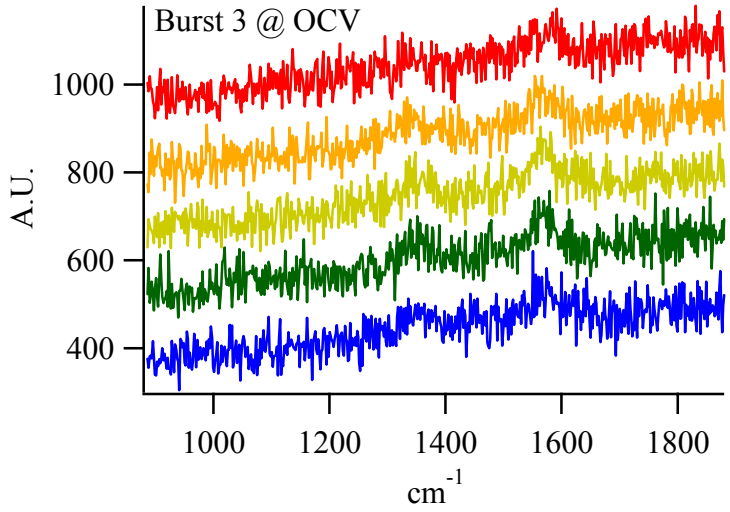
Burst 3 @ OCV
A.U.
1000
800
600
400
1000
1200
1400
1600
1800
cm-1

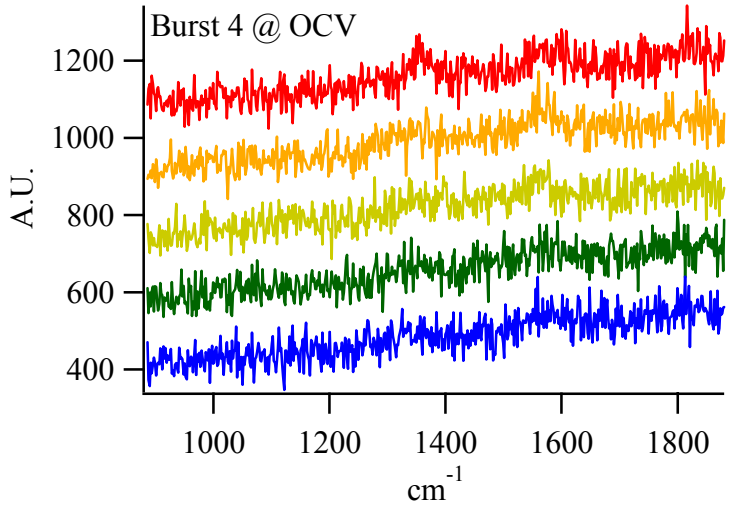
Burst 4 @ OCV
A.U.
1200
1000
800
600
400
1000
1200
1400
1600
1800
cm-1

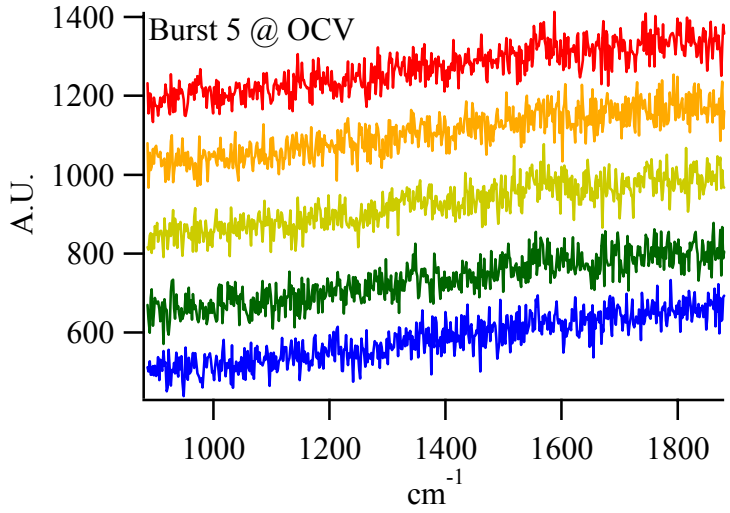

Electrochemical data is acquired as described in Chapters V, VI, and VII. EIS scans are made after each burst. Voltammetry scans are taken after bursts 5, 10, and 15 to prevent the carbon deposits that result from a single burst from being oxidized as the voltage range is scanned. Representative EIS data is shown below, followed by representative voltammetry data. Note that for clear viewing the X and Y axes in the EIS data are not equal. The important data point is the R_p value, which is shown to increase as more fuel is added. An increased R_p indicates that carbon deposition with propylene results in a higher total, ohmic cell resistance. Since conditions on the cathode side and in the bulk electrolyte are keep constant, this increase is assigned to the anode.

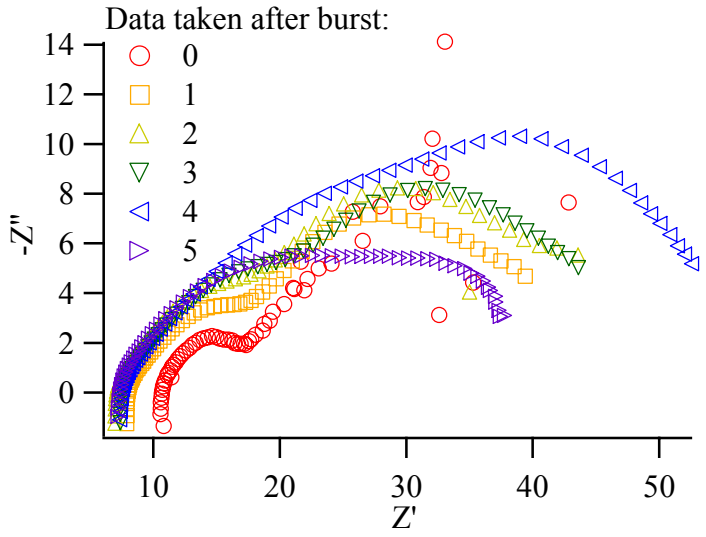
Data taken after burst:
0
1
2
3
4
5
-Z''
Z'
14
12
10
8
6
4
2
0
10
20
30
40
50

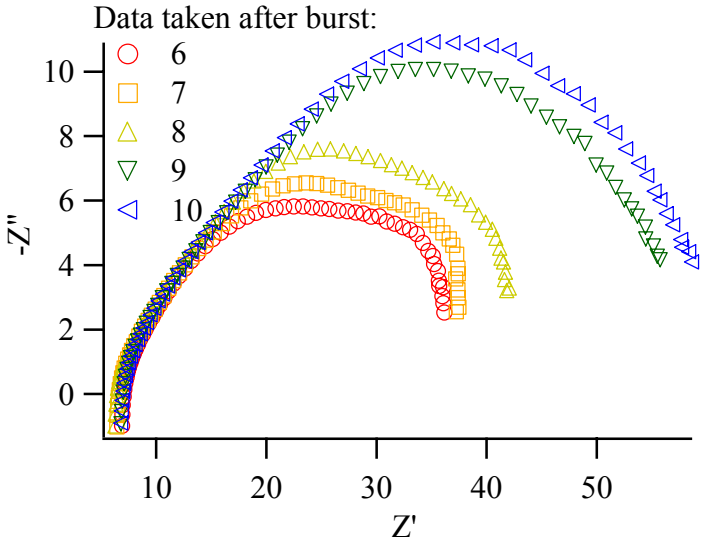
Data taken after burst:
6
7
8
9
10
-Z''
Z'
10
8
6
4
2
0
10
20
30
40
50

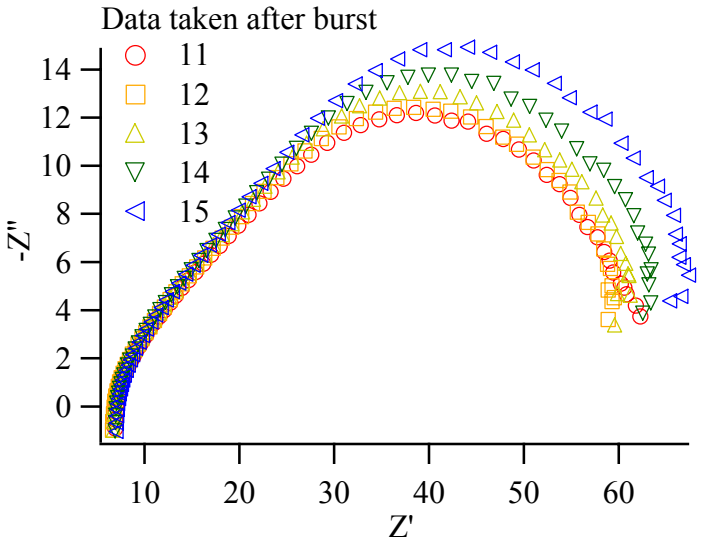
Data taken after burst
11
12
13
14
15
-Z''
Z'
0
2
4
6
8
10
12
14
10
20
30
40
50
60

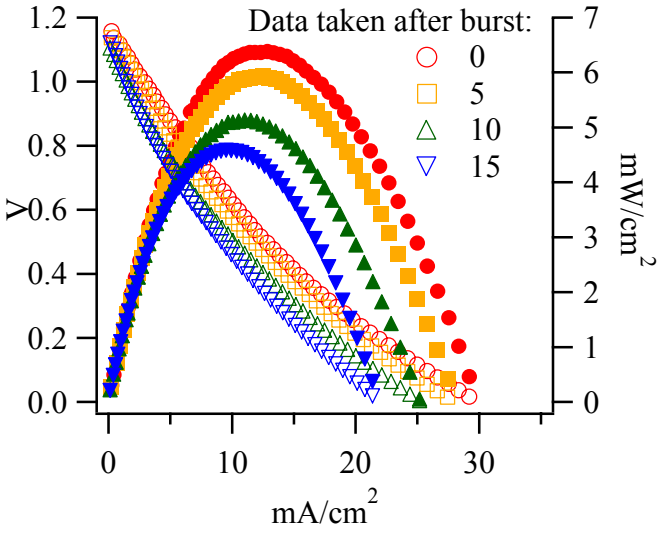
Data taken after burst:
0
5
10
15
V
mW/cm2
mA/cm2
0.0
0.2
0.4
0.6
0.8
1.0
1.2
0
1
2
3
4
5
6
7
0
10
20
30

Appendix 4: Co-author Contributions

Most chapters of this thesis appear in journals as peer-reviewed articles or have been submitted to appear as such. The contributions of the co-authors of each article are detailed below by chapter.

Chapter II (Pomfret, M. B.; Stoltz, C.; Varughese, B.; Walker, R. A. *Anal. Chem.* **2005**, *77*, 1791.) Dr. Chad Stoltz trained the author to take and analyze XRD data and advised the author on the solid state synthesis technique used to make the various compositions of YSZ. Dr. Bindu Varughese trained the author on the XPS equipment and software and advised the author on measurement procedures and analysis. Some of the XPS experiments were conducted jointly by the author and Dr. Varughese. Professor Robert A. Walker is the author's research advisor and a principle investigator on the SOFC project at UMCP. Prof. Walker advised on all experiments presented in this chapter.

Chapter III (Pomfret, M. B.; Eigenbrodt, B. C.; Demircan, O.; Eichhorn, B. W.; Walker, R. A. **in preparation**.) Mr. Eigenbrodt will conduct follow-up experiments for the publication that are not presented in this thesis. Mr. Demircan conducted early experiments that are not presented in this thesis and helped to plan the experiments that are presented. Professor Robert A. Walker is the author's research advisor. Professors Bryan W. Eichhorn, and Walker are principle investigators on the SOFC project at UMCP and advised on all experiments presented in this chapter.

Chapter IV (Pomfret, M. B.; Demircan, O.; Sukeshini, A. M.; Walker, R. A. *Environ. Sci. Technol.* **2006**, *40*, 5574.) Mr. Oktay Demircan conducted separate electrochemical experiments for his own purposes on the some of cells from which exhaust was collected. The electrochemical data presented in Figure IV.2 were provided by Mr. Demircan. Mr. Demircan also constructed many of the SOFCs used in this study. Dr. A. Mary Sukeshini provided significant advice on experimental procedure. Professor Robert A. Walker is the author's research advisor and a principle investigator on the SOFC project at UMCP. Prof. Walker advised on all experiments presented in this chapter.

Chapter V (Pomfret, M. B.; Owrutsky, J. C.; Walker, R. A. *J. Phys. Chem. B* **2006**, *110*, 17305. & Pomfret, M. B.; Owrutsky, J. C.; Walker, R. A. *Anal. Chem.* **2007**, *79*, 2367.) Dr. Jeffery C. Owrutsky helped to develop the "burst" technique for dosing the anode chamber with hydrocarbon fuels and helped to develop the Raman acquisition techniques used in this chapter. Most experiments were conducted jointly by Dr. Owrutsky and the author. Professor Robert A. Walker is the author's research advisor and a principle investigator on the SOFC project at UMCP. Prof. Walker advised on all experiments presented in this chapter.

Chapter VI (Pomfret, M. B.; Demircan, O.; Jackson, G. S.; Eichhorn, B. W.; Walker, R. A. *J. Electrochem. Soc.* **Submitted**) Mr. Oktay Demircan first identified the nanocrystalline graphite on ceria, YSZ, and gold SOFC anodes in a separate study that influenced the experiments in this chapter. Professor Robert A. Walker is the author's research advisor. Professors Gregory S. Jackson, Bryan W. Eichhorn, and

Walker are principle investigators on the SOFC project at UMCP and advised on all experiments presented in this chapter.

Chapter VII (Pomfret, M. B.; Walker, R. A. **in preparation**) Professor Robert A. Walker is the author's research advisor and a principle investigator on the SOFC project at UMCP. Prof. Walker advised on all experiments presented in this chapter.

Appendix 5: Discussion of Electrochemical Impedance Spectroscopic Data

Chapter V of this thesis focuses on the dependence of carbon growth on the polarization of the cell and the dependence of cell performance on exposure to four hydrocarbon fuels. As part of the discussion, electrochemical impedance spectroscopy (EIS) data is presented to support the trends in maximum power and current densities. A brief, yet more detailed discussion of the EIS data from each case presented in Chapter V follows.

Every EIS spectra collected in the study exhibited three arcs. In some cases the arcs are more pronounced, while in others they are more subtle. This phenomenon is shown in the figure below.

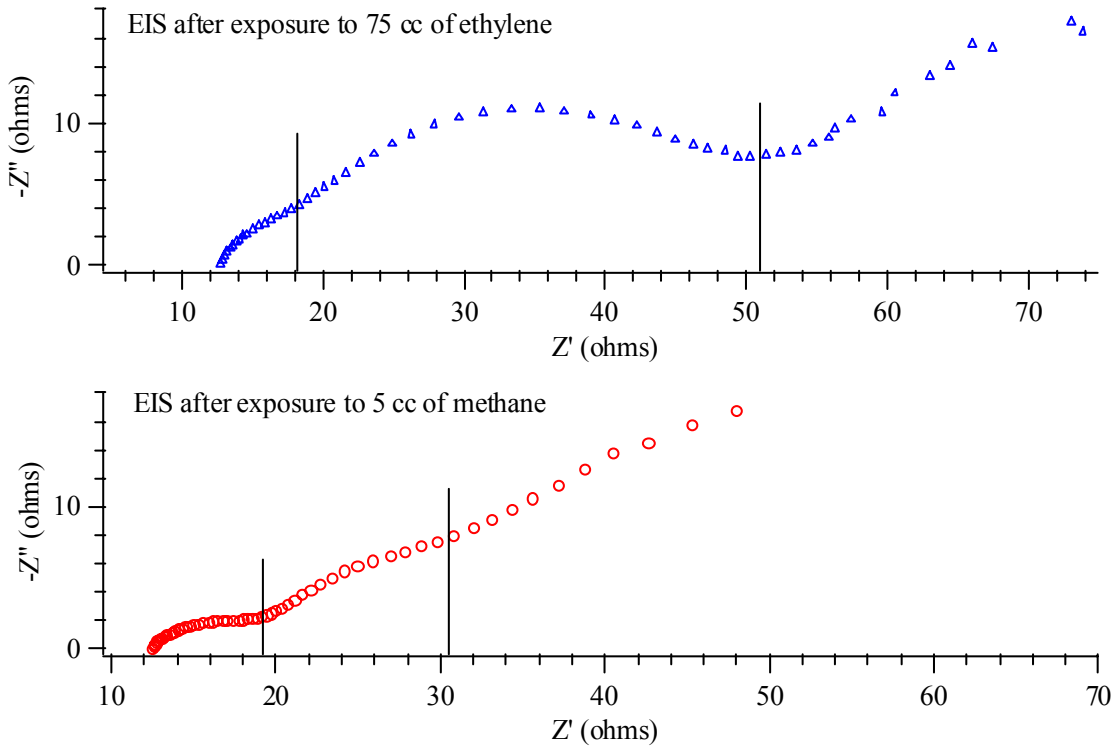

These three arcs, together with the bulk resistance value determined by high-frequency x-intercept, represent 4 circuit elements. The lack of a second x-intercept at low frequency is likely due to poor instrument performance at those frequencies. Preliminary experiments with an Autolab PGSTAT30 showed complete arcs. There is also a small hi-frequency inductance. An approximate circuit model based on the shape of the data is show below.

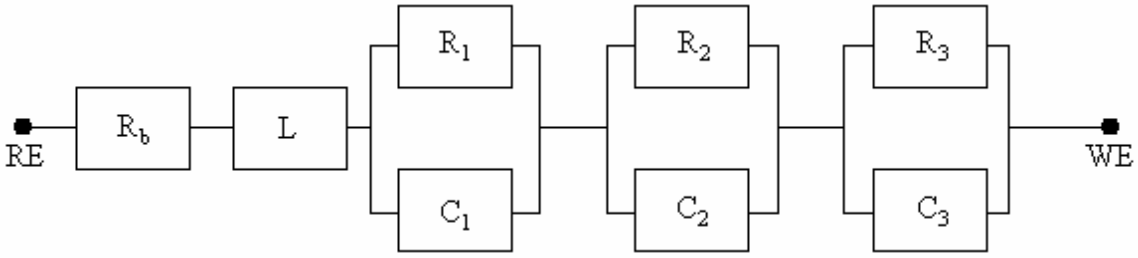

The subscript numbers refer to each arc in order of descending frequency. Typically, high frequency features are attributed to cathode processes, the low frequency features are attributed to mass transfer at the anode, and the middle arc is attributed to charge transfer processes.[1] The circuit is modeled with Gamry EChem Analyst software, using the Simplex modeling method. The values of each circuit element for each fuel at various exposures are given in the table below (uncertainties for these values are given in a table at the end of this appendix).

Circuit Elements Values for Various Amounts of Fuel Exposure									
Fuel	cc	$R_b(\Omega)$	L(H)	$R_1(\Omega)$	C_1(F)	$R_2(\Omega)$	C_2(F)	$R_3(\Omega)$	C_3(F)
CH_4	0	12.8	8.95e-7	4.15	1.21e-4	10.2	7.55e-3	27.8	9.00e-2
	25	9.40	1.25e-6	5.59	7.78e-5	10.9	6.43e-3	28.4	8.26e-2
	75	11.7	7.94e-7	8.91	4.59e-5	12.8	4.78e-3	29.4	7.20e-2
C_2H_4	0	7.29	3.83e-6	3.45	1.07e-4	5.26	5.14e-3	18.4	9.16e-2
	25	8.02	3.68e-6	4.30	7.24e-5	7.13	1.40e-3	20.6	7.54e-2
	75	13.3	2.64e-6	8.28	1.89e-5	32.5	3.14e-2	27.3	2.17e-4
C_3H_6	0	8.24	2.07e-6	2.76	1.48e-4	6.90	1.21e-2	31.6	6.72e-2
	25	7.96	1.54e-6	5.19	5.29e-5	12.1	1.33e-3	25.2	5.23e-2
	75	10.3	1.16e-6	8.46	2.53e-5	20.6	7.63e-4	25.5	3.46e-2
C_4H_{10}	0	4.94	2.20e-6	1.58	2.38e-6	8.44	1.23e-2	3.39	1.08e-1
	25	4.66	2.20e-6	2.29	3.33e-4	10.5	1.04e-2	3.90	1.17e-1
	75	5.49	2.07e-6	2.71	3.31e-4	9.85	7.22e-3	4.10	1.10e-1

For the most part, the R_b values are within three ohms for the duration of the experiment. Interestingly, there is an exception in the ethylene case where the R_b increases from ~8 ohms to ~13 ohms. This suggests a possible decrease in the active area of the anode that could lead to a slightly higher electrolyte resistance. For every fuel, R_1 (assigned to the cathode) increases, likely as a result of cell aging as the experiments are conducted. A similar trend is evident in the values of R_3. Carbon deposits will inevitably lead to more solid volume that gas-phase fuels must diffuse through, leading to the increases in the mass transfer resistances.

The most striking trends are evident in the R_2 values. For each fuel, the R_2 values follow the performance trends that appear clearly in the maximum current and power densities. This circuit model indicates that changes in the anodic charge transfer reactions resulting from carbon deposition are most responsible for differences in cell performance. As discussed in Chapter VII, the average deposit domains formed by butane have the smallest size and literature reports that the

conductivity of graphite is increased when the graphite structure becomes disordered.[2] It the follows that butane alone would form enough deposits to create a graphite network on the anode and that the graphite would exhibit adequate disorder for the network to be electrically conductive. This network would act as a current collector and some of the anodic active sites once blocked by the deposits would regain activity when connected. The graphite formed by the other three fuels does not share the small domain size – and therefore does not share the conductive attribute, thus continued exposure (up to 75 cc) only leads to the blockage of more active sites.

Associated Uncertainties of Circuit Elements

Fuel	cc	$R_b(\Omega)$	L(H)	$R_1(\Omega)$	C_1(F)	$R_2(\Omega)$	C_2(F)	$R_3(\Omega)$	C_3(F)
CH_4	0	0.1	4.30e-7	0.18	1.20e-5	0.4	5.00e-4	1.3	4.90e-3
	25	0.07	3.10e-7	0.15	4.70e-6	0.38	3.60e-4	1.2	4.20e-3
	75	0.09	3.85e-7	0.2	2.30e-6	0.48	3.00e-4	1.4	4.20e-3
C_2H_4	0	0.06	2.60e-7	0.12	8.00e-6	0.21	4.20e-4	0.64	3.90e-3
	25	0.07	2.80e-7	0.17	4.80e-6	0.23	1.10e-4	0.73	3.20e-3
	75	0.1	4.50e-7	0.3	1.10e-6	1.3	1.80e-3	0.5	9.00e-6
C_3H_6	0	0.06	2.80e-7	0.11	1.40e-5	0.31	7.00e-4	1	2.60e-3
	25	0.07	2.60e-7	0.16	3.00e-6	0.29	6.00e-5	0.8	2.40e-3
	75	0.1	3.40e-7	0.21	1.20e-6	0.47	3.20e-5	1	2.30e-3
C_4H_{10}	0	0.04	1.60e-7	0.08	2.50e-7	0.17	9.30e-4	0.29	7.00e-3
	25	0.04	1.90e-7	0.11	2.40e-5	0.17	8.00e-4	0.4	6.00e-3
	75	0.04	1.70e-7	0.07	2.30e-5	0.18	6.50e-4	0.36	7.00e-3

References:

(1) Sukeshini, A. M.; Habibzadeh, B.; Becker, B. P.; Stoltz, C. A.; Eichhorn, B. W.; Jackson, G. S. *J. Electrochem. Soc.* **2006**, *153*, A705.

(2) Peres, N. M. R.; Guinea, F.; Castro Neto, A. H. *Phys. Rev. B* **2006**, *73*, 125411.

Bibliography

Air and Radiation - Basic Information - Six Common Air Pollutants - Carbon Monoxide: Chief, 2005, http://www.epa.gov/air/urbanair/co/chf1.html.

Physics Data; Institute of Science Technology, 2006, http://www.istonline.org.uk/Handbook/40.pdf.

Abild-Pederson, F.; Lytken, O.; Engbaek, J.; Nielsen, G.; Chorkendorff, I.; Norskov, J. K. *Surf. Sci.* **2005**, *590*, 127.

Alanne, K.; Saari, A.; Ugursal, V. I.; Good, J. *J. Power Sources* **2006**, *158*, 403.

Atkinson, A.; Barnett, S.; Gorte, R. J.; Irvine, J. T. S.; McEvoy, A. J.; Mogensen, M.; Singhal, S. C.; Vohs, J. *Nature Materials* **2004**, *3*, 17.

Bard, A. J.; Faulkner, L. R. *Electrochemical Methods: Fundamentals and Applications*, 2nd Ed. ed.; John Wiley & Sons, Inc.: New York, 2001.

Bebelis, S.; Neophytides, S. *Solid State Ionics* **2002**, *152-153*, 447.

Bessler, W. G.; Warnatz, J.; Goodwin, D. G. *Solid State Ionics* **2007**, *177*, 3371.

Bieberle, A. The Electrochemistry of Solid Oxide Fuel Cell Anodes: Experiments, Modeling, and Simulations. PhD, Swiss Federal Institute of Technology, 2000.

Bieberle, A.; Gauckler, L. J. *Solid State Ionics* **2000**, *135*, 337.

Bieberle, A.; Gauckler, L. J. *Solid State Ionics* **2002**, *146*, 23.

Bieberle, A.; Meier, L. P.; Gauckler, L. J. *J. Electrochem. Soc.* **2001**, *148*, A646.

Botha, P. J.; Chiang, J. C. H.; Comins, J. D.; Mjwara, P. M.; Ngoepe, P. E. *J. Appl. Phys.* **1993**, *73*, 7268.

Bove, R.; Ubertini, S. *J. Power Sources* **2006**, *159*, 543.

Bron, M.; Holze, R. *Fresenius J. Anal. Chem.* **1998**, *361*, 694.

Brown, M.; Primdahl, S.; Mogensen, M. *J. Electrochem. Soc.* **2000**, *147*, 475.

Busca, G. *Catal. Today* **1996**, *27*, 323.

Cai, J.; Raptis, C.; Raptis, Y. S.; Anastassakis, E. *Phys. Rev. B* **1995**, *51*, 201.

Calise, F.; Palombo, A.; Vanoli, L. *J. Power Sources* **2006**, *158*, 225.

Carpenter, A. R.; Hinze, P. C. *Proc. Safety Prog.* **2004**, *23*, 292.

Chen, F. Z.; Zha, S. W.; Dong, J.; Liu, M. L. *Solid State Ionics* **2004**, *166*, 269.

Chhowalla, M.; Ferrari, A. C.; Robertson, J.; Amaratunga, G. A. J. *Appl. Phys. Lett.* **2000**, *76*, 1419.

Costa-Nunes, O.; Gorte, R. J.; Vohs, J. M. *J.f Power Sources* **2005**, *141*, 241.

Deluca, N. W.; Elabd, Y. A. *J. Polym. Sci. Part B: Polym. Phys.* **2006**, *44*, 2201.

Demircan, O.; Pomfret, M. B.; Walker, R. A.; Eichhorn, B. W. **in preparation**.

Demircan, O.; Sukeshini, M.; Pomfret, M. B.; Jackson, G. S.; Walker, R. A.; Eichhorn, B. W. "Formation of Carbon Deposits from Hydrocarbon Fuels in SOFC: Towards a Mechanistic Understanding"; 205th Meeting of The Electrochemical Society, 2004, San Antonio, TX.

Divisek, J.; Jung, R.; Vinke, I. C. *J. Appl. Electrochem.* **1999**, *29*, 165.

Dong, J.; Cheng, Z.; Zha, S. W.; Liu, M. L. *J. Power Sources* **2006**, *156*, 461.

Faber, J.; Mueller, M. H.; Cooper, B. R. *Phys. Rev. B* **1978**, *17*, 4884.

Farrauto, R.; Hwang, S.; Shore, L.; Ruettinger, W.; Lampert, J.; Giroux, T.; Liu, Y.; Ilinich, O. *Annu. Rev. Mater. Res.* **2003**, *33*, 1.

Faungnawakij, K.; Kikuchi, R.; Eguchi, K. *J. Power Sources* **2007**, *164*, 73.

Feinberg, A.; Perry, C. H. *J. Phys. Chem. Solids* **1981**, *42*, 513.

Feng, B.; Wang, C. Y.; Zhu, B. *Electrochem. Solid State Lett.* **2006**, *9*, A80.

Ferrari, A. C.; Robertson, J. *Phys. Rev. B* **2000**, *61*, 14095.

Finnerty, C. M.; Coe, N. J.; Cunningham, R. H.; Ormerod, R. M. *Catal. Today* **1998**, *46*, 137.

Fleischmann, M.; Hendra, P. J.; McQuillan, A. J.; Paul, R. L.; Reid, E. S. *J. Raman Spectrosc.* **1976**, *4*, 269.

Fontell, E.; Phan, T.; Kivisaari, T.; Keranen, K. *J. Fuel Cell Sci. Technol.* **2006**, *3*, 242.

Fujiwara, Y.; Sakai, T.; Kaimai, A.; Yashiro, K.; Nigara, Y.; Kawada, T.; Mizusaki, J. *J. Electrochem. Soc.* **2003**, *150*, E543.

Fukunaga, H.; Ihara, M.; Sakaki, K.; Yamada, K. *Solid State Ionics* **1996**, *86-8*, 1179.

Garcia, G.; Figueras, A.; Merino, R. I.; Orera, V. M.; Llibre, J. *Thin Solid Films* **2000**, *370*, 173.

Gorte, R. J.; Kim, H.; Vohs, J. M. *J. Power Sources* **2002**, *106*, 10.

Goula, G.; Kiousis, V.; Nalbandian, L.; Yentekakis, I. V. *Solid State Ionics* **2006**, *177*, 2119.

Gupta, G. K.; Dean, A. M.; Ahn, K.; Gorte, R. J. *J. Power Sources* **2006**, *158*, 497.

Gupta, G. K.; Hecht, E. S.; Zhu, H. Y.; Dean, A. M.; Kee, R. J. *J. Power Sources* **2006**, *156*, 434.

Haberman, B. A.; Young, J. B. *J. Fuel Cell Sci. Technol.* **2006**, *3*, 312.

Haslam, J. J.; Pham, A. Q.; Chung, B. W.; DiCarlo, J. F.; Glass, R. S. *J. Am. Ceram. Soc.* **2005**, *88*, 513.

Hattori, M.; Takeda, Y.; Sakaki, Y.; Nakanishi, A.; Ohara, S.; Mukai, K.; Lee, J.-H.; Fukui, T. *J. Power Sources* **2004**, *126*, 23.

Hecht, E. S.; Gupta, G. K.; Zhu, H. Y.; Dean, A. M.; Kee, R. J.; Maier, L.; Deutschmann, O. *Appl. Catal. A* **2005**, *295*, 40.

Hirabayashi, D.; Hashimoto, A.; Hibino, T.; Harada, U.; Sano, M. *Electrochem. Solid State Lett.* **2004**, *7*, A108.

Hirabayashi, D.; Tomita, A.; Brito, M. E.; Hibino, T.; Harada, U.; Nagao, M.; Sano, M. *Solid State Ionics* **2004**, *168*, 23.

Holtappels, P.; De Haart, L. G. J.; Stimming, U.; Vinke, I. C.; Mogensen, M. *J. Appl. Electrochem.* **1999**, *29*, 561.

Hughes, A. E.; Sexton, B. A. *J. Mater. Sci.* **1989**, *24*, 1057.

Ihara, M.; Hasegawa, S. *J. Electrochem. Soc.* **2006**, *153*, A1544.

Iida, T.; Kawano, M.; Matsui, T.; Kikuchi, R.; Eguchi, K. *J. Electrochem. Soc.* **2007**, *154*, B234.

Ishihara, T.; Yan, J. W.; Shinagawa, M.; Matsumoto, H. *Electrochim. Acta* **2006**, *52*, 1645.

Jacobson, M. Z.; Colella, W. G.; Golden, D. M. *Science* **2005**, *308*, 1901.

Jeanmaire, D. L.; Van Duyne, R. P. *J. Electroanal. Chem.* **1977**, *84*, 1.

Jiang, S. P.; Badwal, S. P. S. *J. Electrochem. Soc.* **1997**, *144*, 3777.

Jiang, S. P.; Wang, W. *Electrochem. Solid State Lett.* **2005**, *8*, A115.

Kakihana, M.; Osada, M. Raman Spectroscopy as a Characterization Tool for Carbon Materials. In *Carbon Alloys: Novel Concepts to Develop Carbon Science and Technology*; Yasuda, E., Inagaki, M., Kaneko, M., Endo, M., Oya, A., Tanabe, Y., Eds.; Elsevier Science, Ltd.: Oxford, UK, 2003; pp 285.

Kee, R. J.; Zhu, H. Y.; Goodwin, D. G. *Proceedings of the Combustion Institute* **2005**, *30*, 2379.

Kilo, M.; Argirusis, C.; Borchardt, G.; Jackson, R. A. *Phys. Chem. Chem. Phys.* **2003**, *5*, 2219.

Kim, T.; Liu, G.; Boaro, M.; Lee, S. I.; Vohs, J. M.; Gorte, R. J.; Al-Madhi, O. H.; Dabbousi, B. O. *J. Power Sources* **2006**, *155*, 231.

Laosiripojana, N.; Assabumrungrat, S. *J. Power Sources* **2007**, *163*, 943.

Lee, T. A.; Navrotsky, A.; Molodetsky, I. *J. Mater. Res.* **2003**, *18*, 908.

Levy, M.; Fouletier, J.; Kleitz, M. *J. Electrochem. Soc.* **1988**, *135*, 1584.

Li, C.; Sakata, Y.; Arai, T.; Domen, K.; Maruya, K.; Onishi, T. *J. Chem. Soc., Faraday Trans. 1* **1989**, *85*, 929.

Lin, Y. B.; Zhan, Z. L.; Barnett, S. A. *J. Power Sources* **2006**, *158*, 1313.

Lin, Y. B.; Zhan, Z. L.; Liu, J.; Barnett, S. A. *Solid State Ionics* **2005**, *176*, 1827.

Litster, S.; McLean, G. *J. Power Sources* **2004**, *130*, 61.

Liu, D. J.; Krumpelt, M.; Chien, H. T.; Sheen, S. H. *J. Mater. Eng. Perf.* **2006**, *15*, 442.

Liu, J. *Prog. Chem.* **2006**, *18*, 1026.

Lu, X. Y.; Faguy, P. W.; Liu, M. L. *J. Electrochem. Soc.* **2002**, *149*, A1293.

Mallon, C.; Kendall, K. *J. Power Sources* **2005**, *145*, 154.

Malzbender, J.; Wessel, E.; Steinbrech, R. W. *Solid State Ionics* **2005**, *176*, 2201.

Titanium and Zirconium in Organic Synthesis; Marek, I., Ed.; Wiley-VCH, Inc.: Weinheim, Germany, 2002.

Mathieu, D. M.; Dean, A. M.; Grenda, J. M.; Green, J. W. H. *J. Phys. Chem. A* **2003**, *107*, 8552.

Matthews, M. J.; Pimenta, M. A.; Dresselhaus, G.; Dresselhaus, M. S.; Endo, M. *Phys. Rev. B* **1999**, *59*, R6585.

McDowall, W.; Eames, M. *Energy Policy* **2006**, *34*, 1236.

McIntosh, S.; He, H.; Lee, S.-I.; Costa-Nunes, O.; Krishnan, V.; Vohs, J. M.; Gorte, R. J. *J. Electrochem. Soc.* **2004**, *151*, A604.

McIntosh, S.; Vohs, J. M.; Gorte, R. J. *J. Electrochem. Soc.* **2003**, *150*, A470.

Minh, N. Q. *Solid State Ionics* **2004**, *174*, 271.

Mizusaki, J.; Tagawa, H.; Saito, T.; Kamitani, K.; Yamamura, T.; Hirano, K.; Ehara, S.; Takagi, T.; Hikita, T.; Ippommatsu, M.; Nakagawa, S.; Hashimoto, K. *J. Electrochem. Soc.* **1994**, *141*, 2129.

Mogensen, M.; Skaarup, S. *Solid State Ionics* **1996**, *86-8*, 1151.

Mori, M.; Hiei, Y.; Itoh, H.; Tompsett, G. A.; Sammes, N. M. *Solid State Ionics* **2003**, *160*, 1.

Nabae, Y.; Yamanaka, I.; Hatano, M.; Otsuka, K. *J. Electrochem. Soc.* **2006**, *153*, A140.

Nagle, D.; PaiVerneker, V. R.; Petelin, A. N.; Groff, G. *Mat. Res. Bull.* **1989**, *24*, 619.

Nakano, H.; Ogawa, J.; Nakamura, J. *Surf. Sci.* **2002**, *514*, 256.

Nam, J. H.; Jeon, D. H. *Electrochim. Acta* **2006**, *51*, 3446.

Nesaraj, A. S.; Kumar, M.; Raj, I. A.; Radhakrishna, I.; Pattabiraman, R. *J. Iranian Chem. Soc.* **2007**, *4*, 89.

Nomura, K. AIST-Kansai, open to public, 2002, http://unit.aist.go.jp/greenlife/ii/english/itscgallary-e.htm.

Norinaga, K.; Deutschmann, O.; Huttinger, K. J. *Carbon* **2006**, *44*, 1790.

Ormerod, R. M. *Chem. Soc. Rev.* **2003**, *32*, 17.

Park, S.; Wasileski, S. A.; Weaver, M. J. *Electrochim. Acta* **2002**, *47*, 3611.

Peres, N. M. R.; Guinea, F.; Castro Neto, A. H. *Phys. Rev. B* **2006**, *73*, 125411.

Phillips, J.; Shiina, T.; Nemer, M.; Lester, K. *Langmuir* **2006**, *22*, 9694.

Pomfret, M. B.; Demircan, O.; Jackson, G. S.; Eichhorn, B. W.; Walker, R. A. *J. Electrochem. Soc.* **submitted**.

Pomfret, M. B.; Demircan, O. S., A.M.; Walker, R. A. *Environ. Sci. Technol.* **2006**, *40*, 5574.

Pomfret, M. B.; Owrutsky, J. C.; Walker, R. A. *J. Phys. Chem. B* **2006**, *110*, 17305.

Pomfret, M. B.; Owrutsky, J. C.; Walker, R. A. *Anal. Chem.* **2007**, *79*, 2367.

Pomfret, M. B.; Stoltz, C.; Varughese, B.; Walker, R. A. *Anal. Chem.* **2005**, *77*, 1791.

Primdahl, S.; Mogensen, M. *J. Electrochem. Soc.* **1997**, *144*, 3409.

Putna, E. S.; Stubenrauch, J.; Vohs, J. M.; Gorte, R. J. *Langmuir* **1995**, *11*, 4832.

Rao, A. M.; Richter, E.; Bandow, S.; Chase, B.; Eklund, P. C.; Williams, K. A.; Fang, S.; Subbaswamy, K. R.; Menon, M.; Thess, A.; Smalley, R. E.; Dresselhaus, G.; Dresselhaus, M. S. *Science* **1997**, *275*, 187.

Reinhold, M.; McGrady, J. E.; Perutz, R. N. *J. Am. Chem. Soc.* **2004**, *126*, 5268.

Rupp, J. L. M.; Drobek, T.; Rossi, A.; Gauckler, L. J. *Chem. Mater.* **2007**, *19*, 1134.

Schnapp, R. Electric Power Annual; Energy Information Administration, 2006, http://www.eia.doe.gov/cneaf/electricity/epa/epa_sum.html.

Shao, Z. P.; Haile, S. M.; Ahn, J.; Ronney, P. D.; Zhan, Z. L.; Barnett, S. A. *Nature* **2005**, *435*, 795.

Shayegan, S.; Hart, D.; Pearson, P.; Joffe, D. *J. Power Sources* **2006**, *157*, 862.

Sheng, C. Y.; Dean, A. M. “Comparison of Experimental Results to Model Predictions for n-Butane Pyrolysis Under High-Temperature Fuel Cell Conditions”;

Third Joint Meeting of the U.S. Sections of the Combustion Institute, 2003, Chicago, IL.

Sheng, C. Y.; Dean, A. M. *J. Phys. Chem. A* **2004**, *108*, 3772.

Simner, S. P.; Shelton, J. P.; Anderson, M. D.; Stevenson, J. W. *Solid State Ionics* **2003**, *161*, 11.

Sin, A.; Kopnin, E.; Dubitsky, Y.; Zaopo, A.; Arico, A. S.; La Rosa, D.; Gullo, L. R.; Antonucci, V. *J. Power Sources* **2007**, *164*, 300.

Skoog, D. A.; Holler, F. J.; Nieman, T. A. *Principles of Instrumental Analysis*, 5th Ed. ed.; Brooks/Cole Thompson Learning: Crawfordsville, MD, 1998.

Song, C. S. *Catal. Today* **2002**, *77*, 17.

Srikar, V. T.; Turner, K. T.; Ie, T. Y. A.; Spearing, S. M. *J. Power Sources* **2004**, *125*, 62.

Sukeshini, A. M.; Habibzadeh, B.; Becker, B. P.; Stoltz, C. A.; Eichhorn, B. W.; Jackson, G. S. *J. Electrochem. Soc.* **2006**, *153*, A705.

Sum, O. S. N.; Djurado, E.; Pagnier, T.; Rosman, N.; Roux, C.; Siebert, E. *Solid State Ionics* **2005**, *176*, 2599.

Sunde, S. *Electrochim. Acta* **1997**, *42*, 2637.

Svensson, A. M.; Sunde, S.; Nisancioglu, K. *J. Electrochem. Soc.* **1997**, *144*, 2719.

Tan, P. H.; Deng, Y. M.; Zhao, Q.; Cheng, W. C. *Appl. Phys. Lett.* **1999**, *74*, 1818.

Tanaka, Y.; Nguyen, T. L.; Kato, T.; Shimada, T.; Sugano, K.; Negishi, A.; Kato, K.; Nozaki, K. *Solid State Ionics* **2006**, *177*, 3323.

Tikekar, N. M.; Armstrong, T. J.; Virkar, A. V. *J. Electrochem. Soc.* **2006**, *153*, A654.

Torres, D. I.; Paje, S. E.; Llopis, J.; Morell, G.; Katiyar, R. S. *J. Lumin.* **1997**, *72-74*, 724.

Tuinstra, F.; Koenig, J. L. *J. Chem. Phys.* **1970**, *53*, 1126.

Van Speybroeck, V.; Reyniers, M. F.; Marin, G. B.; Waroquier, M. *Chemphyschem* **2002**, *3*, 863.

Wagner, C. D.; Naumkin, A. V.; Kraut-Vass, A.; Allison, J. W.; Powell, C. J.; Rumble, J. R. NIST X-ray Photoelectron Spectroscopy Database; Version 3.4 ed.; National Institute of Standards and Techonology, 2003; Vol. 2005, http://srdata.nist.gov/xps/.

Waldbillig, D.; Wood, A.; Ivey, D. G. *J. Power Sources* **2005**, *145*, 206.

Walters, K. M.; Dean, A. M.; Zhu, H. Y.; Kee, R. J. *J. Power Sources* **2003**, *123*, 182.

Wang, C.; Xui, L. H.; Tang, W. H. *Rare Metal Mater. Eng.* **2006**, *35*, 501.

Wang, J. *Analytical Electrochemistry*, 2nd Ed. ed.; John Wiley & Sons, Inc.: New York, 2000.

Wang, X. B.; Liu, Y. Q.; Zhu, D. B. *J. Nanosci. Nanotechnol.* **2002**, *2*, 33.

Weber, A.; Ivers-Tiffee, E. *J. Power Sources* **2004**, *127*, 273.

Wright, D. A.; Thorp, J. S.; Aypar, A.; Buckley, H. P. *J. Mater. Sci.* **1973**, *8*, 876.

Wu, Q.-H.; Abernathy, H.; Liu, M. "FTIR Studies and Kinetic Modeling of Oxygen Reduction on Cathode Materials for SOFCs"; 204th Meeting of the Electrochemical Society, 2003.

Xu, C.; Xu, G.; Wang, G. *J. Mater. Sci.* **2002**, *38*, 779.

Yamaji, K.; Kishimoto, H.; Xiong, Y. P.; Horita, T.; Sakai, N.; Brito, M. E.; Yokokawa, H. *J. Power Sources* **2006**, *159*, 885.

Yang, Y. L.; Yan, H. W.; Fu, Z. P.; Yang, B. F.; Xia, L. S.; Xu, Y. D.; Zuo, J.; Lu, F. Q. *J. Phys. Chem. B* **2006**, *110*, 846.

Ye, X. F.; Huang, B.; Wang, S. R.; Wang, Z. R.; Xiong, L.; Wen, T. L. *J. Power Sources* **2007**, *164*, 203.

Yoon, S. P.; Han, J.; Nam, S. W.; Lim, T. H.; Hong, S. A. *J. Power Sources* **2004**, *136*, 30.

Zhan, Z.; Barnett, S. A. *Solid State Ionics* **2005**, *176*, 871.

Zhan, Z. L.; Barnett, S. A. *Science* **2005**, *308*, 844.

Zhang, X.; Robertson, M.; Deces-Petit, C.; Qu, W.; Kesler, O.; Maric, R.; Ghosh, D. *J. Power Sources* **2007**, *164*, 668.

Zheng, R.; Zhou, X. M.; Wang, S. R.; Wen, T. L.; Ding, C. X. *J. Power Sources* **2005**, *140*, 217.

Zhu, H.; Kee, R. J.; Janardhanan, V. M.; Deutschman, O.; Adams, J.; Eldridge, D.; Goodwin, D. G. "The Influence of Elementary Heterogeneous Reforming Chemistry within Solid-Oxide Fuel Cell Anodes"; Western States Section of the Combustion Institute, 2003, Los Angeles, CA.

Zhu, H. Y.; Colclasure, A. M.; Kee, R. J.; Lin, Y. B.; Barnett, S. A. *J. Power Sources* **2006**, *161*, 413.

Zhu, H. Y.; Kee, R. J. *J. Electrochem. Soc.* **2006**, *153*, A1765.

Zhu, H. Y.; Kee, R. J.; Janardhanan, V. M.; Deutschmann, O.; Goodwin, D. G. *J. Electrochem. Soc.* **2005**, *152*, A2427.

Zhu, W.; Xia, C. R.; Fan, J.; Peng, R. R.; Meng, G. Y. *J. Power Sources* **2006**, *160*, 897.

Zhu, W. Z.; Deevi, S. C. *Mater. Sci. Eng.* **2003**, *A362*, 228.